MAPPING GAS-CHARGED FAULT BLOCKS AROUND THE VINTON SALT DOME, LOUISIANA USING GRAVITY GRADIOMETRY DATA

A THESIS

PRESENTED TO

THE FACULTY OF THE DEPARTMENT OF EARTH AND ATMOSPHERIC SCIENCES

UNIVERSITY OF HOUSTON

IN PARTIAL FULFILLMENT

OF THE REQUIREMENTS FOR THE DEGREE

MASTER OF SCIENCE IN GEOPHYSICS

BY

CHRIS ENNEN

AUGUST 2012

MAPPING GAS-CHARGED FAULT BLOCKS AROUND THE VINTON SALT DOME, LOUISIANA USING GRAVITY GRADIOMETRY DATA

CHRIS ENNEN

_____

APPROVED:

_____

DR. STUART HALL, CHAIRMAN

_____

DR. JANOK BHATTACHARYA, PROFESSOR

_____

DR. NIRANJAN BANIK, SCIENTIFIC ADVISOR, SCHLUMBERGER

_____

DEAN, COLLEGE OF NATURAL SCIENCES AND MATHEMATICS

ACKNOWLEDGEMENTS

I want to thank Dr. Stuart Hall for giving me a lot of his evenings and advice in putting together this study. Thanks to my thesis committee member, Dr. Janok Bhattacharya, for connecting me to Drillinfo.com and suggestions with the production aspect of the dome. Thanks also to my other thesis committee member, Dr. Niranjan Banik, for suggesting additional attributes and knowledge on Gulf Coast geology. I want to thank Chirag Patel for help with MATLAB coding. Thanks to Rick Zoss for providing the top salt interpretation for my model. I'm thankful to Mark Etheridge for providing well logs and guidance on the exploration side of the Vinton dome. I am very grateful to Bell Geospace Inc. for providing the Full Tensor Gradiometry data this study focuses on, and especially to Catherine Cox for providing an additional terrain correction. I want to thank Geosoft Inc. for providing the license to the Montaj software used in this study. Thanks to Dale Bird for expertise in using Geosoft Montaj. Thanks to drillinginfo.com for access to their database. I want to thank Schlumberger for keeping me employed during this experience. Thanks to my wife, Kesa, for watching the kids while I was sitting in a computer lab day and night. Last, I want to thank my parents, Bryan and Patty Ennen, for their words of encouragement and support while I wrote this work.

Dedication

I dedicate this to my kids, Ryker and Cole.

MAPPING GAS-CHARGED FAULT BLOCKS AROUND THE VINTON SALT DOME, LOUISIANA USING GRAVITY GRADIOMETRY DATA

AN ABSTRACT OF A THESIS

PRESENTED TO

THE FACULTY OF THE DEPARTMENT OF EARTH AND ATMOSPHERIC SCIENCES

UNIVERSITY OF HOUSTON

IN PARTIAL FULFILLMENT

OF THE REQUIREMENTS FOR THE DEGREE

MASTER OF SCIENCE IN GEOPHYSICS

BY

CHRIS ENNEN

AUGUST 2012

ABSTRACT

Reflection seismic imaging of complex faulting and associated petroleum reservoirs adjacent to onshore salt domes in the Gulf Coast region is both expensive and time consuming. Modeling studies show that gravity gradiometry data have the resolution in ideal conditions to image such reservoirs where seismic is unavailable or cost averse. Full Tensor Gravity Gradiometry (FTG) data, which are higher resolution than conventional gravity data, have been acquired by Bell Geospace over the Vinton salt dome located in southwest Louisiana.

A model of the dome incorporating reflection seismic, well logs, VSP, and conventional gravity interpretations was built and input to a FTG forward calculation program. The resulting signal was subtracted from the recorded survey to remove the overpowering signal of the dome. This residual image revealed anomalies linked to subsurface structures such as faults, gas-charged reservoirs, and parts of the salt dome not included in previous studies. Models of gas-charged reservoirs were produced and input to the forward calculation program to compare the results with anomalies found near the dome.

Negative Eötvös anomalies on the Tzz component of the residual image are observed within the maximum boundary of the salt dome. The distribution and amplitudes of these anomalies are used to discriminate between signals caused by salt and signals caused by reservoirs. Oil and gas production data overlaid on the FTG data show production within areas with signal character for gas-charged reservoirs.

Table of Contents

Chapter 1 Introduction 1
1.1. Vinton Salt Dome 2
1.2. Full Tensor Gradiometry (FTG) Method 3
1.3. Objective of Study 5
Chapter 2 Study Area 6
2.1. Regional Setting 7
2.2. Structure 10
2.3. Stratigraphy 12
Chapter 3 Data 16
3.1. Seismic 18
3.2. VSP 20
3.3. Well Logs 21
3.4. Conventional Gravity 22
3.5. Full Tensor Gradiometry (FTG) 23
Chapter 4 Methods 26
4.1 Introduction 26
4.1 Full Tensor Gradiometry Processing 27
4.2. Development of the Initial Model 29
4.3. Forward Model Signal Calculation and Subtraction 34
4.4. Attributes 35
Chapter 5 Results 40
5.1. Model Results 40
5.2. Reservoir Model Results 44
5.3. Subtraction Results 46
5.3. Attributes 56
5.4. Data Rotation 68
Chapter 6 Interpretation 74
6.1. Caprock 76
6.2. Salt Dome 79

6.3. Faults 83
6.4. Reservoirs 85
Chapter 7 Discussion 92
7.1. Near Surface 92
7.2. Caprock 93
7.3. Salt Dome 94
7.4. Faults 96
7.5. Reservoirs 100
Chapter 8 Conclusions 103
8.1. Future Work 104
Appendix 106
References 124

Figure 1.1. Reservoirs found near salt domes (Levin, 2006)..... 3
Figure 1.2. Full Tensor Gravity components (modified from O'Brien et al., 2005)..... 4
Figure 2.1 Regional cross section of Gulf Coast and Gulf of Mexico basin. Shoreline marked by inverted triangle, red dot indicates approximate position of Vinton dome, and dotted line shows lower limit of reflection seismic data (Peel et al., 1995) 9
Figure 2.2. Mapped faults on interpreted Siphonina davisi horizon spanning 1 to 1.7 s. Faulting exhibits a single offset and offset radial fault patterns (Coker, 2006). 11
Figure 2.3. Geologic map of southwest Louisiana showing faults scarps. The V denotes Vinton salt dome, C is for Cameron Meadows salt dome, H is for the Hackberry salt dome, and I denotes inland facing scarps (Heinrich, 2005). 12
Figure 2.4. Generalized stratigraphy of Vinton salt dome sedimentary formations (modified from Duncan, 2005). 15
Figure 3.1. Available datasets over the Vinton dome. Dome peak and maximum extent outlined in magenta (Eti, 2004). 17
Figure 3.2 Top salt interpretation from seismic data. Red circles outlines maximum extent of caprock. 20
Figure 3.3 Full tensor gradiometry measurements over the caprock area of the Vinton salt dome. 24
Figure 3.4 Noise analysis for measured FTG survey. 25
Figure 4.1 Gulf Coast Density-Depth Curve (modified from Nettleton, 1934) 31
Figure 4.2 Windows used in calculating coherence values. 38
Figure 5.1 Tzz field data, calculated dome signal, and difference as viewed in MATLAB. 42
Figure 5.2 Txx field data, calculated dome signal, and difference as viewed in MATLAB. 42
Figure 5.3 Qualitative guide for assessing whether residual signals may indicate a gas reservoir. 44
Figure 5.4 Forward calculation of Tzz for known production (SONRIS database access, 2012).... 46
Figure 5.5 Tzz a) salt body model signal calculated 100m above observation surface, b) field measurements 100m upward continued, c) residual difference between both. Arrows illustrate areas of interest highlighted in the text. 50
Figure 5.6 Txx a) salt body model signal calculated 100m above observation surface, b) field measurements 100m upward continued, c) residual difference between (a) and (b). 51
Figure 5.7 Txy a) salt body model signal calculated 100m above observation surface, b) field measurements 100m upward continued, c) residual difference between (a) and (b). 52
Figure 5.8 Txz a) salt body model signal calculated 100m above observation surface, b) field measurements 100m upward continued, c) residual difference between (a) and (b). 53
Figure 5.9 Tyy a) salt body model signal calculated 100m above observation surface, b) field measurements 100m upward continued, c) residual difference between (a) and (b). 54
Figure 5.10 Tyz a) salt body model signal calculated 100m above observation surface, b) field measurements 100m upward continued, c) difference between (a) and (b). 55

Figure 5.11 H-1 Invariant after subtraction. Outer white outline is salt model maximum extent. Inner white outline is maximum extent of caprock. 58
Figure 5.12 H-2 Invariant after subtraction. Outer white outline is salt model maximum extent. Inner white outline is maximum extent of caprock. 59
Figure 5.13 R-1 Invariant after subtraction. Outer white outline is salt model maximum extent. Inner white outline is maximum extent of caprock. 60
Figure 5.14 R-2 Invariant after subtraction. Outer white outline is salt model maximum extent. Inner white outline is maximum extent of caprock. 61
Figure 5.15 Tzz coherence after subtraction. Outer white outline is salt model maximum extent. Inner white outline is maximum extent of caprock. 62
Figure 5.16 Txx coherence after subtraction. Outer white outline is salt model maximum extent. Inner white outline is maximum extent of caprock. 63
Figure 5.17 Txy coherence after subtraction. Outer white outline is salt model maximum extent. Inner white outline is maximum extent of caprock. 64
Figure 5.18 Txz coherence after subtraction. Outer white outline is salt model maximum extent. Inner white outline is maximum extent of caprock. 65
Figure 5.19 Tyy coherence after subtraction. Outer white outline is salt model maximum extent. Inner white outline is maximum extent of caprock. 66
Figure 5.20 Tyz coherence after subtraction. Outer white outline is salt model maximum extent. Inner white outline is maximum extent of caprock. 67
Figure 5.21 Residual Txz data rotated counterclockwise by 45 degrees. Outer white outline is salt model maximum extent. Inner white outline is maximum extent of caprock. 70
Figure 5.22 Residual Txz data rotated counterclockwise by 135 degrees. Outer white outline is salt model maximum extent. Inner white outline is maximum extent of caprock..... 71
Figure 5.23 Residual Txx data rotated counterclockwise by 45 degrees. Outer white outline is salt model maximum extent. Inner white outline is maximum extent of caprock. 72
Figure 5.24 Residual Txx data rotated counterclockwise by 135 degrees. Outer white outline is salt model maximum extent. Inner white outline is maximum extent of caprock..... 73
Figure 6.1 Observed gradients (left) and residual gradients (right) with maximum extent of caprock model outlined in white. 78
Figure 6.2 Caprock signal for the Tzz gradient with well log picks for top caprock (green) and top of salt (black) (Eti, 2004). 79
Figure 6.3 Possible salt migration up counter-regional fault as region moves basinward. 80
Figure 6.4 (Left) Residual map upward continued to two km. Eti's (2004) top salt surface contours overlaid in black. (Right) Tzz residual map with 3.8 km contour from Eti's (2004) top salt interpretation outlined in white. Arrows on the right residual anomaly map define a positive trend extending south from the caprock. 82
Figure 6.5 Fault types found near salt in a stepped counter-regional salt system (Rowan et al., 1999). 83

Figure 6.6 a) H-2 Invariant with radial fractures interpreted and (b) an example interpretation from Matargio and Kieley (2009). 85
Figure 6.7 Reservoir tests for the Tzz gradient. Two block sizes were used with a constant thickness of 100m at three different depths. 87
Figure 6.8 Residual maps for Txz, Txx, and Tzz. Anomalies outlined in white exhibit expected reservoir signal. 88
Figure 6.9 Residual maps for Tyx, Tyz, and Tyy. Anomalies outlined in white exhibit expected reservoir signal. 89
Figure 6.10 Comparison of production wells and dry holes drilled. Black circles are shallower than 1300m and white circles are deeper than 1300m depth. Prospective areas outlined in white. 90
6.11 Residual Tzz plots with production wells from drillinginfo.com with colors corresponding to the amount of gas production at the well. 91
Figure 7.1. Top and base salt interpretation of seismic showing the time interval of used for interpreting the salt (Eti, 2004) 95
Figure 7.2. Velocity model illustrating offset of velocities cause by counter-regional fault (Duncan, 2005). 98
Figure 7.3. H-2 Invariant without and with fault interpretation overlain (Coker, 2006). 99
Figure 7.4. Distribution of producing perforation intervals from east to west across survey area (SONRIS, 2012). 101
Figure 7.5. a) Residual Tzz surface upward continued to 1000 m with production wells deeper than 1300 m plotted. b) Residual Tzz surface upward continued to 500 m with production wells shallower than 1300 m plotted. Maximum extent of salt outlined in black 102

Chapter 1

Introduction

The Gulf Coast region of the United States has been an active producer of oil and gas for over a century. Most reservoirs in the Gulf Coast are found on salt dome flanks, in downthrown fault closures, anticlines, and in stratigraphic pinchouts (Harrison et al., 1970; Branson, 1991). The first hydrocarbon exploration method in the region involved drilling a well at any location that exhibited evidence of a salt dome, such as a depression in the landscape or any kind of hydrocarbon seepage at the surface (Owen, 1975). Acquisition of seismic reflection surveys in the 1950's made exploration by subsurface imaging possible (Fails, 1995). Seismic data, however, have limitations near salt domes where imaging becomes difficult due to the steeply dipping salt flanks that scatter or absorb seismic energy (Coburn, 2002).

Salt domes in the Gulf Coast continue to produce hydrocarbons. The United States Geological Survey (USGS) estimates that more than 9 billion cubic feet of gas have not been recovered from the region (Swanson and Karlsen, 2009). New developments around salt domes require more sophisticated geophysical techniques, such as Vertical Seismic Profiling (VSP) (Constance et al., 1999; Kisin, 2003), well log data (Coker, 2006), conventional gravity (Eti, 2004), and gravity gradiometry (Prutzman, 1998; O'Brien et al., 2005). More salt dome development also requires a more holistic approach to the hydrocarbon system. A better understanding of the relationship and timing of source, migration pathway, and trap is critical in predicting where hydrocarbons are stored. New geophysical techniques and a holistic understanding of a hydrocarbon system are the best approaches in developing mature hydrocarbons fields where previously bypassed reservoirs are still available for production.

Full Tensor Gradiometry (FTG) data has seen renewed interest in recent years in mining applications and for gleaning new insights in salt geometry in marine settings (Bell et al., 1997; Mataragio and Kieley, 2009; Hokdstad et al., 2011). The survey collected over the Vinton salt dome is unique as an attempt to measure the gravity field for use at the reservoir level.

1.1. Vinton Salt Dome

The Vinton salt dome, located in Calcasieu Parish, Louisiana, has many characteristics that are typical of Gulf Coast salt domes, and can be used as an analog for understanding bypassed resources in mature fields. It is a piercement dome that has been in production since 1901 (Thompson and Eichelberger, 1928). Like many salt domes in the Gulf Coast region, most discoveries at Vinton were made on the north side of the dome where sedimentation occurred as channels flowed around highs caused by domes (Cossey and Jacobs, 1992). Many discoveries have been made on the downthrown side of faults where thicker sediments have accumulated. Since Vinton has a counter-regional fault the downthrown block is on the north side (Harrison et al., 1970; Branson, 1991). It has produced hydrocarbons from many of the reservoir types associated with salt dome hydrocarbon production (Figure 1.1), including its caprock, the steeply dipping salt flanks, fault blocks, and from beneath salt overhangs (Owen, 1975). Eleven domes in the Gulf Coast Region, including Vinton, have salt overhangs (Judson and Stamey, 1933). Many of the hydrocarbon bearing trends of the Gulf Coast are represented and have produced within the Vinton field, including the Pliocene, Miocene, and Oligocene (Sawtelle, 1936). Formations adjacent to the dome have been fractured through faulting and are increasingly the focus of companies trying to find resources to produce in the region. This faulting has produced blocks available for hydrocarbon trapping and storage. The Vinton dome has been studied by an array of geophysical techniques; including VSP (Constance et al., 1999;

Eti, 2004), well log data (Coker, 2006), conventional gravity (Eti, 2004), and reflection seismic (Duncan, 2005; Coker, 2006). Recently Bell Geospace has acquired a gravity gradiometry survey over the dome. If gravity gradiometry over the Vinton dome can be used to image reservoirs then the method can be put to use in many other salt domes in the region to extend field life and replenish reserves for independent and major oil companies (Cossey and Jacobs, 1992; Hoeve and Borowski, 1988).

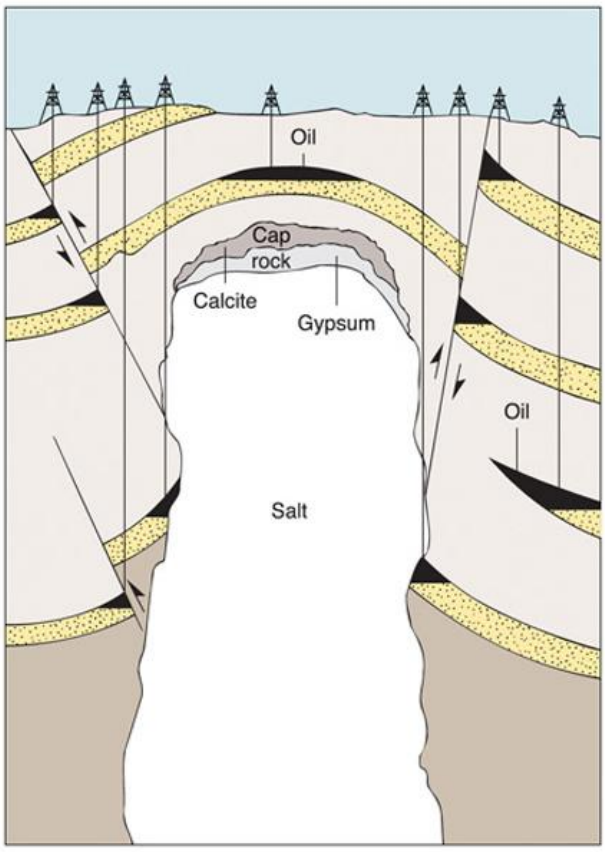

Figure 1.1. Reservoirs found near salt domes (Levin, 2006)

1.2. Full Tensor Gradiometry (FTG) Method

Gravity gradiometry data are obtained by measuring the rate of change of the earth's gravity field along a surface. Conventional gravity measurements, on the other hand, only

sample the vertical component of Earth's gravity field. Gravity gradiometry samples all nine components of the gradient for the gravity field (Bell et al., 1997). Each component measures the signal from subsurface structures in a different direction (Figure 1.2). Assuming the x axis is east-west, the y axis is north-south, and the z axis is the vertical then Txx emphasizes north-south trending features. Txy emphasizes northeast-southwest trending features. Txz and Tyz highlight the central axis of a mass. Tyy emphasizes east-west features. Tzz emphasizes all edges. Structural resolution near complex salt bodies is the main advantage of measuring the gravity gradient (Bell et al., 1997). In the Green Canyon area of the Gulf of Mexico, a salt body with flanks dipping 60^{o} obscured the seismic imaging of subsalt structure in the K-2 field (O'Brien et al., 2005). Inversion of data from a gradiometry survey compared with a wave-equation depth migration imaged a keel underneath the salt body at a depth of 7.6 km. The keel measured 2.4 km horizontally and 1.2 km vertically. Elsewhere, a subsalt anticline at 3 km depth was imaged using gradiometry data over the Mississippi Canyon area of the Gulf of Mexico (Prutzman, 1998). Gravity gradiometry has been shown to be a valuable tool for deepwater reservoirs, but it has not been fully utilized in shallow, onshore areas.

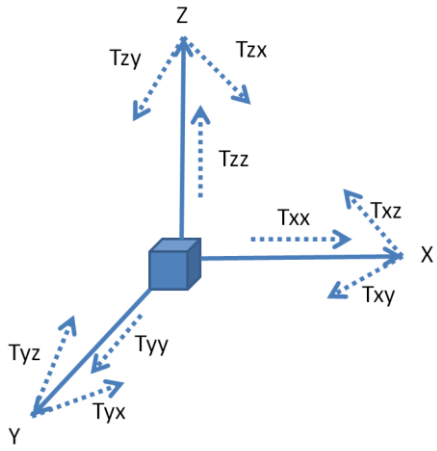

Figure 1.2. Full Tensor Gravity components (modified from O'Brien et al., 2005).

1.3. Objective of Study

The purpose of this project is to use nontraditional geophysical techniques, such as gravity gradiometry, to differentiate between water-saturated and gas-saturated salt blocks in areas that are difficult to image with seismic, such as those associated with steeply dipping salt flanks or steeply dipping faults. The complex wavefield behavior of seismic reflection and transmission through these structures requires sophisticated and expensive imaging methods that are not cost effective for the reserves available. The goal of this study is to detect and map possible gas-charged fault blocks near the flanks of the Vinton salt dome using gravity gradiometry data. The enhanced resolution of gravity gradiometry should provide less ambiguity in locating compartmentalized reservoirs adjacent to the dome. Mapping these compartments may provide a better understanding of the Vinton salt dome system as a whole, and an evolutionary framework of the dome can be formed that can be applied to other salt domes in the Gulf Coast Region. This is the first attempt at using FTG data to search for gas hydrocarbons over the Vinton dome, and there are no available publications for such a study elsewhere.

Chapter 2

Study Area

The Vinton Salt Dome lies within the Gulf of Mexico Continental Margin (Watkins et al., 1978). It is located 5 kilometers southwest of Vinton in Calcasieu Parish, Louisiana. The surface expression of the dome is a slight depression within a raised mound filled by Gray Lake (Barton, 1936). It is a piercement dome with a large caprock that overhangs the salt column. There is a lot of discussion centered around how the dome formed and whether or not it is attached to autochthonous Louann salt. There are two theories of dome formation. One is that it is an attached offshoot of the Louann salt (Coker, 2006). The second is that it was emplaced in the Eocene and is not attached to the Louann salt (Eti, 2004). It pierces the Miocene Fleming, Oligocene Vicksburg, and Eocene Jackson formations (Sawtelle, 1936). The dome sits on top of a column of Cenozoic and Mesozoic sediments in an almost unbroken depositional column (Martin and Bouma, 1978). A counter-regional fault bisects the dome and has three fault sets adjacent to it. Oil seepages, sour water and the topographic depression were used as early evidence for salt dome occurrence with hydrocarbons (Thompson and Echelberger, 1928, Paine et al., 1968). Most production comes from the Miocene Fleming and Oligocene Vicksburg formations (Branson, 1991).

The first well to recover oil was drilled at Vinton in 1901 (Thompson and Echelberger, 1928). Oil was found beneath a salt overhang in 1911 (Owen, 1975). The largest gas well initially produced 10 million cubic feet of gas from a depth of 1,060 meters (Thompson and Eichelberger, 1928). Gas-condensate production wasn't established until 1952 (Paine et al., 1968). Most of the oil and gas production has occurred on the east, northeast, and north sides

of the dome. The source rock is thought to be either the Eocene Jackson Formation (Swanson and Karlsen, 2009) or a deeper undiscovered source (Branson, 1991). The dome is similar to other Gulf Coast salt domes in that it has produced oil and gas from the Eocene, Miocene, and Oligocene trends.

After a century of production more focus is now on finding less obvious traps and bypassed reservoirs (Branson, 1991). A recent study proposed an estimated 9384 billion cubic feet of natural gas and 542 million barrels of natural gas liquids left in the Frio and Anahuac formations throughout the Gulf Coast. This includes unconventional reservoirs that may include the Eocene Jackson Shale or formations deeper than 3 km where little exploration has been attempted (Swanson and Karlsen, 2009).

2.1. Regional Setting

.Gulf Coast Region. The Gulf Coast Region is an area bounded on the east by the Louisiana-Alabama border and on the west by the western boundary of Jackson County, Texas. It extends inland from the Gulf of Mexico to between 130 and 160 kilometers (Barton, 1936). The basement of the Gulf Coast Region is Paleozoic and Precambrian metamorphic and granite rock between 16 to 20 kilometers deep (Figure 2.1) (Martin and Bouma, 1978; Peel et al., 1995).

The majority of faults in the central Gulf Coast region are extensional growth faults interpreted as Late Cretaceous to early Eocene in age and activated by detachment along the autochthonous Louann salt (Peel et al., 1995). Growth faults can be attributed to three processes. The first process is the response to sediment overload along the Tertiary and Quaternary shelf edges. Second is differential compaction associated with changes in sediment thickness and lithology. The third is salt withdrawal during episodes of diapir growth (Martin and

Bouma, 1978). There are three fault trends in the central Gulf Coast. From north to south they are; the Glenmora, the Tepetate, and a southern region between the Tepetate and the shoreline. Vinton dome is located within the southern region between the Tepetate trend and the shoreline (Heinrich, 2005). Faults within this trend do not exhibit a uniform direction.

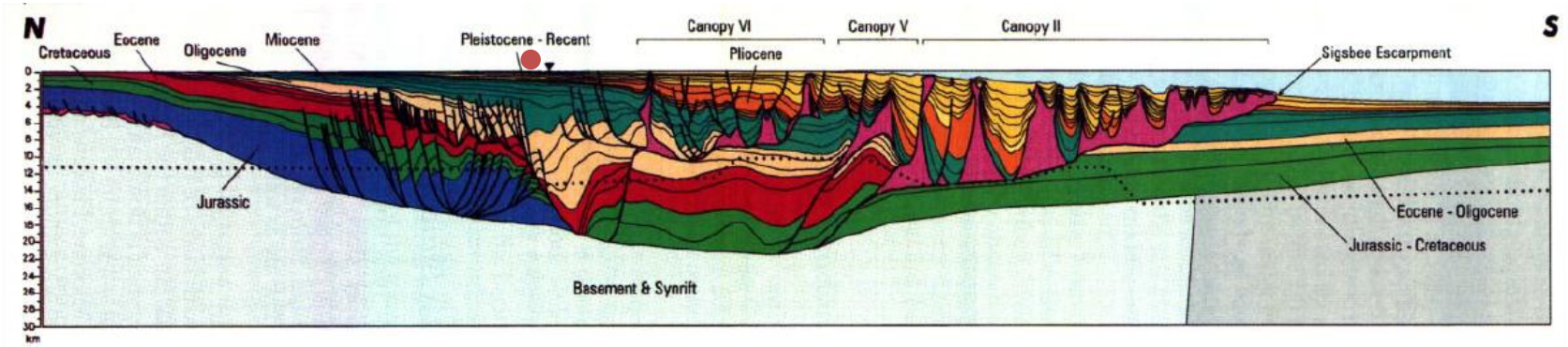

Figure 2.1 Regional cross section of Gulf Coast and Gulf of Mexico basin. Shoreline marked by inverted triangle, red dot indicates approximate position of Vinton dome, and dotted line shows lower limit of reflection seismic data (Peel et al., 1995)

Gulf of Mexico Basin. The Gulf of Mexico basin formed in the Middle Jurassic by rifting (Salvador, 1987; Peel et al., 1995). Mesozoic and Cenozoic rocks sit unconformably on top of complexly folded and faulted Paleozoic rocks of the Ouachita and Appalachian tectonic belts. In the early Cenozoic, the Laramide Orogeny provided a large amount of sediment to the Gulf of Mexico Basin. The sediment accumulation outpaced the rate of subsidence and as a result, thick accumulations of sediment were deposited along the Gulf Coast (Martin and Bouma, 1978).

2.2. Structure

Caprock. The shallow portion of the caprock comes within 130 meters of the surface (Owen, 1975; Eti, 2004). The dome has a caprock of limestone, gypsum, and anhydrite that ranges in thickness from 210 m to 60 m. This caprock formed by either precipitation in place, or solution of impure salt rock at the top of the dome (Ingram, 1991). A section of the caprock 210 m thick protrudes north from the top of the dome.

Dome. The dome is 3.8 km in height (Eti, 2004). The core of the dome is 1,280 meters from north to south and 1,520 meters from east to west. The dome has a residual gravity signature of -26.5 mGal at its center and a -19 mGal residual at its southwest edge (Wilson and Noel, 1983). The dome is considered a piercement dome because the Eocene Jackson Formation is pierced by the dome (Jackson and Talbot, 1986). There is debate as to whether the dome is attached to autochthonous salt (Eti, 2004; Coker, 2006). Eti's (2004) models of the gravity signature of the dome suggest the salt does not reach depths greater than 8 km, where autochthonous salt would be. Coker (2006) argues through lack of subsalt reflections in the seismic that the dome is attached to the Louann salt.

Faults. A single counter-regional fault downthrown to the northwest with three sets of peripheral faults characterizes complex faulting around the dome. It's inferred that faulting occurred as a result of emplacement of the salt dome in the Eocene. Coker (2006) described this fault system as a single offset with offset radial pattern faulting using Fails (1990) classification system. Figure 2.2 shows a counter-regional fault oriented WSE-ENE and downthrown 427 meters to the northwest. The counter-regional fault is unusual in an extensional tectonic region since most faults dip in the direction of extension.

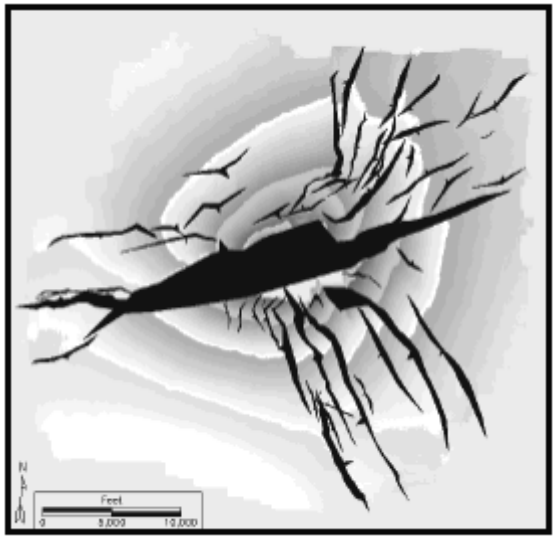

Figure 2.2. Mapped faults on interpreted Siphonina davisi horizon spanning 1 to 1.7 s. Faulting exhibits a single offset and offset radial fault patterns (Coker, 2006).

Reactivation of faults resulted from loading of the Gulf of Mexico margin starting in the Late Pliocene, which renewed flow of salt. Vinton has an extensive fault-line scarp system radiating from it. Figure 2.3 shows fault-line scarps that extend as far as 20 km to the north-east, 12 km to the southeast, and 5 km to the west, height of fault-line scarps to northeast and west are typically .9 m at the surface. Displacement on the longest of the northern fault-line scarps reverses. It changes from an eastward facing scarp to a westward facing scarp. Fault-line scarps to the southeast range in height from .6 to .9 m. Faults have a tectonic origin based on

displacement of terrace surfaces, relict river channels, and coastal ridges. The fault-line scarps are unique to Vinton and don't form part of regional trends found running east-west across Louisiana, such as the Tepetate fault-line scarp trend or the Glenmora trend. The fault-line scarps around Vinton reflect salt flowage at depth associated with domes (Heinrich, 2005).

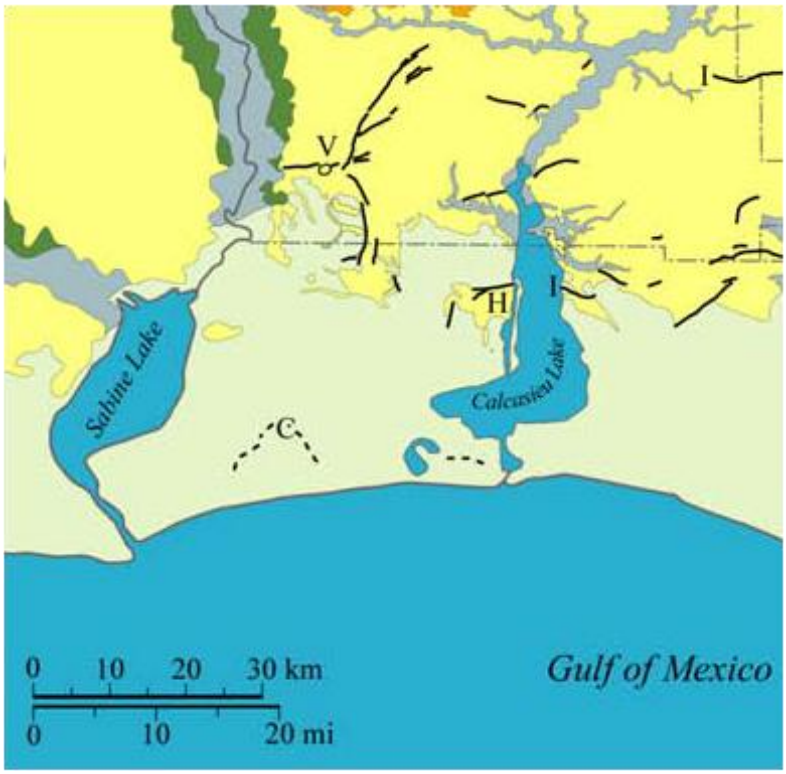

Figure 2.3. Geologic map of southwest Louisiana showing faults scarps. The V denotes Vinton salt dome, C is for Cameron Meadows salt dome, H is for the Hackberry salt dome, and I denotes inland facing scarps (Heinrich, 2005).

2.3. Stratigraphy

A regional cross section of the central Gulf Coast is found in Figure 2.1. The deepest formation drilled in Vinton is the Vicksburg Formation at 2000 meters (Sawtelle, 1936). Below the Vinton salt dome is an undetermined amount of Cretaceous and Cenozoic sediments. A generalized stratigraphic column is shown in Figure 2.4.

Eocene Jackson Formation. The Jackson Formation is an Eocene shale formation of undetermined thickness (Thompson and Echelberger, 1928). It's thought to be a source rock by the USGS, but volumes were small for wells drilled near the Vinton dome (Deussen, 1934; Swanson and Karlsen, 2009). The Jackson Formation was deposited at the same time the Vinton salt was emplaced (Eti, 2004). It exhibits steep dips and is overturned resulting from deformation caused by migration of the salt after emplacement (Xu et al., 2012).

Oligocene Hackberry, Vicksburg, Frio and Anahuac. The Oligocene Formation is mostly sand and sandy shale. It's the most popular target for oil in the Gulf Region. During the Oligocene the Hackberry Formation was deposited by submarine turbidity currents meandering around paleotopographic highs in a marginal and shallow marine region 32 km wide where several salt domes existed (Paine, 1971; Duncan, 2005). Fields consist of structural and stratigraphic traps on the updip flanks of salt domes where submarine channels were forced to meander around paleobathymetric highs. Good targets are found on the outer edges of meanders north of salt domes where flow stripping occurs (Cossey and Jacobs, 1992).

The Vicksburg Formation overlays the Jackson Formation and is used to mark the end of the Eocene and the start of the Oligocene. It is 60 to 90 meters thick and is mostly sandstone and sandy shale. It is interpreted as a slope facies in a regional subsurface embayment (Cossey and Jacobs, 1992). In a number of places, the Vicksburg Formation is the only formation between the Jackson Formation and the Frio Formation (Duncan, 2005). However the Vicksburg Formation is seens as a control during deposition of the lower Hackberry Formation. Vicksburg Formation prospects usually consist of traps on the updip flanks of salt dome.

The Frio Formation overlays the Vicksburg (Swanson and Karlsen, 2009; Duncan, 2005). It is divided into lower, middle and upper members. The lower Frio is 120m thick. The middle Frio is 90 meters thick (Eti, 2004). The upper Frio is 240m thick. Across the Gulf Coast, porosity for the Frio ranges from 23-29% (Branson, 1991). Duncan (2005) describes it as a dark shale with massive sandstone beds. The interfingering sandstones are interpreted as a result of lowering of sea level along the northwest Gulf of Mexico basin.

The Anahuac Formation overlays the Frio Formation (Duncan, 2005). It is mostly shale with some sandstone and carbonates (Swanson and Karlsen, 2009). Porosities for the Anahuac are 26-28% (Branson, 1991). The shales are interpreted as transgressive, and include delta, shoreface, and slope sandstones. Coker (2006) interprets the Anahuac as a marker for the maximum landward shift of shorelines in the late Oligocene.

Miocene Fleming. The Fleming Formation contains massive sandstones with periodic shale breaks. Sandstone packages range in thickness from 2100 to 2300 meters. It was deposited in deltaic and continental environments (Duncan, 2005). Highstand deltaic sandstones sit conformably on top of late Oligocene Anahuac shales (Coker, 2006). It is one of the most prolific formations in the Gulf Coast (Branson, 1991; Borowski, 1990).

Pliocene gravel. Surface clay is underlain by Late Pliocene Lafayette gravel (Thompson and Eichelberger, 1928). The gravel contains sand and shale and averages 180 meters in thickness. Bulk density measurements range between 2 g/cc and 2.2 g/cc but there are measurements as low as 1.8 g/cc and as high as 2.4 g/cc (Eti, 2004).

Beaumont clay/ near surface.The Beaumont clay forms the surface above the dome and extends to 120 meters. The soil varies in density between 1.19 gm/cc and 1.70 gm/cc in the first two meters of the surface (NRCS, 2012).

Miocene	Grand Gulf	Upper			
		Middle			
		Lower			
Oligocene		Anahuac		Discorbis Zone	
				Heterostegina Zone	
					Het Lime
				Marginulina Zone	First Marginulina Sand
					Second Marginulina Sand
					Third Marginulina Sand
		Frio		Upper	Welch Sand
					Ortega Sand
					Klumpp A, B, C, D Sands
			Hackberry	Middle	Burleigh Sand
					Boaghi Sand
					Homeseeker A Sand
				Lower	First Nodosaria sand
					Second Nodasaria Sand
					Third Nodosaria Sand
					Fourth Nodosaria Sand
					Tweedel Sand
		Vicksburg			
Eocene		Jackson			

Figure 2.4. Generalized stratigraphy of Vinton salt dome sedimentary formations (modified from Duncan, 2005).

Chapter 3

Data

To build the most accurate model of the salt dome and caprock, integration of all useful *a priori* geophysical and geological data is needed. The datasets include a 3D seismic survey, a pair of vertical seismic profiles (VSP's), well logs, a gravity survey, and a FTG survey (Figure 3.1). A radial 3D seismic survey acquired around the dome is used for the macrostructure of the dome above 2800m depth and for imaging faults adjacent to the salt. VSP provides P-wave sediment velocities adjacent to the dome that can be converted into densities and the depths for strata. Well logs are used to locate proven hydrocarbon reservoirs, provide information on formation density, and to differentiate between salt and caprock. An interpretation of a conventional gravity survey is used for mapping the depth and extent of salt dome below 2800m depth. The gradiometry data are used as an imaging tool for areas not imaged by seismic data. Each geophysical technique has application for different aspects of model building, and each has pitfalls that can skew the model. It is important to understand the acquisition parameters and resolution of these datasets in order to know where and how effectively these data constrain the model.

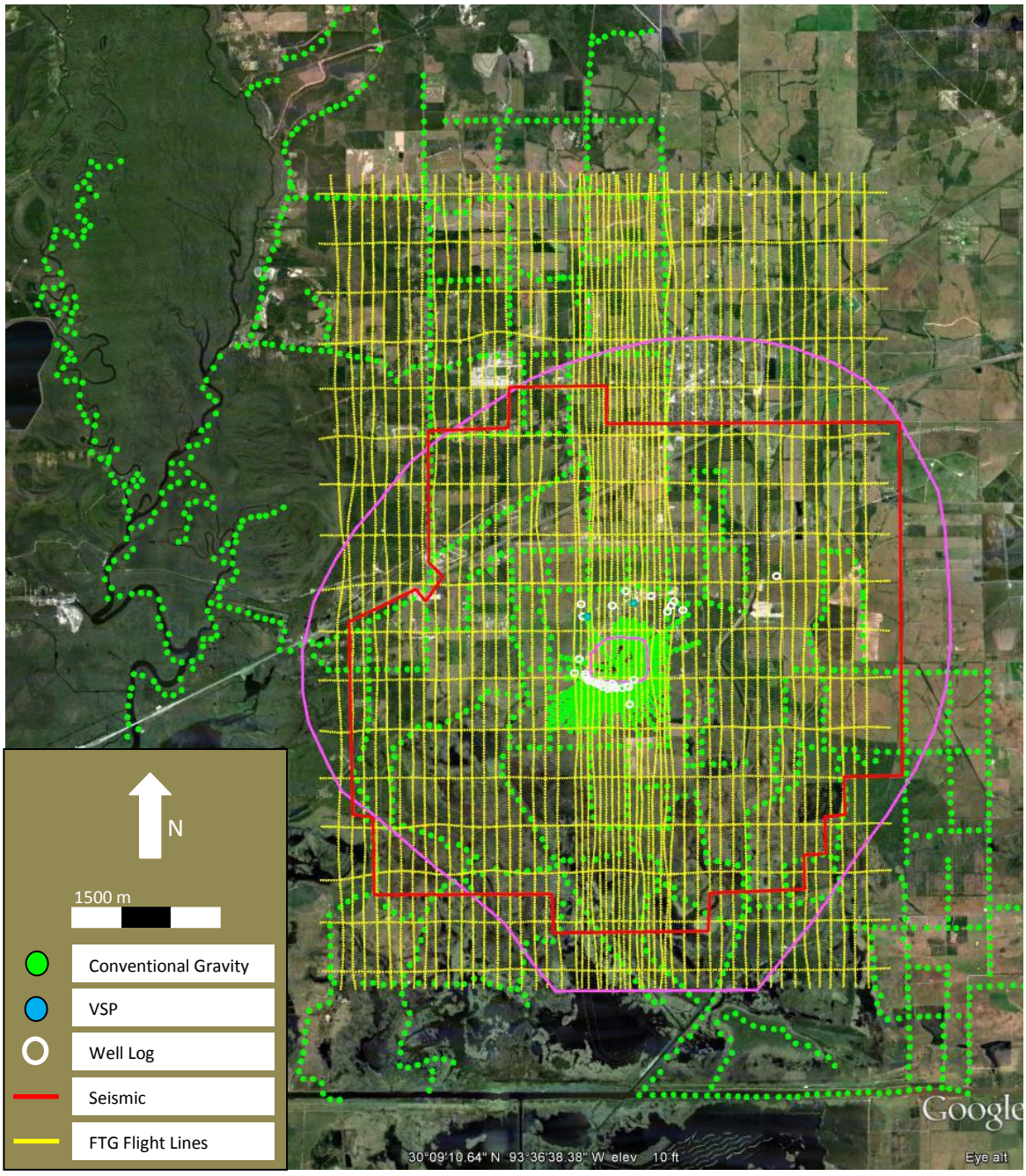

Figure 3.1. Available datasets over the Vinton dome. Dome peak and maximum extent outlined in magenta (Eti, 2004).

3.1. Seismic

A radial 3D seismic reflection survey centered over the caprock was acquired in 1998. Radial receiver lines in 5° increments were laid out around the dome. For each shot a 90° swath (19 lines) of receivers recorded the reflected seismic energy (Gherasim, 2005). Concentric rings of source locations were used. Receivers and source locations were spaced 50 m apart for a common midpoint of 25 m. The source used was 2.5 kg pentolite charges buried 18 m deep. The goal of the survey was to achieve spatial resolution of 60 m to image small polygonal faults (Constance et al., 1999; Coker, 2006). There is little coverage over the caprock of the dome because the structure is too shallow and rugose to image effectively with seismic data.

Before migration, the seismic data were pre-processed with geometry application, elevation static correction, a T^2 spherical divergence correction, trace by trace spiking deconvolution, and a time variant filter. Elevation statics use receiver elevations and shot hole depths to correct the data to a surface of zero feet. Elevations ranged from 1.5m to 3.3m. No reflection or refraction statics were applied to the data. The deconvolution was applied using a filter length of 124 ms and an operator length of 20 ms. The operator was applied in two windows as defined in Table 3.1. A time variant Butterworth band pass filter was applied after deconvolution. The filter bands are presented in Table 3.2 (Kimbro, 2003).

	Near Offset	Far Offset
Window 1 Start	500 ms	3000 ms
Window 1 End	3500 ms	4200 ms
Window 2 Start	3000 ms	3700 ms
Window 2 End	6000 ms	6000 ms

Table 3.1 Deconvolution application window definition.

Time (ms)	Low Cut (Hz)	Low Cut Slope (Db/octave)	Hi Cut (Hz)	Hi Cut Slope (Db/octave)
1000-1100	6	3	60	4
2500-2600	6	3	48	4
4000-4100	6	3	40	4
5900-6000	6	3	32	4

Table 3.2 Time variant filter parameters

The data were depth migrated using a well-derived velocity model (Kimbro, 2003). Twenty-six sonic logs were used to populate seven layers of interval velocities. The layers were defined by surfaces for the upper Miocene, upper mid-Miocene, mid-Miocene, Top Anahuac, A-sand, D-sand, and the Hackberry. The surfaces were interpreted on time-migrated data and converted to depth with well derived interval velocities. A linear gradient was used between well locations. A lot of *a priori* information has been derived from the seismic data. The salt

model was developed from interpretation of the seismic data integrated with salt picks from well log analysis (Figure 3.2). Faults were interpreted from the seismic reflection data. The disadvantage of using the seismic data for developing the salt model is the lack of imaging over the surface of the caprock, under salt overhangs, and on the flanks of the dome. The seismic data were very useful in connecting sparse well information into a single salt interpretation.

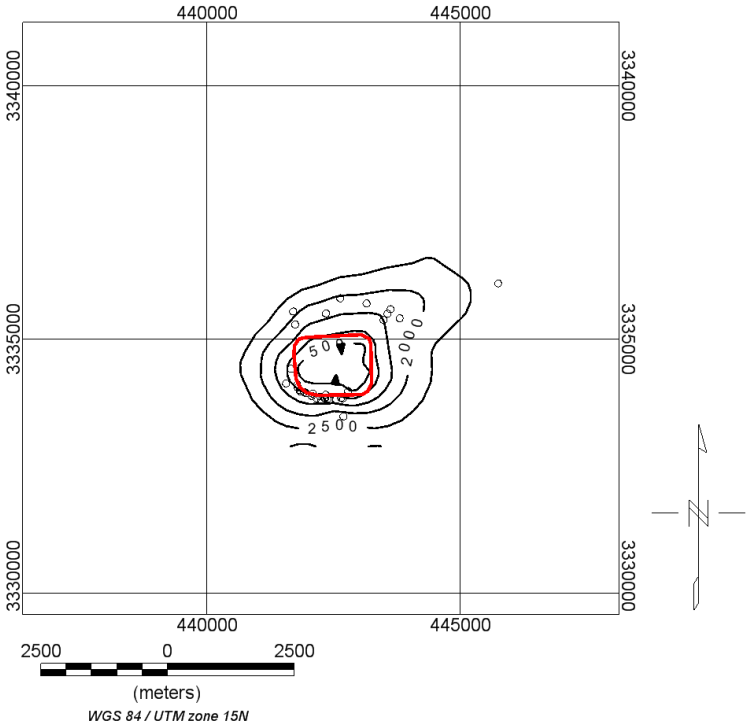

Figure 3.2 Top salt interpretation from seismic data. Red circles outlines maximum extent of caprock.

3.2. VSP

Two 3-C Vertical Seismic Profiles were simultaneously recorded with the radial 3D seismic reflection survey. The western well contained 3-C geophones cemented into place at 15 m intervals from 287 to 1217 m (930 m) depth. The receivers were split between 10 and 30 Hz geophones. Forty one shallow receivers were 10 Hz while 39 deeper receivers were 30 Hz. The

eastern well contained 3-C geophones in a coiled tubing deployment configuration 15 m apart from 107 to 716 m (609 m) depth (Constance et al., 1999).

During processing all three component traces were separated and processed. A filter was derived and applied to match the 10 Hz geophones to the 30 Hz geophones. Surface consistent, time-invariant scalars were used to balance the amplitudes of the traces. The horizontal geophones were rotated to a consistent orientation. Deconvolution was applied to shape the wavelet and balance the frequency spectrum. The up-going and down-going wavefields were separated.

VSP data were used to determine seismic velocities near the salt dome (Gherasim, 2005). These velocities were converted into densities using Gardner's equation (Gardner et al., 1974):

$$\rho = .23V^{.25} \tag{3.1}$$

3.3. Well Logs

Well logs provide constraints on the extent of salt and have the resolution necessary for establishing the depth of the interface between salt and caprock. There are an estimated 550 well logs measured around the dome (Coker, 2006). One hundred and four well logs were provided by White Oak Energy for analysis. These well logs covered 37 well locations. A map of well locations with well logs can be seen in Figure 3.1. Spontaneous potential, resistivity, and gamma ray measurements have been measured in different wells and some measurements have been taken multiple times in the same well. Using these measurements and mud log information, salt and caprock picks have been made in wells that have pierced the salt.

3.4. Conventional Gravity

Multiple conventional gravity studies have been carried over the Vinton dome in the last thirty years and published as maps of regional and residual Bouger anomaly maps with station locations included (Eti, 2004). Several gravity profiles were recorded over the caprock of the dome at a station spacing of 7.62 m. Farther away from the dome stations were spaced 61 m apart. These studies were digitized and collated into a single dataset of station locations with mGal measurements. Krigging was used to grid the data into a 45 square kilometer area with node spacing of 200 m (225x225 nodes) (Eti, 2004).

A graphical technique was used to separate the regional field from the local anomaly. A sediment density profile was derived using 34 density logs. This curve was used to derive a density contrast curve using a constant salt density of 2.17 g/cc (Eti, 2004).

The conventional gravity combined with sparse well log picks were used to create a map of the caprock by Eti (2004). This map was used to develop the caprock model. The density used for the caprock in the model was 2.7 g/cc. The model was input to a conventional gravity forward calculation. The results was then subtracted from the local anomaly plot to obtain the sub-crossover depth salt signal. The GF3XP inverse gravity-modeling software program was used to invert the sub-crossover depth salt signal for the geometry of the salt dome below the crossover depth with the assumption of a flat top at the crossover depth and a flat base.

The caprock map produced by Eti was the basis for caprock geometry used for forward modeling in this study. The salt geometry below the crossover depth was also used to develop a salt dome geometry below the crossover depth.

3.5. Full Tensor Gradiometry (FTG)

Bell Geospace Inc. acquired a FTG survey in 2008. The survey was planned for the caprock to be in the center of the survey. It is composed of 53 north-south lines 250 m apart. The center eighteen lines over the caprock are infilled at 125 m apart. Samples are taken every second. At airspeed of 240 km/hr the samples are spaced approximately 60 m apart. Each line is 16.7 km long. Seventeen east-west tie lines 11.3 km long were acquired 1 km apart. The plane's altitude varied between 52 m to 116 m above mean sea level. The data were conditioned with a proprietary noise reduction technique and terrain corrected with a density of 1.80 g/cc (Figure 3.3).

A simple way to analyze the noise content of FTG data is to sum the Txx, Tyy, and Tzz components of the measured data (Bell et al., 1997). The sum should be zero. This analysis was done on the received FTG survey (Figure 3.4). The noise content using this method is within +/- 1 Eötvös.

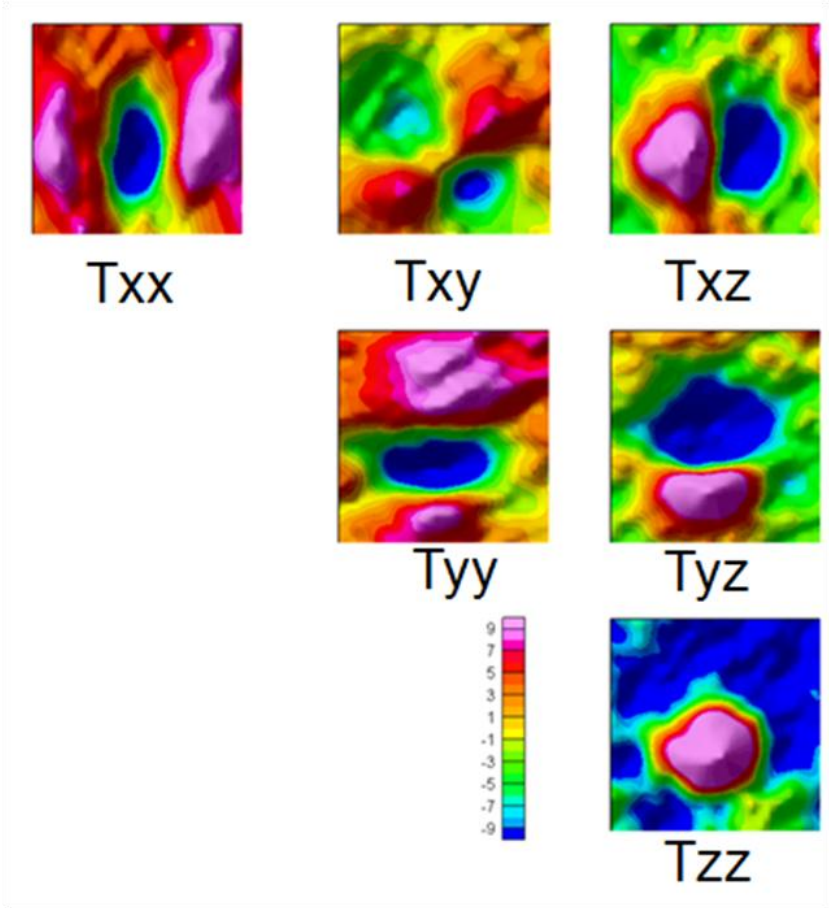

Figure 3.3 Full tensor gradiometry measurements over the caprock area of the Vinton salt dome.

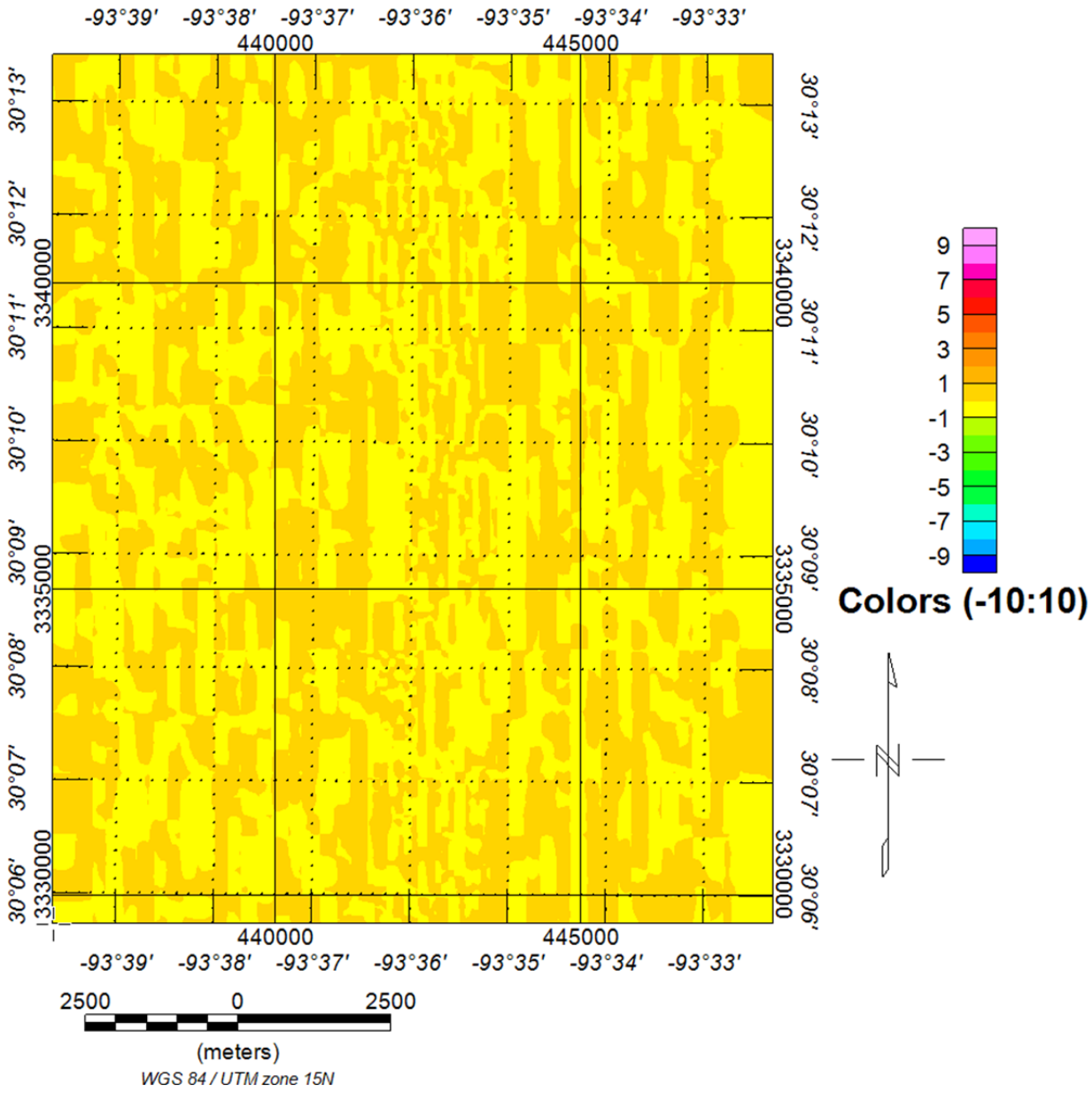

Figure 3.4 Noise analysis for measured FTG survey.

Chapter 4

Methods

4.1 Introduction

To detect and map gas reservoirs near the Vinton salt dome, the Full Tensor Gradiometry (FTG) data had to be terrain corrected and gridded. Terrain correction is necessary to compensate for undesired signal generated by changes in landscape topography. Gridding is necessary to fit the data to a regularized grid comparable to the grid output from the forward calculation algorithm. A two-part method was used to investigate the presence of gas reservoirs near the dome after processing. The first part is a forward modeling process where the dome signal is calculated for a model built from *a priori* information gleaned from seismic data, conventional gravity data, well logs, and VSP. The signal of the dome model was calculated for each gradient by a MATLAB program written with equations published by Okabe (1979) that is included in the appendix. The calculated signal is subtracted from the observed FTG data for each gradient to remove the effect of the salt dome for the corresponding gradient. It is assumed that by subtracting the salt dome signal the remaining signals should be indicative of gas reservoirs, faulting, or irregularities of the salt dome unaccounted for in the model. The second part of the method is the calculation of a range of attributes from the data after subtraction such as coherency, curvature, and invariants to detect discontinuities associated with residual anomalies.

Bell Geospace provided the several versions of the FTG data; free air, de-noised free air, and de-noised with terrain correction of 1.8 gm/cc applied. A terrain correction model was also

supplied if the user wished to apply a terrain correction with a different density. However the user is unable to apply de-noising after application of a new terrain correction. The FTG data are gridded to match the forward calculated signal from the salt dome model.

4.1 Full Tensor Gradiometry Processing

The FTG data had to undergo two processes before subtraction could take place. First, the terrain correction had to be checked and recalculated. Second a grid spacing and algorithm had to be chosen and applied to the data to provide evenly spaced values that could be directly compared to the calculated dome signal.

Terrain Correction. Initial observations of the data provided and preliminary subtractions raised concerns about the terrain correction. Elevation data used to derive the initial terrain correction came from the Shuttle Radar Topography Mission (SRTM) and had a 90 meter spatial sampling rate (Selman, 2008). The elevation data used for the terrain correction was contoured and overlaid on the Tzz gradient. It was observed that elevation highs matched Eötvös lows on the terrain corrected Tzz data. This indicated either the density was too large or the elevations used in terrain correction model derivation were too high or both. Additionally the initial subtraction of the calculated salt dome signal from the Txx and Txz component revealed a significant residual anomaly in the exact location of the hill on the northwest side of Grey Lake. A second elevation dataset derived from LIDAR (Light Detection and Ranging) surveys was obtained from the atlas program (http://atlas.lsu.edu/lidar) and sent to Bell Geospace for derivation of a new terrain correction model. After receipt of the new terrain correction model a range of densities from 1.0 gm/cc to 2.0 gm/cc were tested to find the correction with the least correspondence to the elevation data.

Gridding. In order to grid the data, the FTG values provided by Bell Geospace were loaded into Geosoft Montaj. Data for each gradient are in columns (channels in Montaj nomenclature). The gradients are sampled along flight lines at 1 sample per second. The flight lines are 250 meters apart away from the dome and 125 meters apart directly over the dome. Tie lines were 1 km apart. Maps supplied by Bell Geospace are based upon data gridded with a spacing of 1/2 or 1/3 the closest line spacing using a minimum curvature algorithm within Geosoft Montaj. Noise attenuation processing used by Bell Geospace depends on the wavelength chosen by the operator. The process correlates signal across all six components above a specified wavelength. Data that do not correlate across all six gradients were removed. The de-noised dataset provided by Bell has a cutoff wavelength of 125 meters (Selman, 2008). The Nyquist wavenumber can be calculated using the following equation:

$$\pi k_n^2 = 4k_{x^n}\, k_{y^n} \tag{4.1}$$

To use the noise-attenuated data provided by Bell with a 125 m wavelength cutoff the data would have to be gridded with 100 m or more spacing between nodes. For data that are not de-noised, the grid spacing can be reduced to 50 meters. Conservative signal estimates of faults, gas-charged fault blocks, and gas reservoirs show minimum wavelengths of 800 meters. A grid spacing of 100 meters was chosen to prevent loss of short wavelengths in case the signal wavelength was overestimated.

Upward Continuation. The gridded data contained a large number of randomly distributed, short wavelength anomalies that couldn't be correlated to any known subsurface structures. These events obscured larger residual signals and thus were classified as noise. Two methods could be used to reduce the influence of this noise; (1) using a larger grid spacing and

(2) upward continuation. Upward continuation was used to reduce noise contamination while retaining details in the data. Using a larger grid spacing may risk propagating noise and attenuating signal depending on where the grid nodes are located and the type of gridding method used. Upward continuation is an attenuation method whereby the power spectrum (S_0) of the field is attenuated by:

$$P(k) = S_0(k)\exp(-2kz_0) \tag{4.2}$$

Where P(k) is the attenuated power spectrum, k is the wavenumber, and z_0 is the height to which the wavefield is continued to. The upward continued wavefield is considered the same wavefield that would be observed at depth for the height value used to upward continue the field. Using this method incorporates the entire measured wavefield (Jacobsen, 1987). By using a small value height small amplitude anomalies are attenuated to the point where they do not influence the subtraction of the model from the measured data. Of course, the signal calculated from the model has to be at the same height chosen for the upward continuation of the observed data. In this study a height of 100 m was chosen for upward continuation since the measured signals where attenuation should be minimized are from subsurface features that start at a depth between 130 and 180 m (Eti, 2004). The reduction in noise can increase confidence that residual anomalies are more likely due to caprock signal not captured in the model.

4.2. Development of the Initial Model

The forward model was built using three inputs. (1) The caprock portion of the model (160 meters to 360 meters) was developed from a map drafted from conventional gravity data and well logs (Eti, 2004). (2) The salt portion of the model (360 meters to 2860 meters) was

derived from a seismic interpretation supplied by Rick Zoss, a contractor that worked for White Oak Energy. White Oak Energy had access to the seismic data as part of production activities near the dome. (3) Well log interpretations were also used to constrain the depth extent of caprock and salt where available. A density versus depth profile was used to establish the change in density contrast with depth for the model.

The model has a spatial extent 6.6 km north-south and 4.5 km east-west, which is larger than the dome, but smaller than the extent of the gradiometry data. The model was composed of 66 blocks in the east-west direction, 45 blocks in the north-south direction and 28 blocks in depth. Each block was 100x100x100m. The program has to calculate the contribution from a total of 83,160 blocks. The signal was calculated on a 200m x 200m grid. The grid was 70x70 nodes to get a 14km x 14km surface. Each block was assigned a density contrast based on the block's relationship with surrounding blocks at a particular depth. Blocks of surrounding sedimentary formations were assigned a value of zero. At each 100 m depth interval blocks designated as salt were assigned a density contrast value that was constant for each depth interval. The density contrast value changed based on a density-depth curve (Figure 4.1).

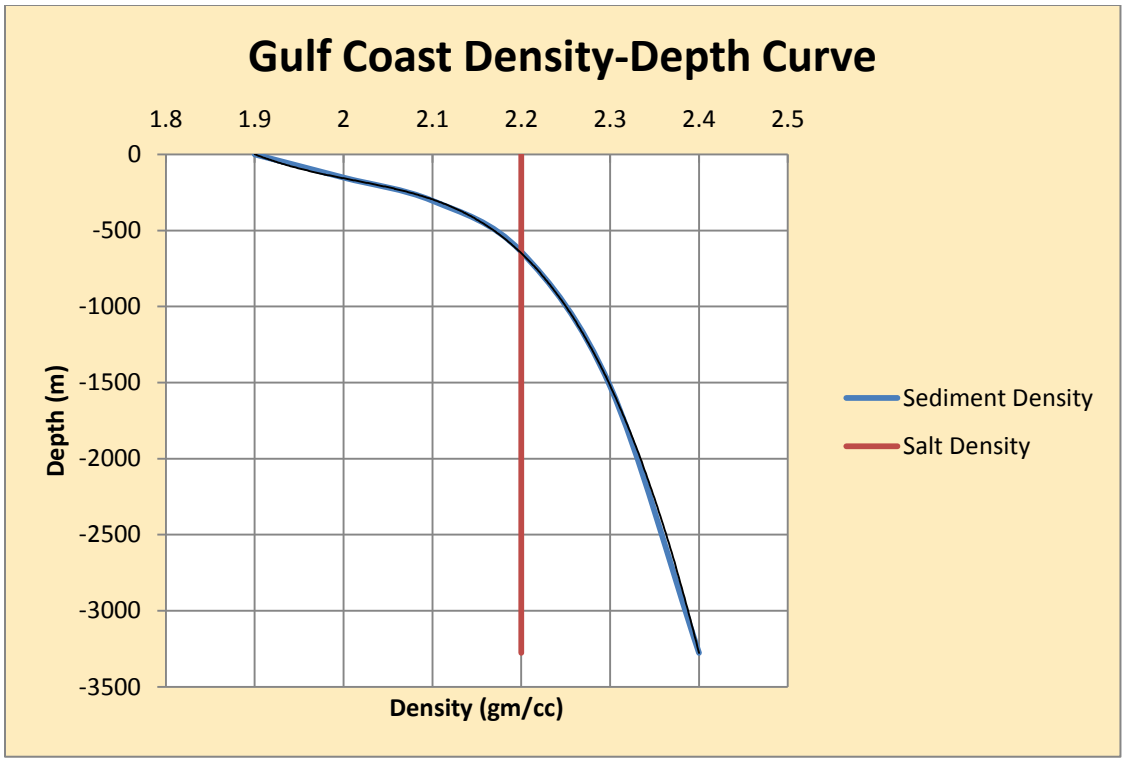

Figure 4.1 Gulf Coast Density-Depth Curve (modified from Nettleton, 1934)

Caprock. Extensive drilling in the area allowed the depth, thickness and areal extent of the caprock to be relatively well defined. A skewed pyramid shape with a peak at the southeast corner was used to simulate the geometry of the caprock. It extends from 160 m to 360 m in depth. It spans 1500 m east-west and 1100 m north-south. The south and eastern sides of the dome are the steepest ranging from 36˚ to 56˚. The north and west sides of the dome have a shallower gradient from 16˚ to 20˚ (Eti, 2004). A density of 2.75 g/cc has been assumed for the caprock, and a density of 1.9 g/cc is assumed for the sediment at a depth of 160 m. This produces a density contrast of 0.85 g/cc. with the surrounding sediment. At 360 m the sediment density is assumed to be 2.0, which creates a density contrast of 0.75 g/cc (Table 4.1).

Salt. There is more uncertainty for the salt than for caprock due to sparse well control and bottom hole depths that are shallower than the top of salt. The salt portion of the model

relied more on seismic data than well logs. Within the model the salt started at 460 meters depth and reached a maximum depth of 2860 meters. The density contrast values ranged from +0.1 gm/cc at 460 meters depth to -0.02 gm/cc at 1160 meters, just below the crossover depth. The maximum negative density contrast at 2800 meters depth is -0.17 gm/cc (Table 4.1).

Depth (m)	Salt Density (g/cc)	Sediment Density (g/cc)	Density Contrast (g/cc)
160	2.75	2.00	0.75
260	2.75	2.00	0.75
360	2.75	2.10	0.65
460	2.20	2.10	0.10
560	2.20	2.10	0.10
660	2.20	2.15	0.05
760	2.20	2.15	0.05
860	2.20	2.15	0.05
960	2.20	2.22	-0.02
1060	2.20	2.22	-0.02
1160	2.20	2.22	-0.02
1260	2.20	2.25	-0.05
1360	2.20	2.22	-0.02
1460	2.20	2.22	-0.02
1560	2.20	2.27	-0.07
1660	2.20	2.27	-0.07
1760	2.20	2.27	-0.07
1860	2.20	2.33	-0.13
1960	2.20	2.33	-0.13
2060	2.20	2.33	-0.13
2160	2.20	2.33	-0.13
2260	2.20	2.33	-0.13
2360	2.20	2.33	-0.13
2460	2.20	2.37	-0.17
2560	2.20	2.37	-0.17
2660	2.20	2.37	-0.17
2760	2.20	2.37	-0.17
2860	2.20	2.37	-0.17

Table 4.1. Density and density contrast values used to populate each layer of the model.

After subtraction of the salt/caprock model from the observed data, residual signals are compared with forward calculations of signal from gas-charged reservoirs. Models of gas reservoirs were developed from gas production information available through the SONRIS database (sonris.com). A MATLAB program based on equations for modeling gradiometry for 3D structures was used to calculate the gradients for gas on brine contacts to understand their expression.

4.3. Forward Model Signal Calculation and Subtraction

The salt dome signal is calculated from a forward model in MATLAB using equations published by Okabe (1979). The input to the program is an array with three dimensions corresponding to x, y, and z in a model space. X values increase in the east direction, Y values increase in the north direction, and Z values increase with depth. Each cell in the array can be populated with a density value or a density contrast value. If density values are used, calculated signal will have unrealistic values at the edges of the model due to the change from some positive density value to zero. For this study the model was populated with density contrast values to avoid anomalous values at the edges of the model space. At each z-layer in the model, the cells designated as salt are populated with the difference between salt density and the average density of sediment at that depth based on a derived density depth curve. The model used in this study is an array with size 66x45x28, but can be expanded as needed. The time needed for the program to complete the calculations is increased with an increase in array size in any direction or a decrease in observed surface node spacing.

The program calculates the signal for each cell in the array. The program considers each cell in the array as a cube with x,y, and z coordinates at the eight points of the cube. The program calculates the contribution of each cell in the x-direction, then the y-direction, then the

z-direction. The contribution of each cell is summed before the program calculates the contribution from the next cell. In this way the signal for the model is constructed until the program finishes calculating the signal for each cell in the array.

The program yields two outputs. The first is a grid of calculated values for a specified gradient in matrix form. Cells in the matrix correspond to nodes separated by a specified number of units decided by the user. For this study, a 70x70 grid of nodes 200 meters apart in x and y were used. The second output is a three column array that lists the x, y, and calculated gradient signal value relative to the input model dimensions. The first output is useful for a quick check of the values calculated for the model so adjustments to the program can be made quickly without going through the full subtraction process. The second output is assigned UTM coordinates that correspond to the expected position of the calculated observation surface on the Earth's surface. To georeference the calculated output with the measured data 439,440 meters was added to each x-coordinate value and 3,332,750 meters was added to each y-coordinate value. These values were derived by matching the maximum positive values of the calculated signal and the measured signal through trial and error. The regularized observation surface is considered georeferenced at this point. It is loaded into Geosoft and subtracted from the supplied field measurements for the appropriate gradient. The result is considered a map of the gradient with the salt dome signal removed.

4.4. Attributes

Attributes have been used in many seismic studies to map discontinuities in seismic data associated with faults and small scale features like sand channels and faults. Calculation of attributes is a robust method that has been applied to seismic, surface elevations, and gravity gradiometry datasets Attributes used in previous studies include horizontal and rotational

invariants that emphasize different aspects of subsurface structures such as gross dimension and lineaments. Rotating the data about the down axis has also been used to highlight trends in the data. In this study coherency is derived from the data to see if the attribute is useful with FTG data (Bergbaur and Pollard, 2003; Pearce et al., 2006; Li, 2009; Mataragio and Kieley, 2009).

Invariants. Attribute derivations are applied to FTG data to combine gradients into a single tensor attribute (Pederson and Rasmussen, 1990; Murphy and Brewster, 2007).

Rotational invariants and horizontal invariants were derived from FTG data and used by Mataragio and Kieley (2009) to detect small-scale features associated with the Budgell's Harbour Gabbro on the coast of Notre Dame Bay in Canada. Two rotational invariants were used to detect intrusions within the host gabbro. These two attributes were also used by Murphy and Brewster (2007) in the Nordkapp Basin, a salt basin, offshore Norway. In their case R-1 was used to map gross regional stratigraphy, and R-2 was used to detect the shape of anomalous bodies such as fault blocks and salt bodies. They were calculated using:

$$R-1=((TxxTyy+TyyTzz+TxxTzz)-(Tyx^2+Tyz^2+Tzx^2)) \quad (4.2)$$

$$R-2=(Txx(TyyTzz-Tyz^2)+Txy(TyzTxz-TxyTzz)+Txz(TxyTyz-TxzTyy)) \quad (4.3)$$

Horizontal invariants revealed radial fractures around the intrusion. Using only the horizontal gradients decouples the attribute from the influence of vertical Tzz gradient. This is important for reducing the influence of burial depth on the attribute (Murphy and Brewster, 2007). They were calculated using:

$$H-1=\sqrt{(Txy^2+\left(\frac{Tyy-Txx}{2}\right)^2)} \quad (4.4)$$

$$H - 2 = \sqrt{(Txz^2 + Tyz^2)} \quad (4.5)$$

The rotational and horizontal invariants can be calculated without the need for gridding the data. These attributes were used to detect changes in density within an intrusion. In this study the invariants are used to find changes in density adjacent to a salt dome.

Coherence. Coherence is another attribute used in seismic reflection studies to detect faults from discontinuities along horizons (Bahorich and Farmer, 1995; Gersztenkorn and Marfurt, 1999). Coherence is derived by calculating the normalized cross-correlation between a central window and four adjacent windows. A script was written in MATLAB to produce coherence from gridded gradiometry data. Grid spacings tested were 250m and 100m. Five windows were used to calculate the coherence; a central window and four adjacent windows to the northeast, southeast, southwest, and southeast (Figure 4.3). Each window contained 3x3 data points. The mean and standard deviations were calculated for all five windows. A normalized cross-correlation coefficient between the central window and each adjacent window was calculated by the following equation:

$$\frac{1}{9-1}\sum_{x,y} = \frac{(f(x,y) - \bar{f})(t(x,y) - \bar{t})}{\sigma f \sigma t} \quad (4.6)$$

Where $\bar{f}$ is the average and σ_f is the standard deviation of the adjacent windows and $\bar{t}$ and σ_t are the average and standard deviation of the central window.

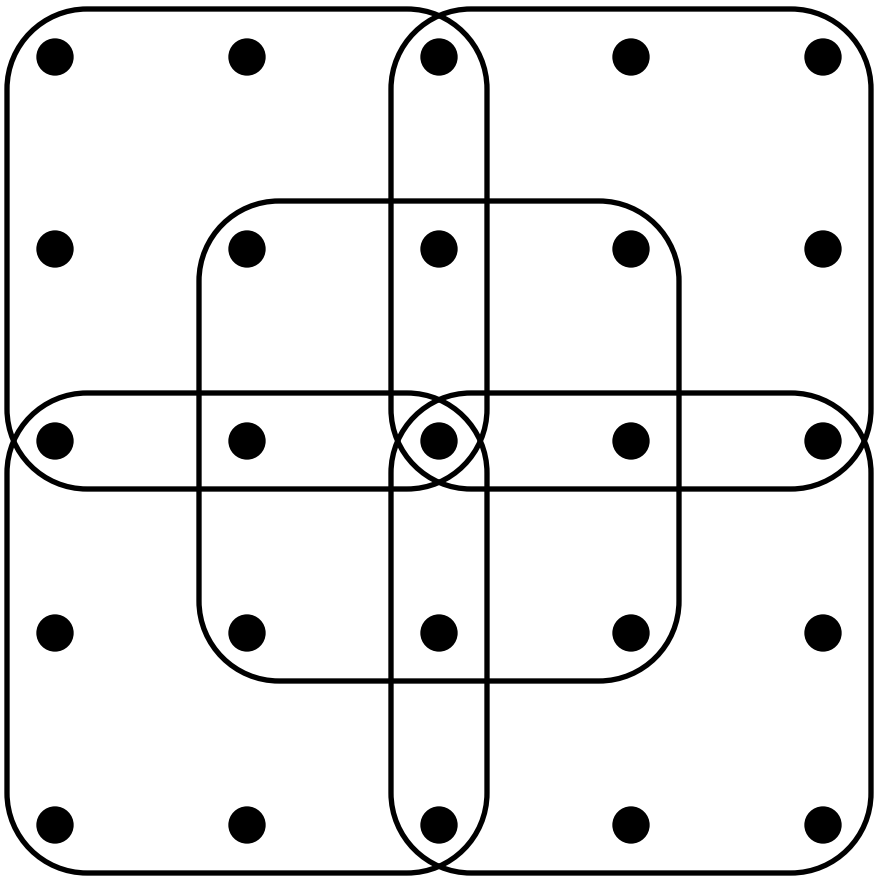

Figure 4.2 Windows used in calculating coherence values.

One normalized cross-correlation coefficient was calculated for each window. The fourth root of the product of all four cross-correlation coefficients was taken to yield the coherence for the center of the central window. The windows move one grid interval and the values are calculated again. The coherence is not calculated at the edge due to the window restriction (Li, 2009).

Data Rotation. Each FTG component can be rotated to highlight features with different orientations (Pederson and Rasmussen, 1990). The measured data were loaded into Geosoft Montaj using the North-East-Down (NED) coordinate convention. The choice of coordinate convention is an arbitrary one, but NED is one of the most common. Subsurface structures

rarely align with either the north or east directions. By rotating the data, measured energy is better aligned with subsurface structure orientation. This can provide more distinct anomaly boundaries for mapping and comparisons with other interpretations. The data are rotated using the following equations:

$$Txz' = Txz\cos\theta + Tyz\sin\theta \tag{4.7}$$

$$Tyz' = -Txz\sin\theta + Tyz\cos\theta \tag{4.8}$$

$$TyyMxx = (Tyy - Txx)/2 \tag{4.9}$$

$$Txy' = Txy\cos 2\theta + TyyMxx\sin 2\theta \tag{4.10}$$

$$TyyMxx' = -Txy\sin 2\theta + TyyMxxcos2\theta \tag{4.11}$$

$$Txx' = -\frac{Tzz}{2} - TyyMxx' \tag{4.12}$$

$$Tyy' = -Tzz - Txx' \tag{4.13}$$

where θ is the angle around the down axis to which the data are rotated.

Chapter 5

Results

The results can be divided into two categories. The first are the results of the forward modeling and subtraction. This is not just limited to the final model, but includes how the model was modified to obtain the final result. Subsequent iterations of the model used *a priori* information to guide modifications. The second category of results comes from deriving attributes from the survey data after subtraction of the forward model, which is called the residual.

5.1. Model Results

A model is generated as input to the forward calculation algorithm. The result of the forward calculation algorithm is obtained for each gradient component and subtracted from the corresponding field data to obtain a series of maps of residual anomalies. The first set of model tests focused on obtaining an accurate estimate of signal from the caprock. It was the closest body to the surface, had the highest density contrast with surrounding sediment, and dominated the measured FTG data over the center of the dome. Modeling the caprock was also done to decrease time between iterations of the forward model calculation. Calculating the signal for the entire salt body, which had 28 layers of 100m thick blocks, took an average of four hours, while calculating the signal for only the caprock, which had only three layers, took ten minutes.

The initial model was constructed utilizing a top caprock interpretation based on conventional gravity and well logs (Eti, 2004). The bottom of the caprock was fixed at 460m depth. The model assumed a caprock density of 2.75 g/cc. Four tests were conducted using a three layer caprock model. All three layers were populated with the same same sediment density contrast for each test. Adjacent sediment densities of 2.00 g/cc, 2.15 g/cc, 2.20g/cc, and 2.25 g/cc were used. The density contrast is treated as an average of formation densities over a given depth interval based on the observation of scatter in the well log densities. The best fit was 2.20 g/cc with a residual difference of -0.91 Eo at the peak of the caprock on the Tzz gradient (Figure 5.1). This density would indicate that the density crossover depth occurs at the same depth as the caprock. Significant positive Eötvös anomalies remained after the subtraction, especially in the Txx (Figure 5.2) and Txz gradients. The supplied elevations taken from the Shuttle Tomography Mission (STS) were contoured and overlaid on these gradients. High correspondence was observed between elevations and the Tzz gradient contours. The elevations used in the terrain correction calculation from the STS were then compared with topographic quadrangles and available LIDAR data. There were large differences in topography between the STS, the quadrangles, and the LIDAR data. The LIDAR data and the quadrangles had similar topography.

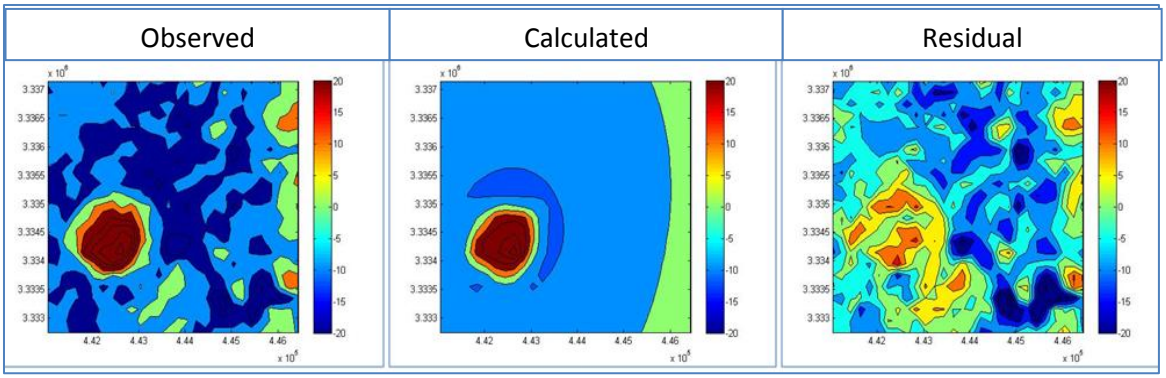

Figure 5.1 Tzz field data, calculated dome signal, and difference as viewed in MATLAB.

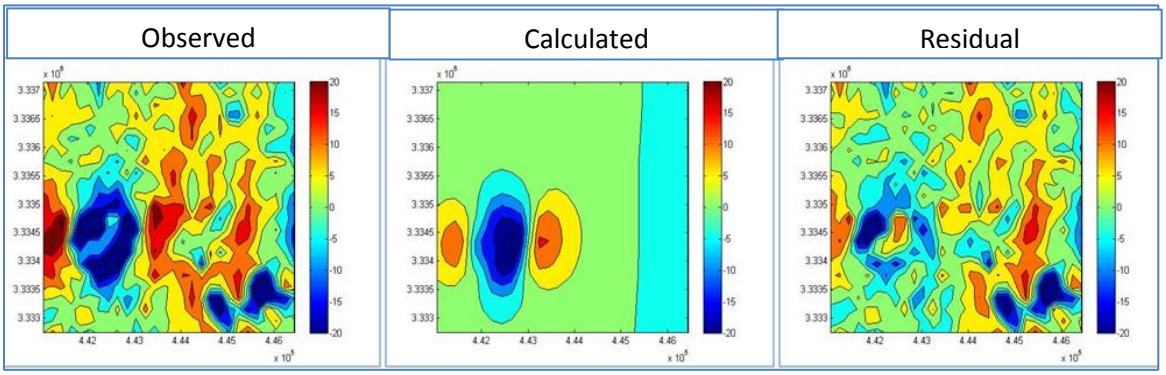

Figure 5.2 Txx field data, calculated dome signal, and difference as viewed in MATLAB.

Bell Geospace Inc. used a proprietary FTG tailored algorithm for calculating the terrain correction for each gradient of the FTG survey. When a new terrain correction based on the available LIDAR data was requested they were kind enough to supply it. The gridded terrain correction was applied to the de-noised data.

The supplied terrain corrections were calculated so that a single scalar could be applied to adjust the terrain correction to a suitable near surface density value. A terrain correction using a density of 1.8 g/cc was applied to the data since it was used previously. When the LIDAR elevations were overlaid, the contours again matched with the Tzz gradients indicating the terrain correction was inducing errors in the data associated with the elevations. New terrain

corrections tests were derived and applied that ranged in density from 1.0 g/cc to 2.2 g/cc at 0.2 g/cc increments. The data that showed the least correspondence to the topography was obtained with a density of 1.4 g/cc, which was corroborated with information from the Natural Resources Conservation Service about soil density data in the Gray Lake area. This shallow density is also supported by tomography work done on VSP data adjacent to the dome (Kisin, 2003).

Due to the change in the terrain correction, a new set of model tests for the caprock were run with density contrast values of 0.75 g/cc, 0.95 g/cc, and 1.35 g/cc to simulate adjacent sediment densities of 2.0 g/cc, 1.8 g/cc, and 1.4 g/cc with a constant caprock density of 2.75 g/cc. The 2.0 g/cc sediment density presented the closest match on the 100 m upward continued maps.

The combined caprock and salt dome model were forward calculated at the appropriate height of 100 m to match the upward continued surface. A sediment density of 2.0 g/cc adjacent to the caprock eliminated the positive signal in the location of the caprock without inducing a negative Eötvös residual on the Tzz gradient. The density-depth function was modified to start at 2.0 g/cc at the top and increase with a fixed caprock density of 2.75 g/cc and a fixed salt density of 2.0 g/cc. Forward calculations were computed for each gradient and subtracted from the data at 100m upward continued surfaces.

Forward calculations for the caprock, above crossover, and below crossover salt were derived. Below the caprock, to a depth of 2800 m, the geometry of the model was constructed using a top salt interpretation developed from well log salt picks and seismic data available to White Oak Energy and developed by an independent consultant. The initial density contrast

function assumed a linear increase in sediment density from 2.0 gm/cc to 2.2 gm/cc over a depth interval from 160m to 1160m. It also assumed a 400 meter caprock of 2.75 gm/cc density and underlying salt of 2.17gm/cc density. The final contrast function had a 0.75 gm/cc density contrast between the caprock and the surrounding sediment and the underlying salt contrast with the sediment decreased from 0.1 gm/cc to 0.05 gm/cc (Table 4.1) above the crossover depth.

5.2. Reservoir Model Results

A simple model was constructed to simulate a gas-charged reservoir. The model was composed of a single 100x100x100 m block populated with a -0.3 g/cc density contrast. The signal for the block was calculated at a number of depths for the six gradients available (Figure 5.3). This provided a qualitative guide for comparison with the residual images.

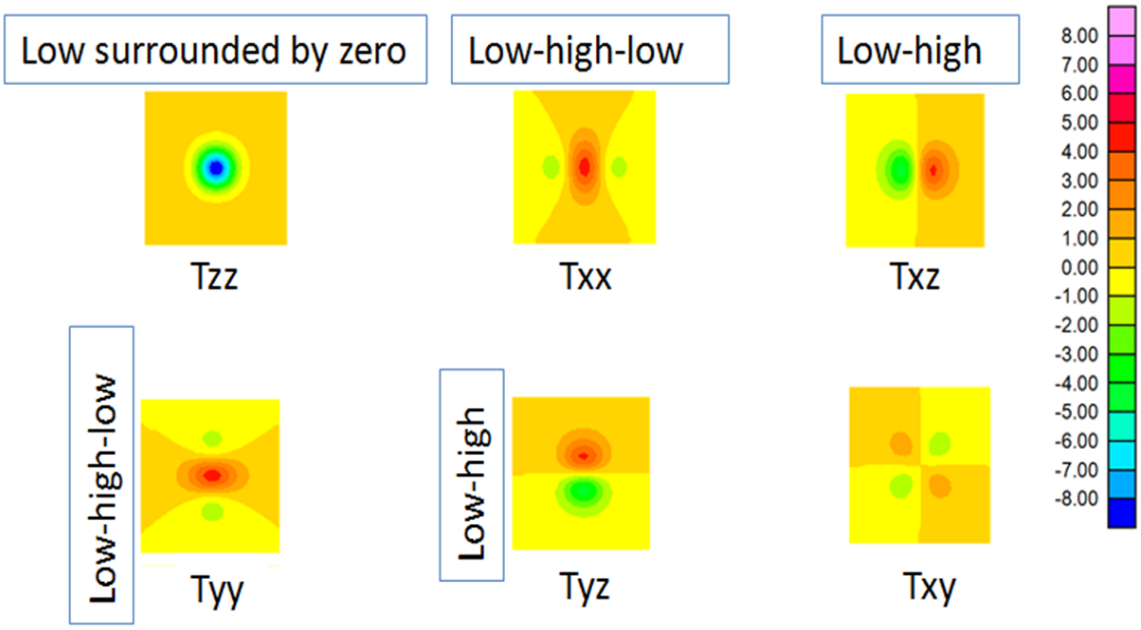

Figure 5.3 Qualitative guide for assessing whether residual signals may indicate a gas reservoir.

A rough model of gas production was also constructed using production records (SONRIS database access, 2012). At a well location where a production depth was recorded a 100x100x100 m block was inserted into a volume at the production depth. After populating the model with all known gas production the FTG signal was calculated. Without more detailed information on production intervals and volumetrics this model remains a rough approximation and only gives a negative anomaly of between -1 and -2 Eötvös (Figure 5.4).

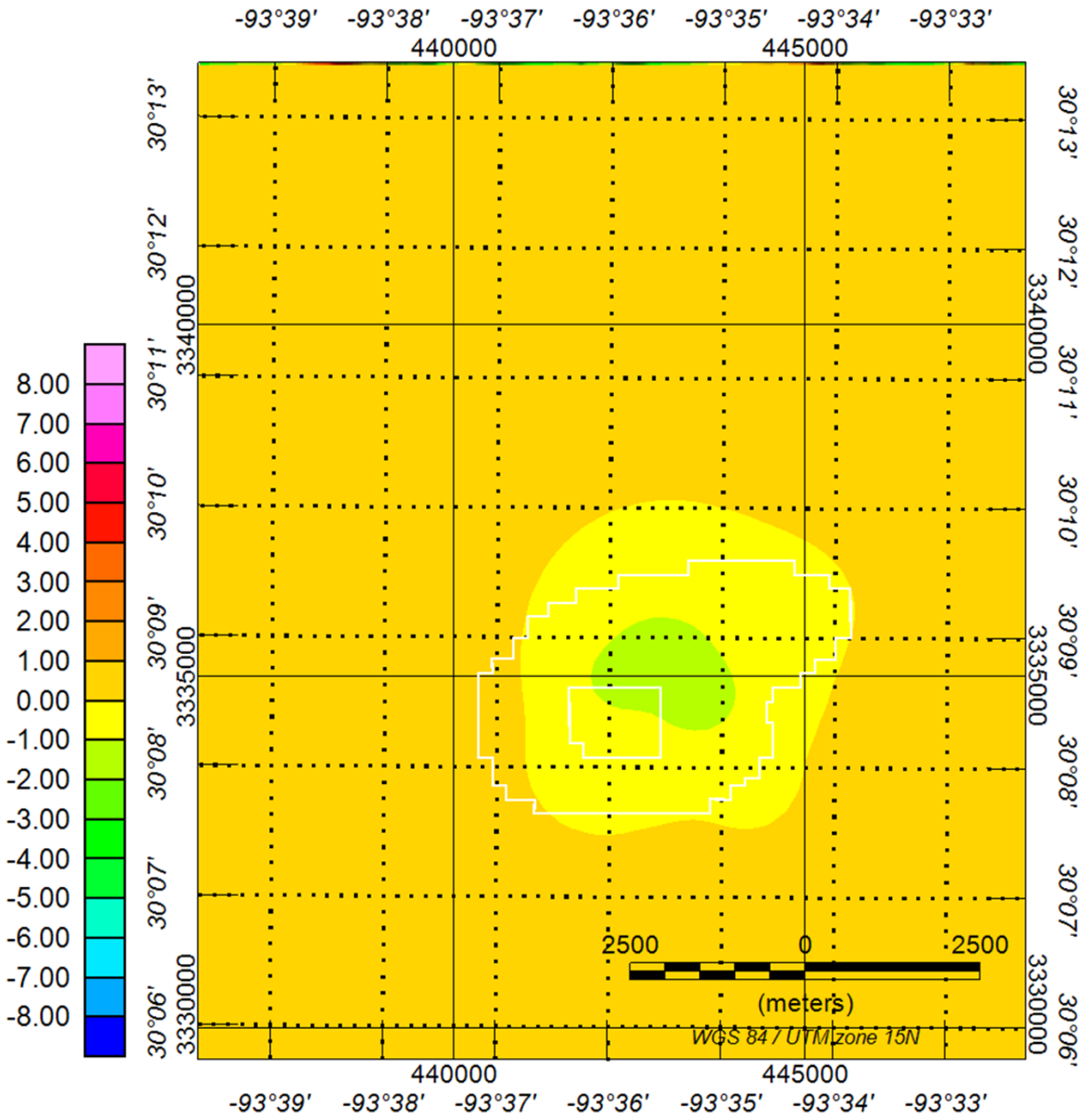

Figure 5.4 Forward calculation of Tzz for known production (SONRIS database access, 2012).

5.3. Subtraction Results

The expected response for the Vinton salt dome was calculated for all six components of the gravity gradient tensor at 100m above the observation level. This response was subtracted from the gridded survey upward continued by 100m. The difference revealed several residual anomalies around the dome. Residual anomalies can be explained in one of three ways; either

the expected signal from the dome was not properly modeled, signals from other source bodies were present, or noise contaminated the data.

The results of subtracting the calculated salt dome signal from the gridded gradiometry data are shown in Figures 5.3 through 5.8. The residual anomalies vary with each component. After subtraction of the salt the Tzz component still shows a significant positive residual on the south and east edge of the caprock (Figure 5.3c). There are also a number of negative anomalies outside of the modeled salt dome signal. The largest negative anomaly is northeast of the dome. The best fit between the salt dome signal and the field data is on the south and west sides of the dome. Many negative closures are reduced to less than 5 Eötvös magnitude.

The Txx and Txz components highlight north-south oriented features. On the Txx field data there is a significant positive anomaly 2 km northwest of the dome, and a 5km long positive feature on the east side of the dome that is parallel to a shorter feature 1 km to the east (Figure 5.4b). After subtraction of the salt dome signal from the Txx component the northwest positive feature remains (Figure 5.4c). The 2 km long feature on the east side of the dome is attenuated immediately east of the dome, but 3 km of the linear feature remains unaltered northeast of the dome. The parallel feature 1km east is mostly unaltered by the subtraction.

The Txy gradient marks corners of a subsurface body. Arrows in Figure 5.7b point out the corners of the caprock of the dome. The area over the caprock is marked by a pair of highs on the northeast and southwest corners and a pair of lows on the northwest and southeast corners. The northeast positive for both the calculated signal and the measured field are higher amplitude than the southwest positive. The southeast negative is also higher amplitude than the northwest negative, but the difference is more pronounced on the measured data than the

calculated signal. Low amplitude, long wavelength features can be observed on the diagonal corners of the measured field. The observed and residual images are dominated by a low amplitude, diagonal fabric. Figure 5.5c shows that after the subtraction the caprock area is within +/-5 Eötvös. The area northeast of the caprock shows the highest magnitude residuals. The broad areas on the corners of the survey show only minor changes. The Txy field in general has the lowest amplitude values of the six gradient components.

The Txz component has a clear positive anomaly on the west side of the caprock and a negative anomaly on the east side of the caprock (Figure 5.6b). There are two trends that are longer with lower magnitude but opposite polarity from the caprock signal. The east side of the survey is dominated by a 10 km long positive anomaly. The west side has a shorter 7 km long negative anomaly that appears to have a lower magnitude. After subtraction a lot of the signal associated with the caprock is attenuated (Figure 5.6c). The positive anomaly on the west side of the dome is reduced and split into a pair of positive anomalies. The negative anomaly on the east side is reduced to less than -7 Eötvös. The 10 km trend on the east side of the survey is narrowed, but remains higher than 9 Eötvös. The trend on the west side is shortened to 5 km but remains lower than -9 Eötvös. The subtraction highlights a positive magnitude anomaly on the southwest side of the dome that trends northeast-southwest.

The Tyy and Tyz components show east-west trending features, but the data character is not as similar compared to the Txx and Txz components. The Tyy component shows an asymmetric pair of positive anomalies to the north and south of the caprock centered on a negative closure (Figure 5.7b). The caprock is marked by the negative closure. After subtraction the trend on the south side is reduced to less than 5 Eötvös while the trend on the north side is reduced to 8 Eötvös at its maximum (Figure 5.7c). The negative closure over the caprock is

reduced and split in half by a small positive anomaly. A pair of lineations appear on the north and south sides of the caprock oriented northeast-southwest.

The Tyz gradient is used to mark the center of mass for an object. The Tyz gradient of the Vinton survey is split in half with a dominant positive background on the north side and a negative background on the south side (Figure 5.8b). Immediately over the caprock there is a negative closure on the north side and a positive closure on the south side. After subtraction the positive closure on the south side is attenuated with values less than 5 Eötvös (Figure 5.8c). There is also a small circular feature within the positive part of the anomaly. The negative anomaly on the north side remains lower than -9 Eötvös. Outside the area of the caprock there are a lot more zero values after subtraction than before.

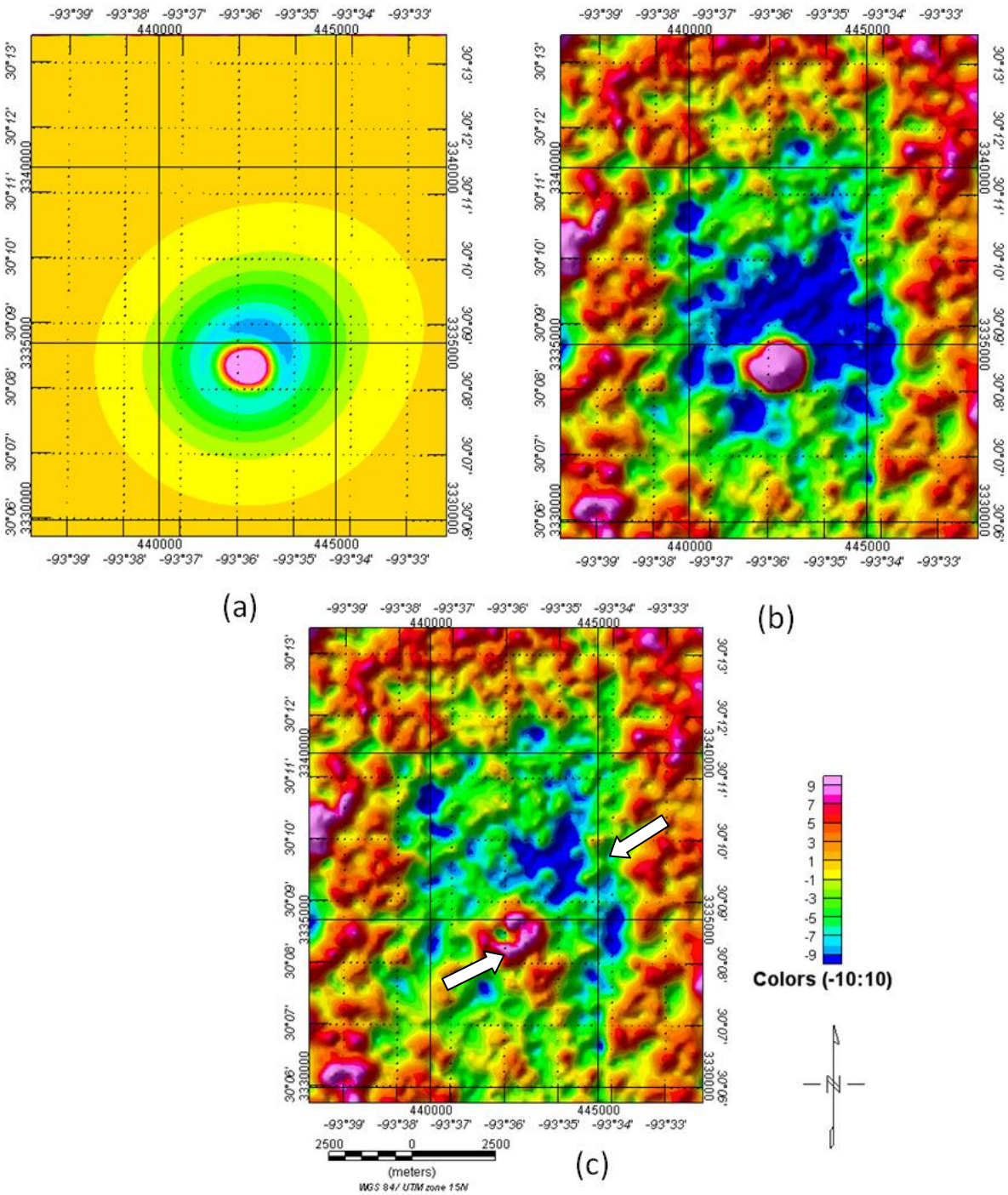

Figure 5.5 Tzz a) salt body model signal calculated 100m above observation surface, b) field measurements 100m upward continued, c) residual difference between both. Arrows illustrate areas of interest highlighted in the text.

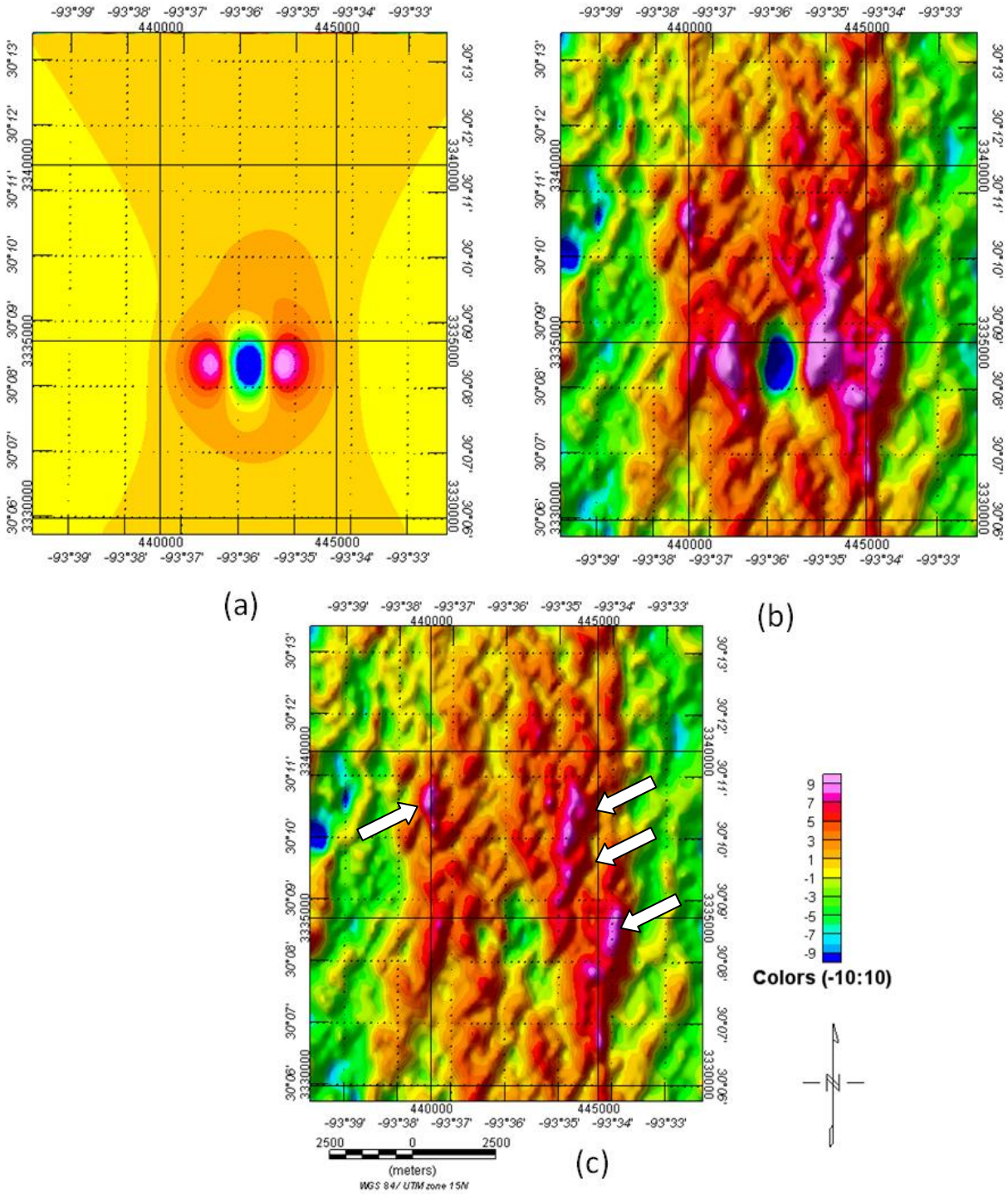

Figure 5.6 Txx a) salt body model signal calculated 100m above observation surface, b) field measurements 100m upward continued, c) residual difference between (a) and (b).

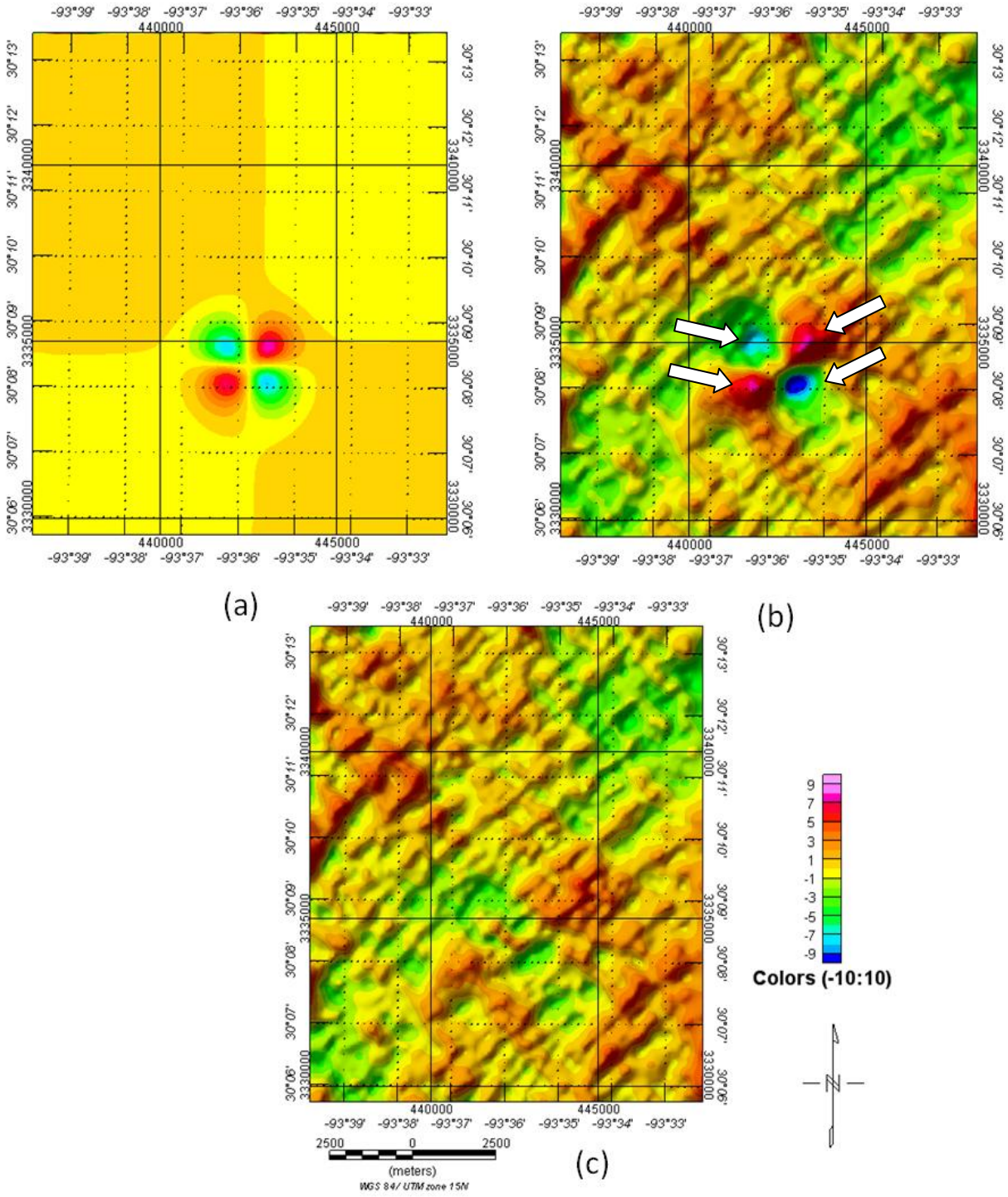

Figure 5.7 Txy a) salt body model signal calculated 100m above observation surface, b) field measurements 100m upward continued, c) residual difference between (a) and (b).

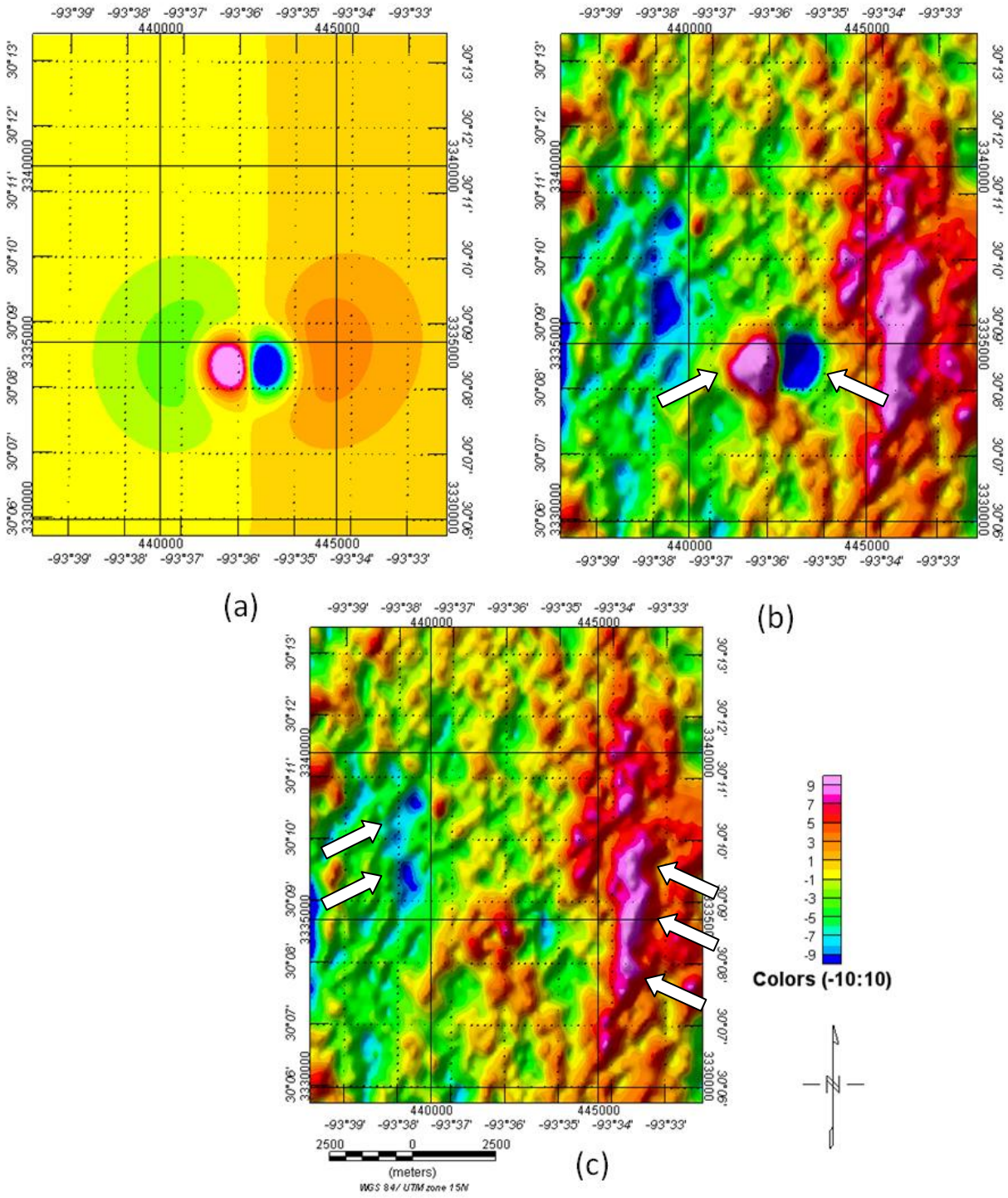

Figure 5.8 Txz a) salt body model signal calculated 100m above observation surface, b) field measurements 100m upward continued, c) residual difference between (a) and (b).

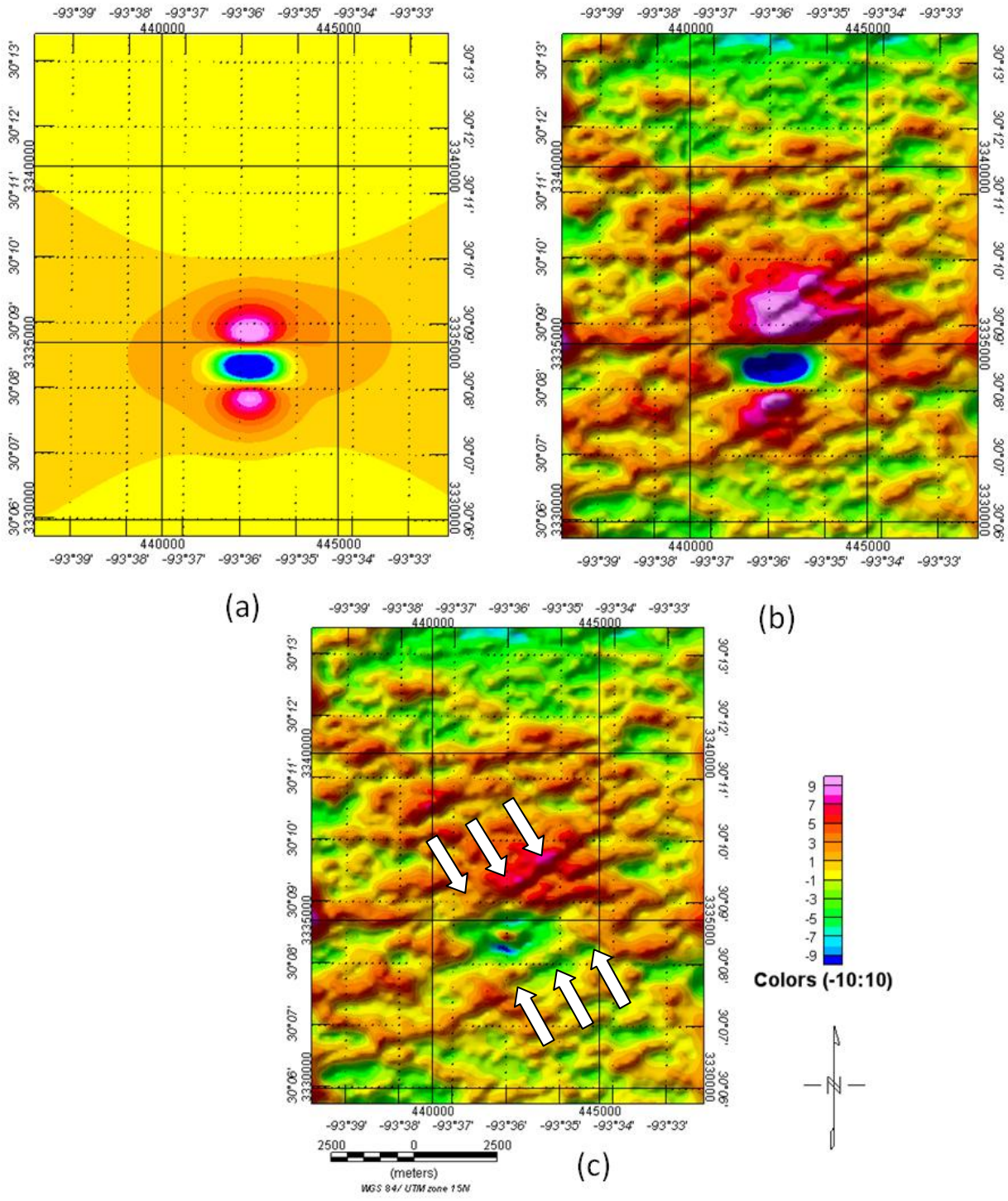

Figure 5.9 Tyy a) salt body model signal calculated 100m above observation surface, b) field measurements 100m upward continued, c) residual difference between (a) and (b).

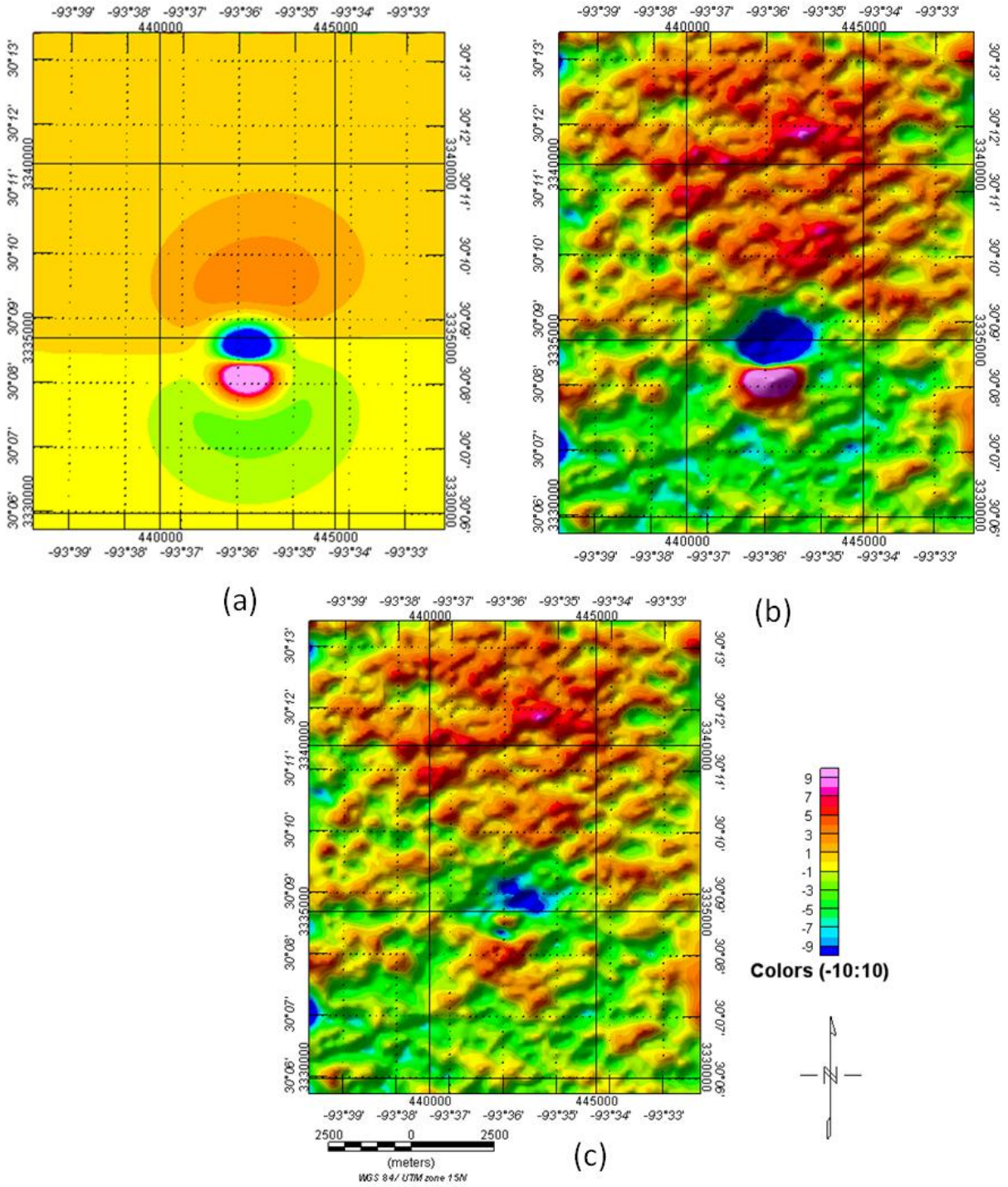

Figure 5.10 Tyz a) salt body model signal calculated 100m above observation surface, b) field measurements 100m upward continued, c) difference between (a) and (b).

5.3. Attributes

The residual maps were used to derive a number of attributes; two horizontal attributes, two rotational attributes, and a coherency attribute for each gradient. All the gradients except for Tzz were rotated about the vertical axis in 45 degree increments. They can be viewed in Figures 5.9 to 5.24. Warm colors on the coherency plots indicate areas with high coherence, and low coherency areas (where discontinuities would be expected) are indicated with cool colors.

Horizontal Invariants. The invariants present a wide variety of images. The H-1 and H-2 invariants were used to detect radial features in an igneous geologic setting (Mataragio and Kieley, 2009). The expected result of deriving these attributes for the Vinton FTG data is to emphasize linear trends caused by faults. This should be recognizable on the northeast and south sides of the dome where a lot of faulting has been mapped (Coker, 2006). The H-1 invariant shows isolated positive amplitude anomalies that don't seem to follow a particular trend (Figure 5.11). The only feature that really stands out is a broad ridge on the north side of the image.

The H-2 invariant has two high magnitude trends that run north-south on either side of the survey and are connected with a lower amplitude, discontinuous trend on the north side of the image (Figure 5.16). On the north side of the caprock model outline there is a broad high amplitude anomaly. The ridge observed on the H-1 Invariant is present on the H-2 image as a narrow trend of high amplitude anomalies on the north side of the image.

Rotational Invariants. In the Mataragio and Kieley (2009) study the R-1 and R-2 invariants were used to find intrusions within an igneous host. The rotational invariants were

used in the Nordkapp basin to delineate salt bodies (Murphy and Brewster, 2007). The rotational invariants are expected to highlight boundaries of the salt. The R-1 invariant has similar positive trends as the H-2 invariant on the east and west side of the image (Figure 5.13). There is a group of clearly defined negative anomalies consistent with anomalies observed on the residual Tzz component.

The R-2 invariant is dominated by negative magnitude anomalies (Figure 5.14). Negative anomalies are in similar locations as those seen in the R-1 image, but are much broader and have less clearly defined boundaries. The caprock outline is bounded on the north and south by a broad positive anomaly that trends in the northeast-southwest direction.

Coherence. All the coherence images have a "wormy" appearance with very few distinct boundaries. The Tzz contains the most high coherence events of the six images, but the events are discontinuous. There is only one discontinuous trend on the north side of the image (Figure 5.15).

Txx and Tyz show rapid changes in coherence on the south side of the caprock. Areas of high coherence are concentrated near residual anomalies that are visible in the difference plots in Figure 5.13 to 5.24. Gas production was plotted on the invariants to see if there was a link between the two. Gas production on the south side of the dome is more prominent on the coherency after subtraction of the modeled salt signal, and appears in the Tzz, Tyy, and Tyx. Rapid changes in coherence appear to be parallel to the component direction. Txx does not show low coherency on the north and south side of the dome, but the component emphases features that trend east-west. Rapid changes are perpendicular to the component direction.

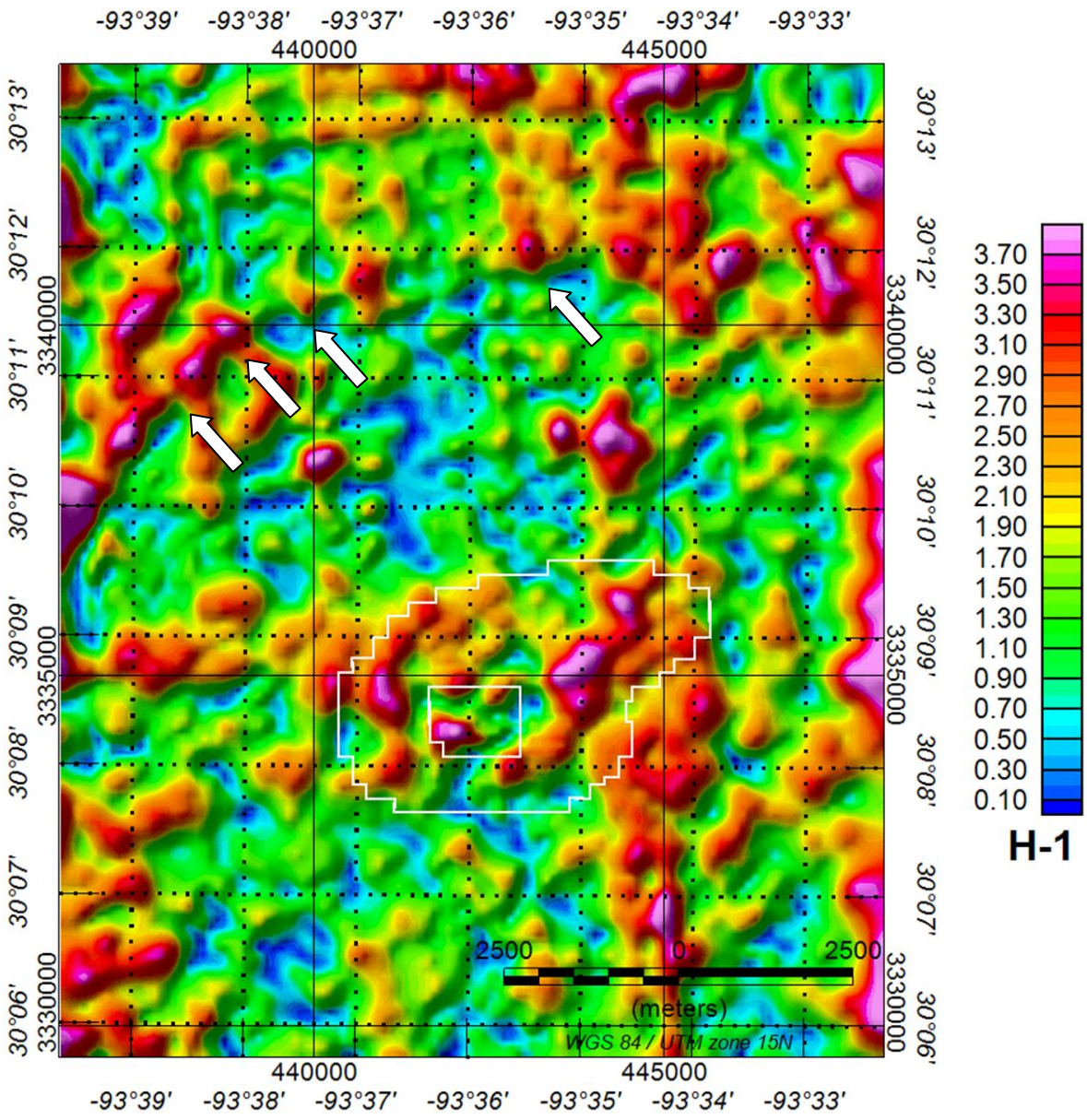

Figure 5.11 H-1 Invariant after subtraction. Outer white outline is salt model maximum extent. Inner white outline is maximum extent of caprock.

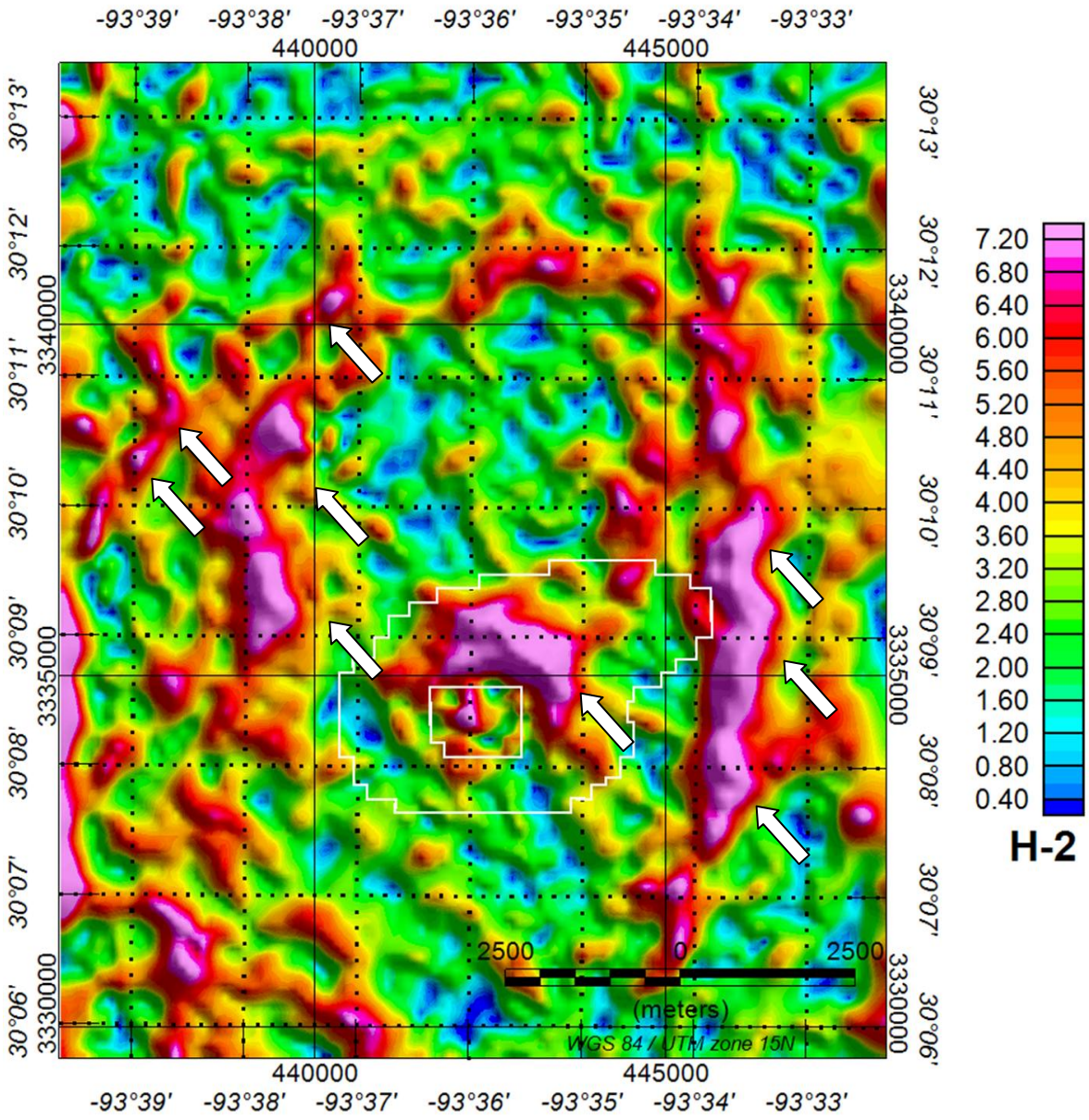

Figure 5.12 H-2 Invariant after subtraction. Outer white outline is salt model maximum extent. Inner white outline is maximum extent of caprock.

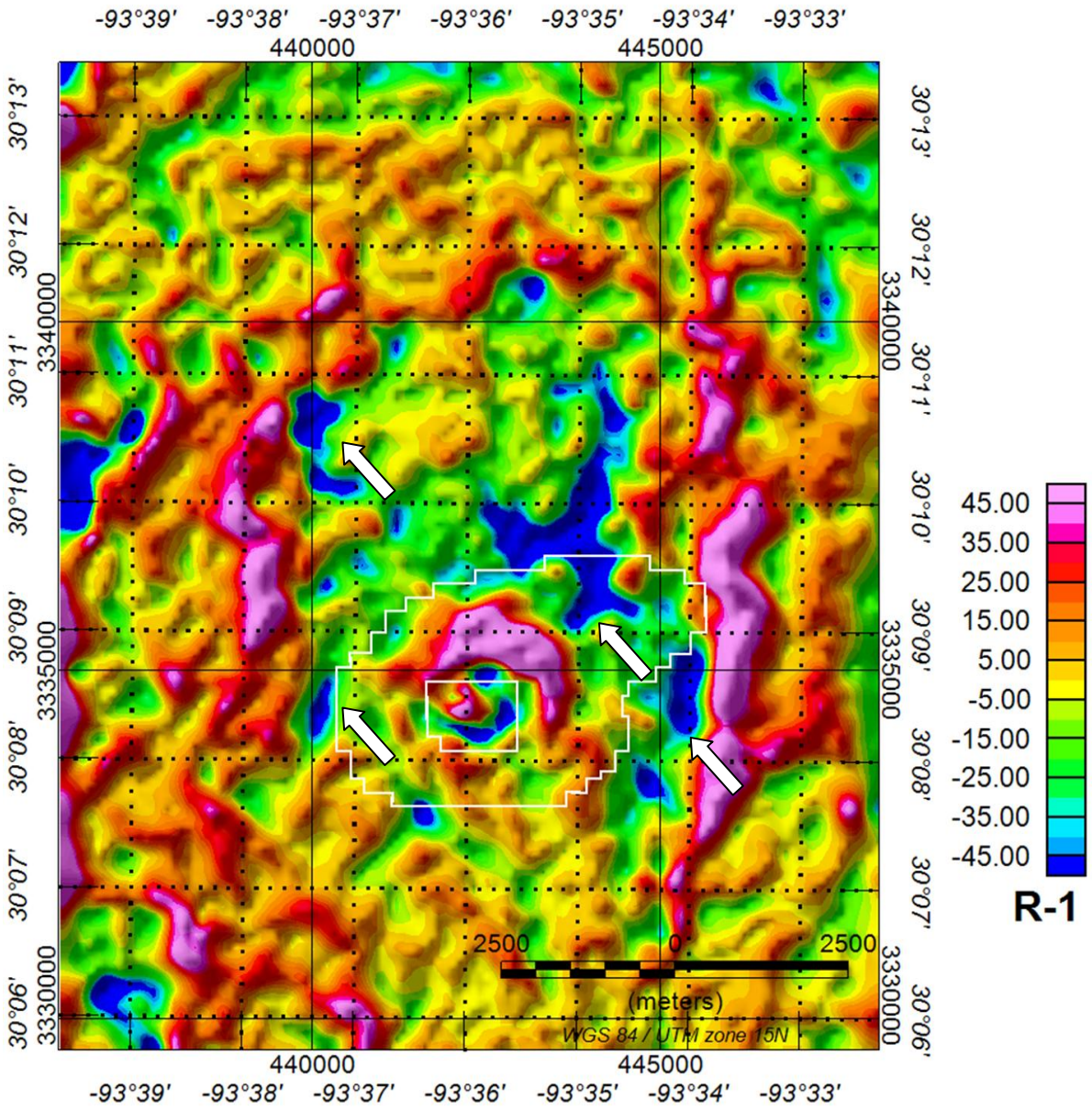

Figure 5.13 R-1 Invariant after subtraction. Outer white outline is salt model maximum extent. Inner white outline is maximum extent of caprock.

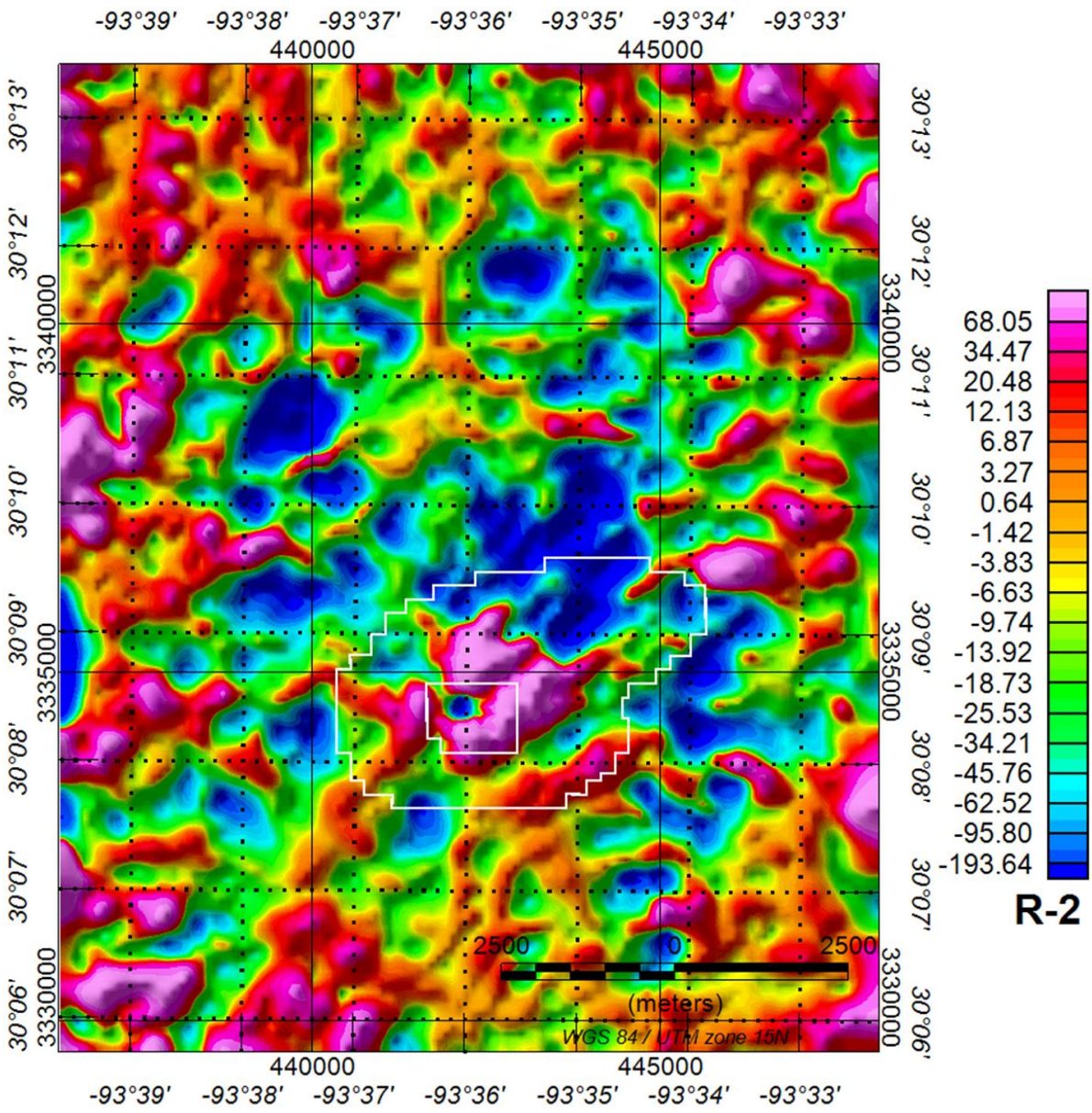

Figure 5.14 R-2 Invariant after subtraction. Outer white outline is salt model maximum extent. Inner white outline is maximum extent of caprock.

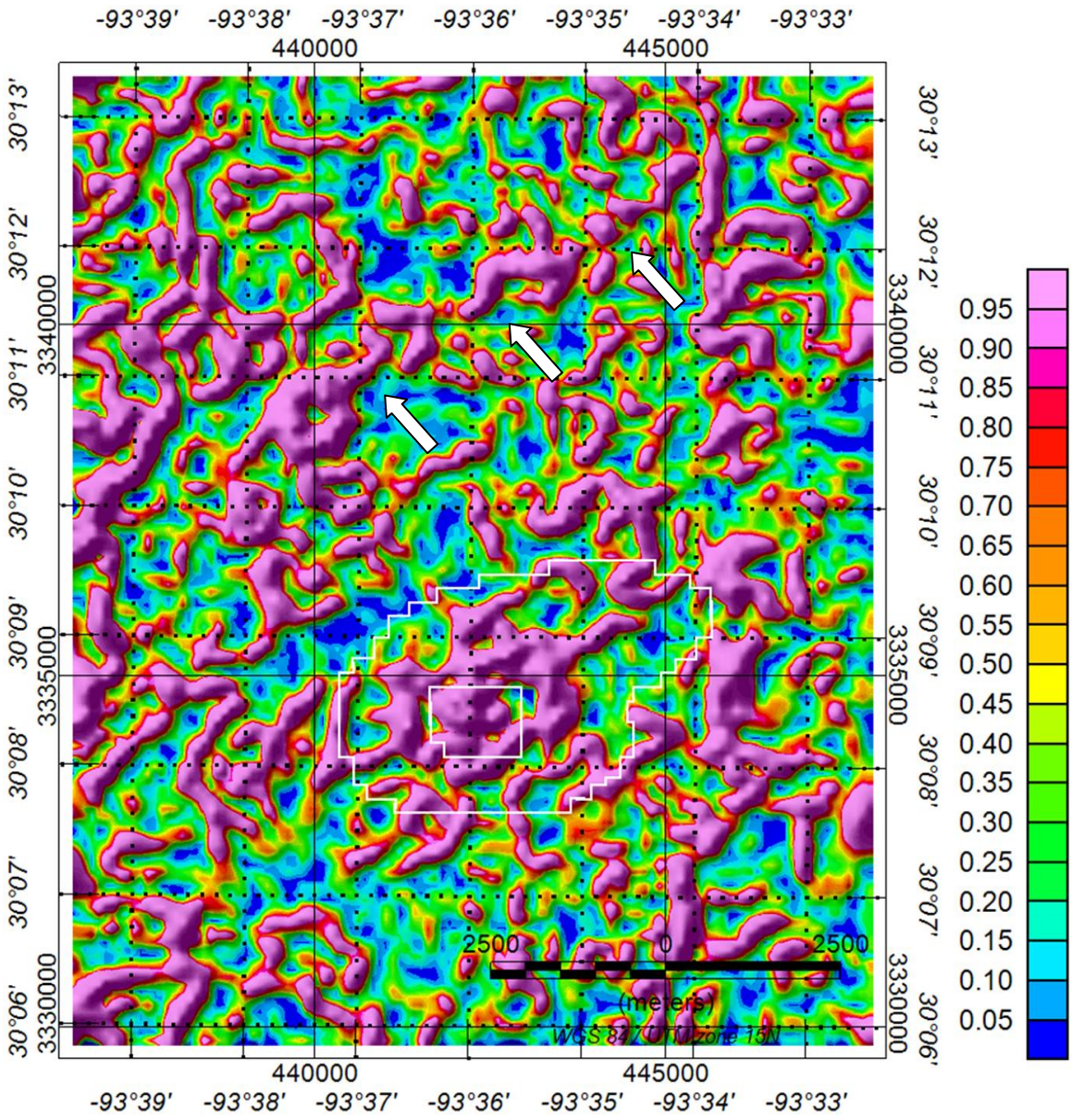

Figure 5.15 Tzz coherence after subtraction. Outer white outline is salt model maximum extent. Inner white outline is maximum extent of caprock.

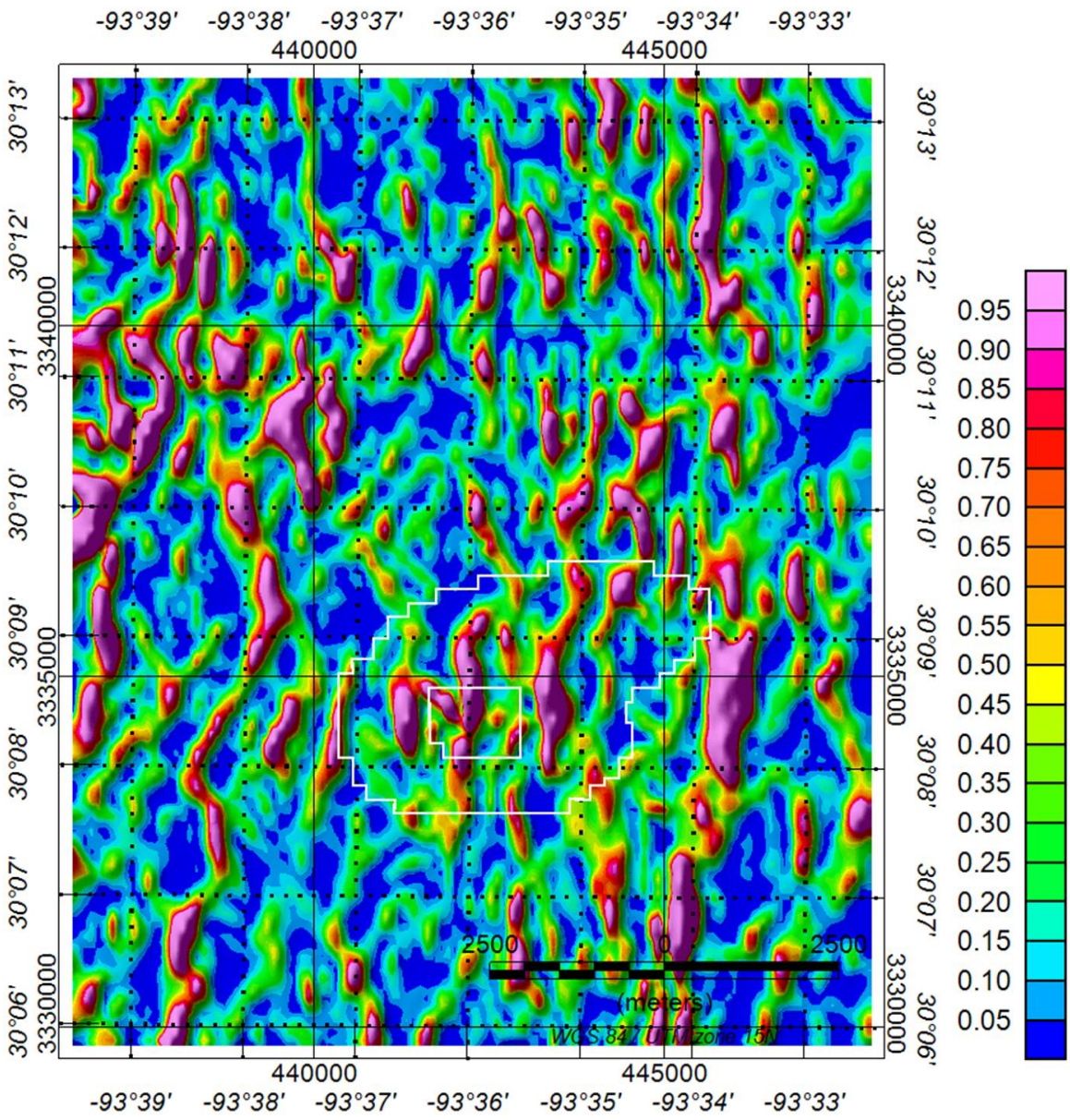

Figure 5.16 Txx coherence after subtraction. Outer white outline is salt model maximum extent. Inner white outline is maximum extent of caprock.

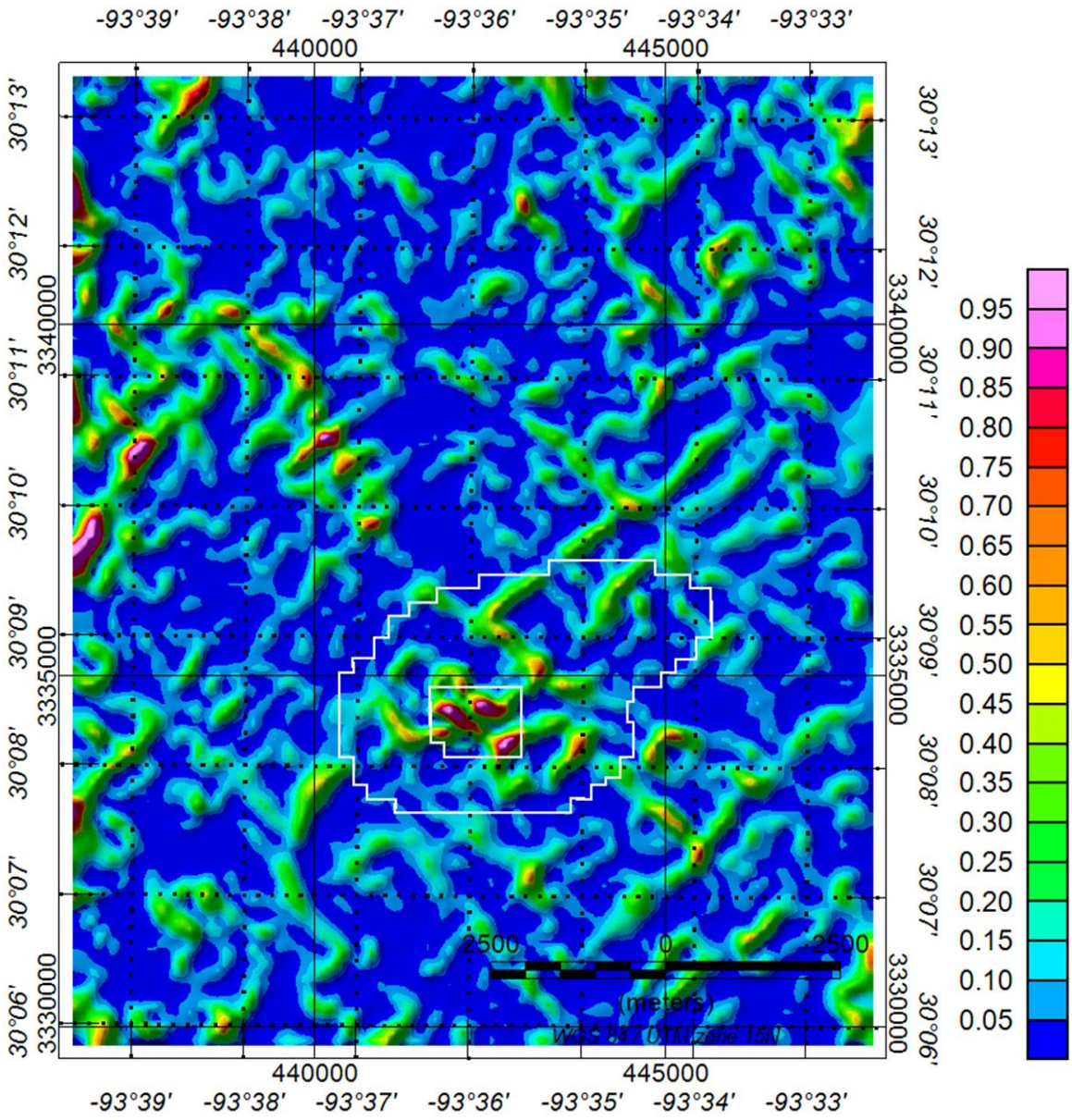

Figure 5.17 Txy coherence after subtraction. Outer white outline is salt model maximum extent. Inner white outline is maximum extent of caprock.

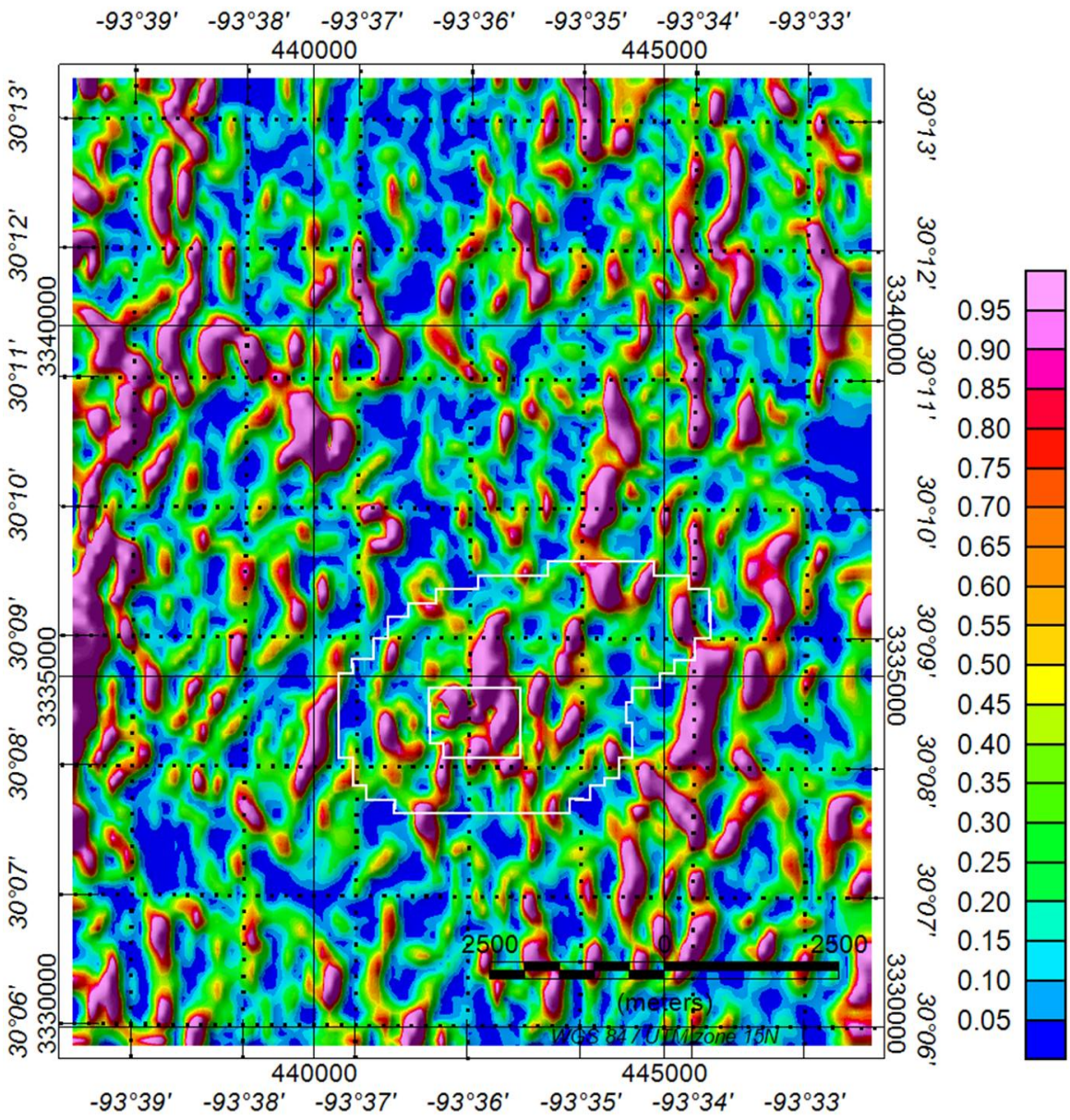

Figure 5.18 Txz coherence after subtraction. Outer white outline is salt model maximum extent. Inner white outline is maximum extent of caprock.

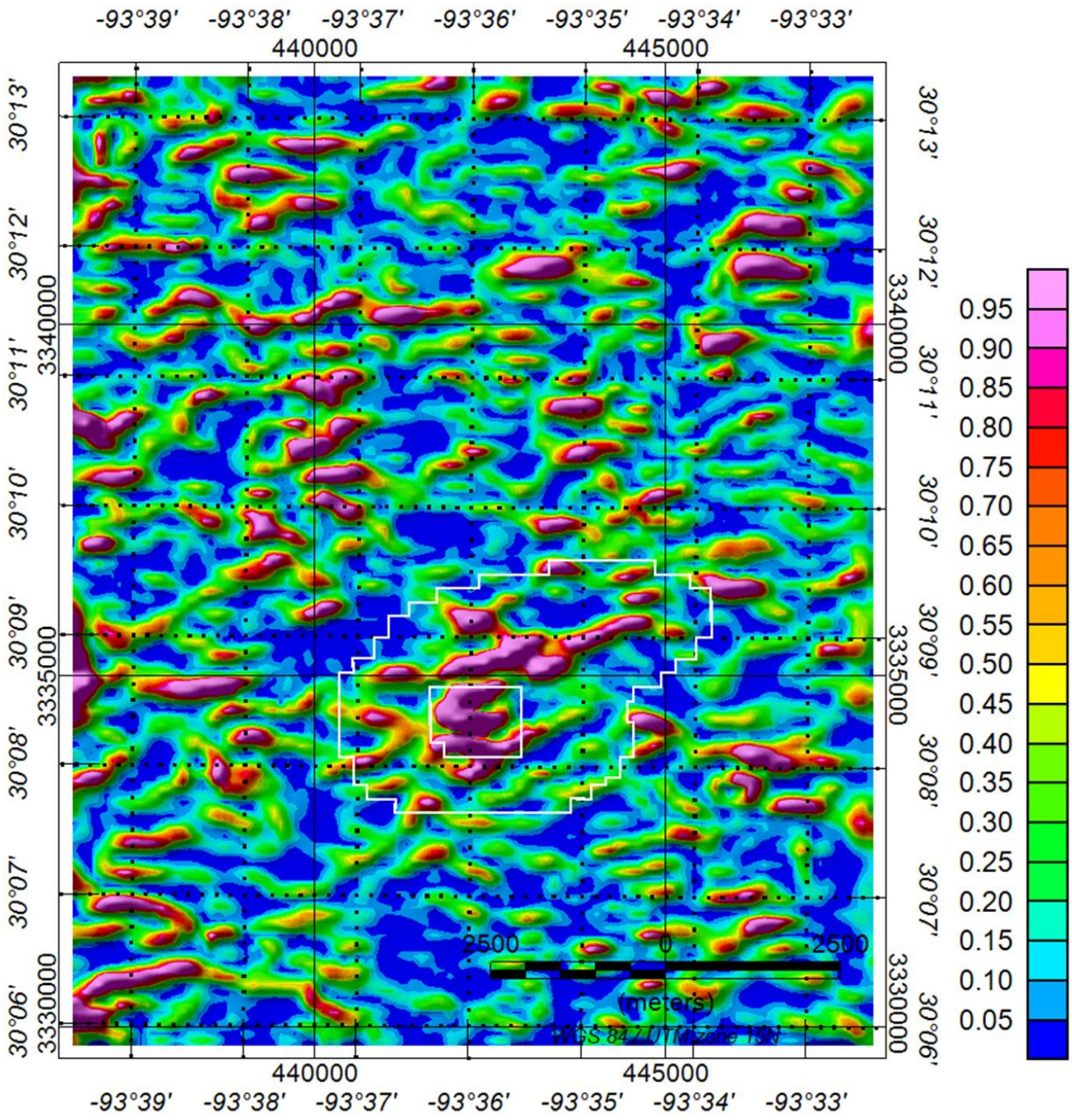

Figure 5.19 Tyy coherence after subtraction. Outer white outline is salt model maximum extent. Inner white outline is maximum extent of caprock.

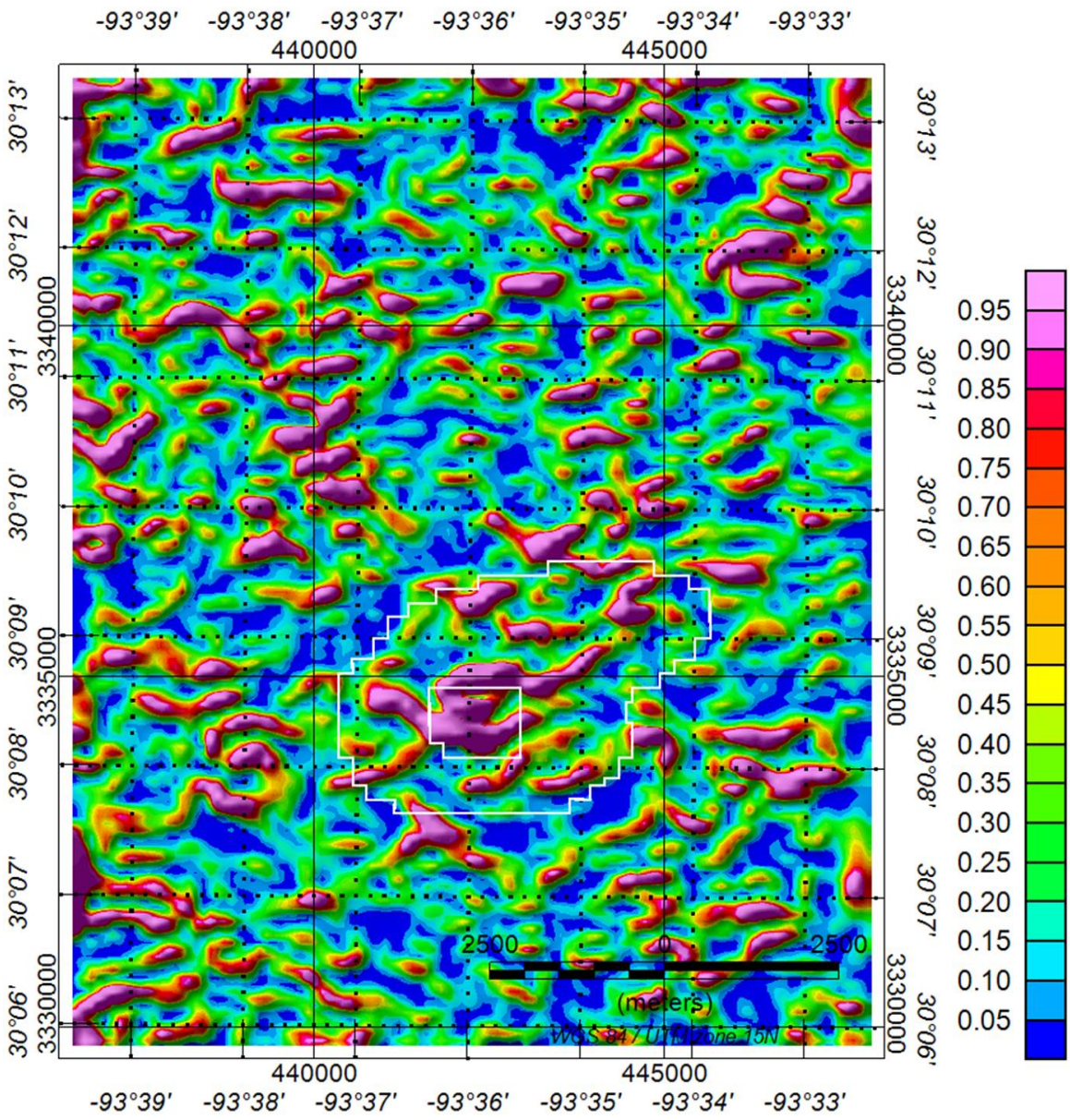

Figure 5.20 Tyz coherence after subtraction. Outer white outline is salt model maximum extent. Inner white outline is maximum extent of caprock.

5.4. Data Rotation

The data were rotated to highlight subsurface structures by aligning the coordinate system with data trends. Both Txx, and Txz gradients were rotated 45 degrees and 135 degrees. Rotating Txz or Txx by 90 degrees yielded Tyz and Tyy respectively. Rotating Txz and Txx by 180 degrees reversed the polarity of the image. Angles of 45 degrees and 135 degrees were used to determine if the middle angle between 0 and 90 degrees and between 90 and 180 degrees would emphasize trends that were weak in the default NED coordinate system.

The Txz component rotated to 45 degrees does has a noisy appearance without noticably continuous trends or high amplitudes when compared with the unrotated Txz component (Figure 5.21). The 10 km long positive amplitude trend on the east side of the unrotated Txz component (Figure 5.6) is less continuous and lower amplitude on the rotated Txz component. There is a positive trend on the southwest side of the caprock model outline and a large negative anomaly on the northeast side fo the caprock. The negative anomaly on the northeast side of the caprock is much more pronounced on the 45 degree rotated Txz component than on the unrotated Txz component. This anomaly makes it appear as if the observed Txz compnent was rotated instead of the residual image.

The Txz rotated to 135 degrees shows a number of connected linear positives to the north of the model outline (Figure 5.22). These linea features trend northeast-southwest. The east side of the rotated image has a trend of disconnected negative anomalies. The negative on the north side of the caprock model is much lower amplitude on the 135 degree rotated Txz component compared to the 45 degree rotated Txz component. The postive trend on the south

side of the 45 degree rotated Txz component is split into three trends on the 135 degree rotated Txz component and appears narrower.

The Txx component rotated 45 degrees shows a strong amplitude anomaly to the north of the dome and a lower amplitude linear feature on the southeast side of the model (Figure 5.23). The anomaly on the north side of the dome has a higher amplitude on the 45 degree rotated Txx component than on either the 135 degree rotated Txx component or the unrotated Txx component.

Trends on the Txx component rotated 135 degrees (Figure 5.24) are narrower than the 45 degree rotated Txx component but appear more continuous than the unrotated Txx component.

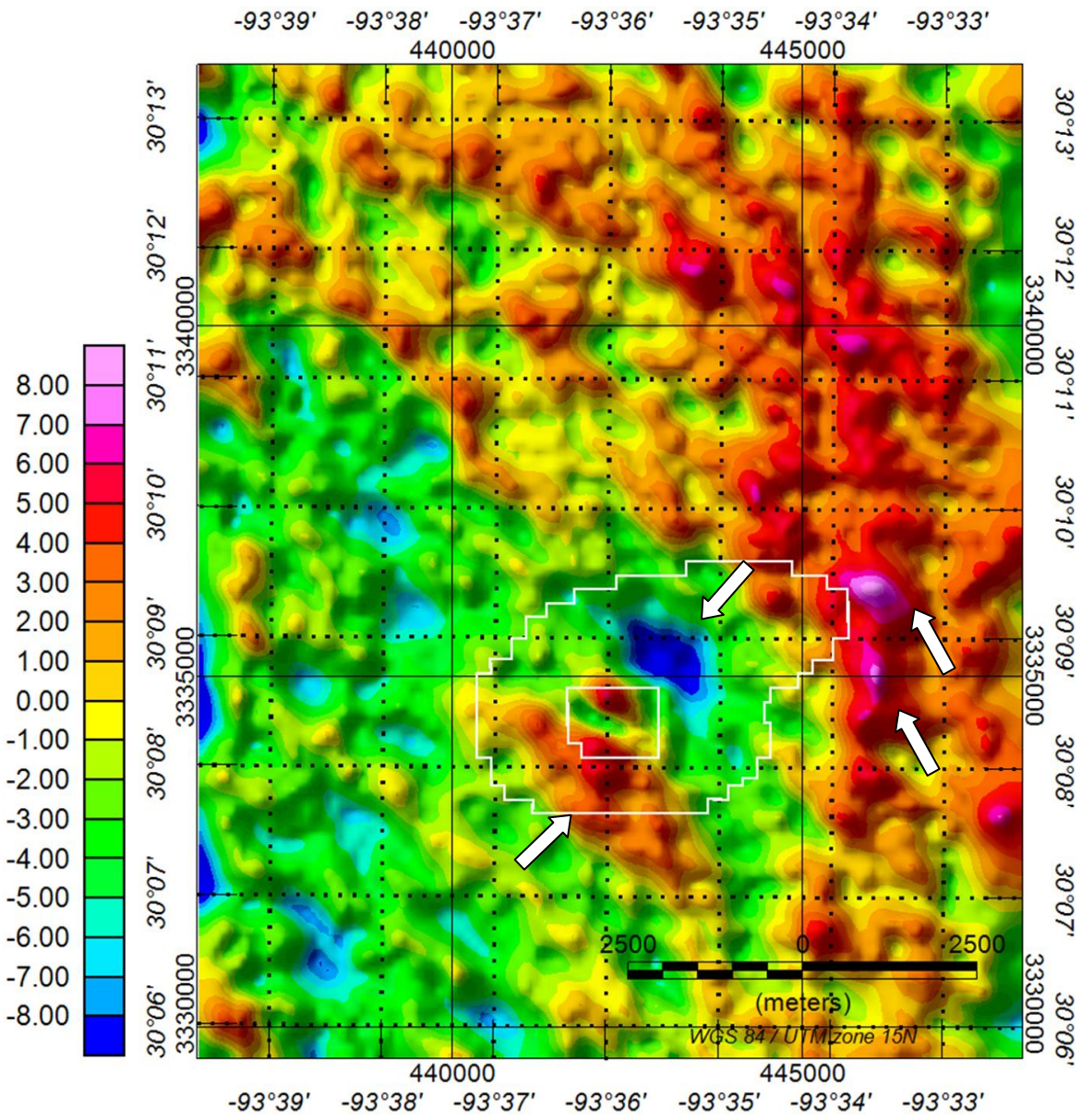

Figure 5.21 Residual Txz data rotated counterclockwise by 45 degrees. Outer white outline is salt model maximum extent. Inner white outline is maximum extent of caprock.

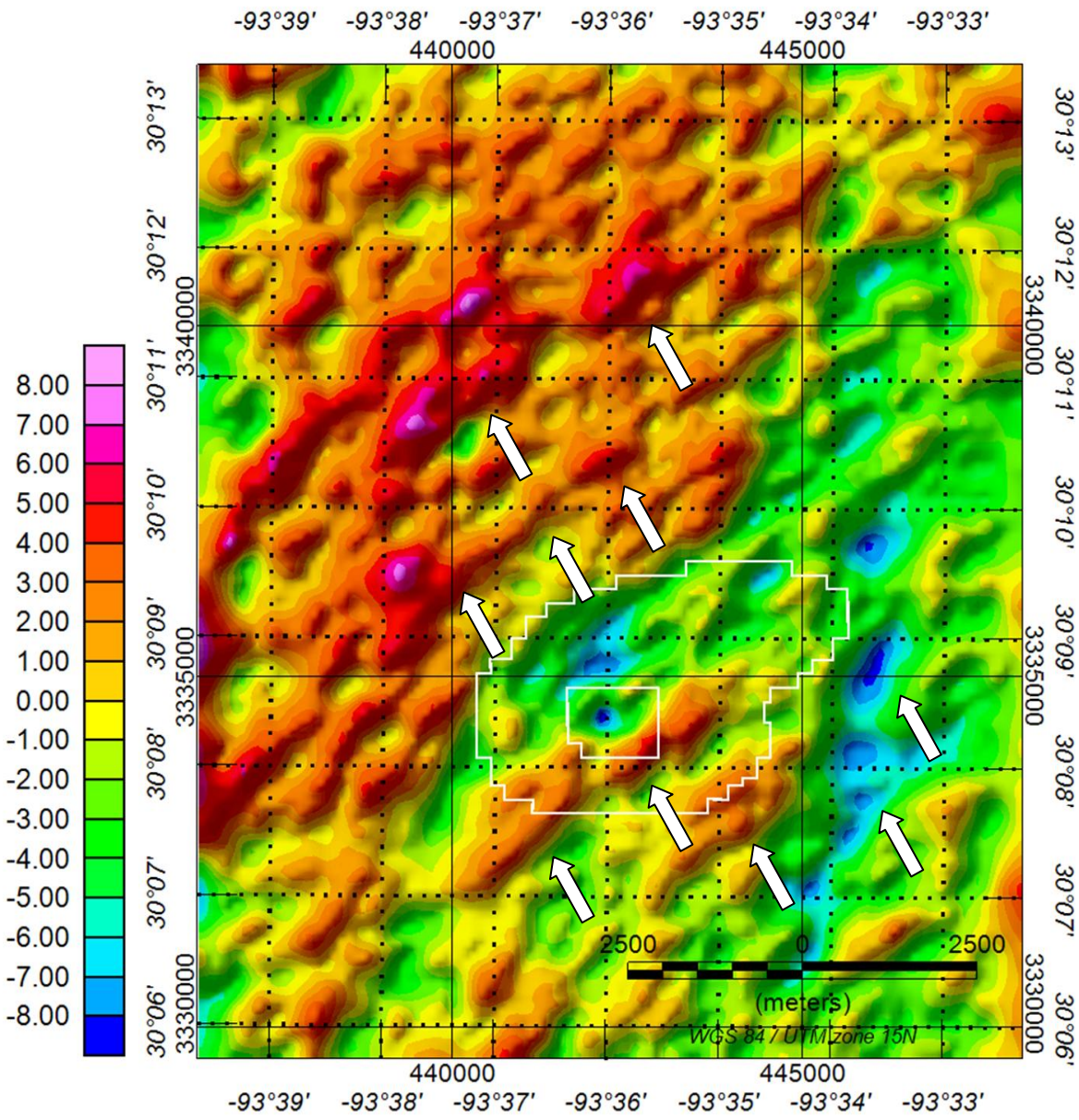

Figure 5.22 Residual Txz data rotated counterclockwise by 135 degrees. Outer white outline is salt model maximum extent. Inner white outline is maximum extent of caprock.

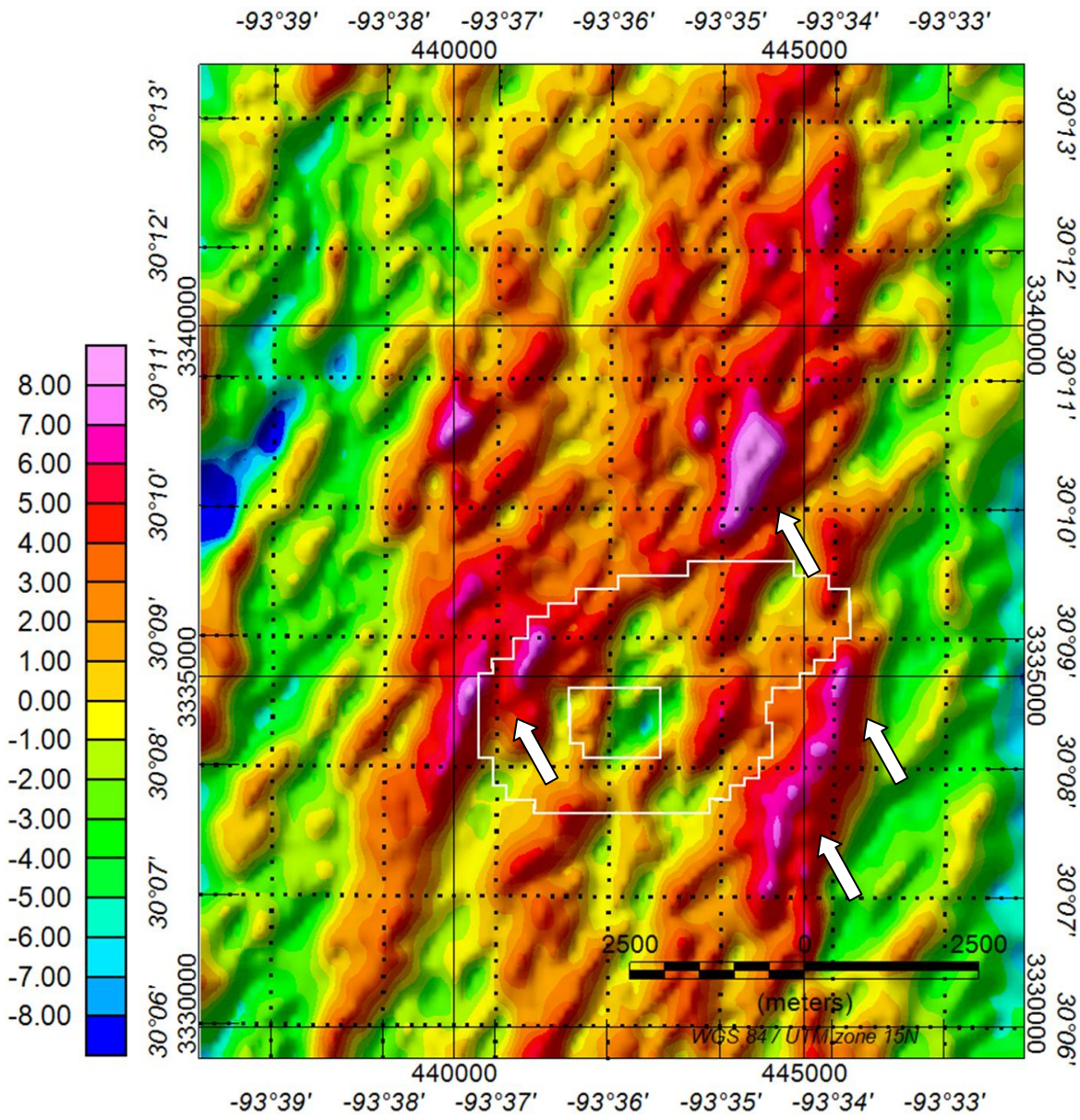

Figure 5.23 Residual Txx data rotated counterclockwise by 45 degrees. Outer white outline is salt model maximum extent. Inner white outline is maximum extent of caprock.

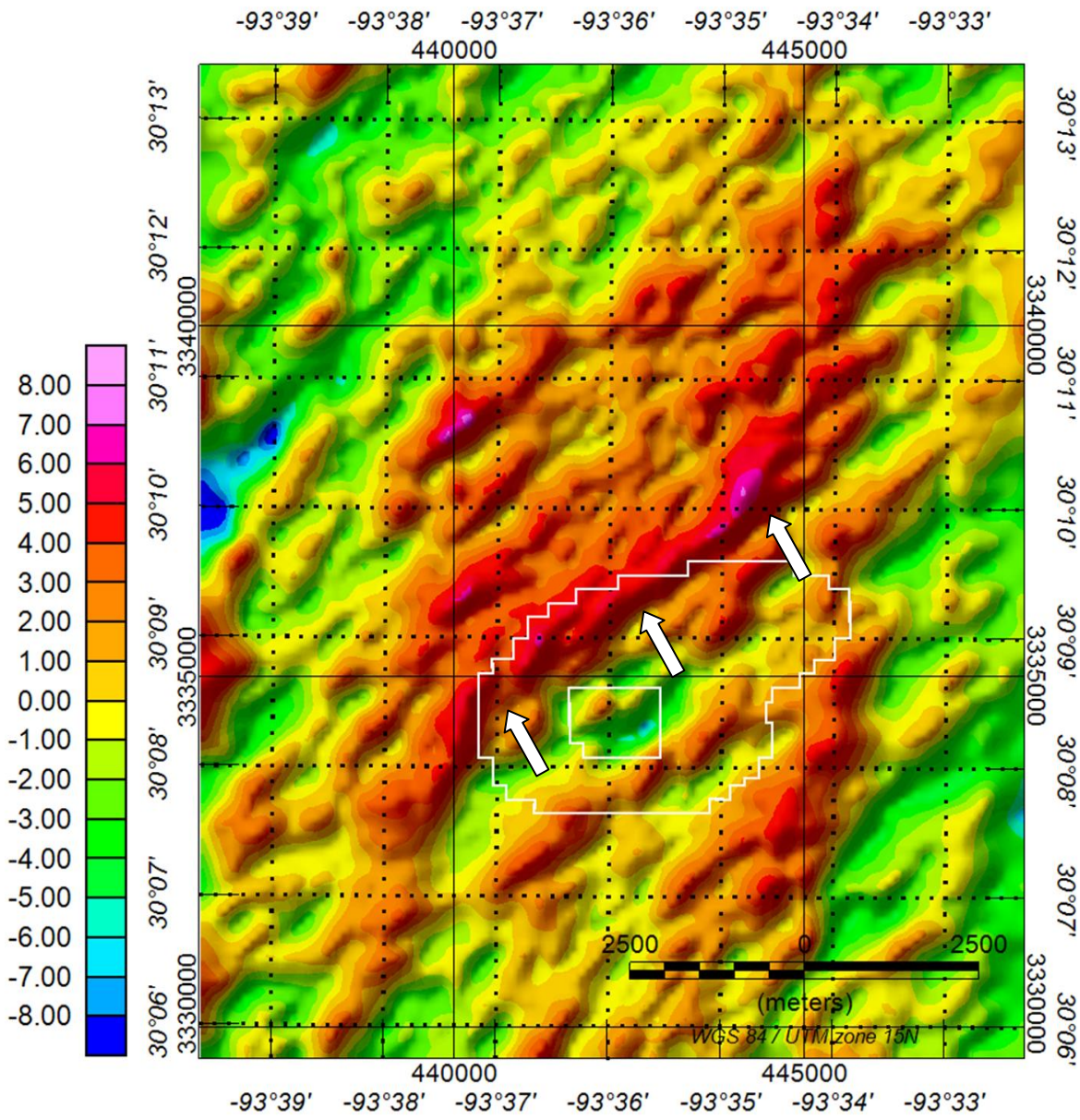

Figure 5.24 Residual Txx data rotated counterclockwise by 135 degrees. Outer white outline is salt model maximum extent. Inner white outline is maximum extent of caprock.

Chapter 6

Interpretation

Interpretation of FTG data at a reservoir scale is not currently recorded in the literature. Most interpretation work of FTG data over salt bodies focuses on constraining the base of the salt (Hokstad et al., 2011). The most significant challenge in this project is eliminating or attenuating the expected signal from the salt dome so as to increase the visibility of signals that could be caused by gas-charged reservoirs where the density contrast between gas-filled porous rock and brine-saturated rock is significant enough to be detected by FTG methods. Thus the primary goal is the detection and interpretation of these small anomalies. A secondary goal is to gain new insights on the structural framework of the Vinton dome from the FTG data. Most of the work at Vinton dome has focused on the caprock and the columnar salt below the caprock. Besides the conventional gravity work done by Eti (2004) there is not a lot of knowledge about the maximum extent of salt beneath the dome at depths greater than 2800m.

The models generated for the caprock and salt dome fit all available *a priori* information. The caprock model is constrained by well control and conventional gravity information. There is no seismic imaging over the top of the dome due to lack of coverage and the rugosity of the top of the caprock (Constance et al., 1999; Eti, 2004; Coker, 2006). Well log picks and an interpretation of seismic reflection data were used to constrain the geometry and density of the salt model between 300 m and 2800 m depth. There are no wells that penetrate more deeply than 2800 m, and the seismic data are of very poor quality below this depth. The salt model used in this study ends at 2800 m depth. Below this the only information available is the conventional gravity interpretation done by Eti (2004), but it was not used in the model

generation for two reasons. The first is that signal wavelengths are very long for subsurface features below 2800 m which makes the interpreted salt edge less precise than what is needed for calculating the FTG signal. The second is that a test was conducted using the salt geometry below 2800 m depth, and the salt signal calculated was up to -20 Eo for the layers at that depth. The measured data was upward continued to a height of 3 km to compare with the calculated signal. There was a 17 Eo difference between the calculated signal and the upward continued data. It was then decided that a model that extended below 2800 km would not be used. Due to these constraints on the salt model the results show that the FTG data captures more information than is currently available for the dome from other geophysical methods. Comparisons between the salt model and the FTG data will be made to see what insight can be gleaned from the forward calculation exercise.

There are a number of small-scale negative residual anomalies present after subtraction of the forward calculated salt signal on the Tzz gradient. Negative anomalies on the Tzz are used to guide the residual anomaly analysis since negative anomalies are predicted by reservoir forward model calculations. The Tzz gradient shows the best discrimination between signals from different subsurface structures. Residual anomalies can be the result of noise, signals from small features such as gas charge reservoirs, or remaining signal from the salt dome that is not captured in the model. The noise is characterized by short wavelength, randomly distributed anomalies. To minimize noise contamination the data were upward continued before subtraction. A few areas will be proposed that match the expected signal for a gas-charged reservoir. Negative residual anomalies can also be caused by any structures with a lower density than the surrounding sediment. The model built fits the seismic interpretation, but Eti's salt interpretation from conventional gravity contains additional salt from 2800m to 3800m depth.

To create a more accurate salt dome model above 2800m depth would require additional *a priori* information. Inversion is another alternative for deriving a more detailed salt geometry and density.

6.1. Caprock

In the model, the largest spatial extent of the caprock is 1300 m east-west and 1000 m north-south at 360 m depth. The top of the caprock in the model forms a peak that is 200m x 200m at 130m depth. The signal calculated from the model exhibits asymmetry similar to the caprock's geometry. The signal peak is on the south side of the caprock area, and the top of the caprock has a shallow dip to the north. The residual positive Tzz anomalies on the west, south, and north sides of the dome may be due to overhangs of the caprock that are not included in the current model. Two reasons for not including these overhangs are that 1) they are less than 100 m from the model caprock and 2) the well information for the caprock is not available or missing (Figure 6.1). If overhangs are less than 100 m from the model caprock the only way to model that signal would be to increase the resolution fo the caprock model to less than 100 m. The positive signature of the measured field data extends outside of the maximum caprock extent modelled in all directions. These positive anomalies around the caprock suggest the FTG data has recorded the caprock signal in places where well log information is absent (Figure 6.2). The FTG data provides a more spatially continuous record of signal than previously available. The residual map shows a similar extension of the caprock as well as areas within the modeled caprock where a small amount of residual signal was not captured by the modeled signal. The positive residual anomalies on the north side suggest a shallower caprock than modeled.

The south residual positive anomalies could indicate one of three possibilities. The first is a shallower caprock than indicated by well log picks. Second is a deeper caprock/salt interface than modeled. All base of caprock picks are between 300 and 400 m depth, but all the caprock bottom picks are on the south side of the dome. Both of these possibilities would lead to a thicker caprock. Another possibility is that the salt beneath the caprock extends further south than 200 m from the edge of the caprock (Judston and Stamey, 1933). The wells drilled are as close to the edge of the overhang as possible. Wells north of the overhang do not contain picks at the interface between caprock and salt.

Several more models were tested with extensions in either direction. Residual caprock signal could be reduced by adding an additional row of on any side of the caprock model. The model was modified until most of the residual signal was taken out, but the subsequent model had a 200 m x 1000 m area of caprock disconnected from the originally modelled caprock. This area of caprock was not consistent with well logs on the north side of the dome where caprock was not observed. The model was reverted back to the original model defined by *a prior* information.

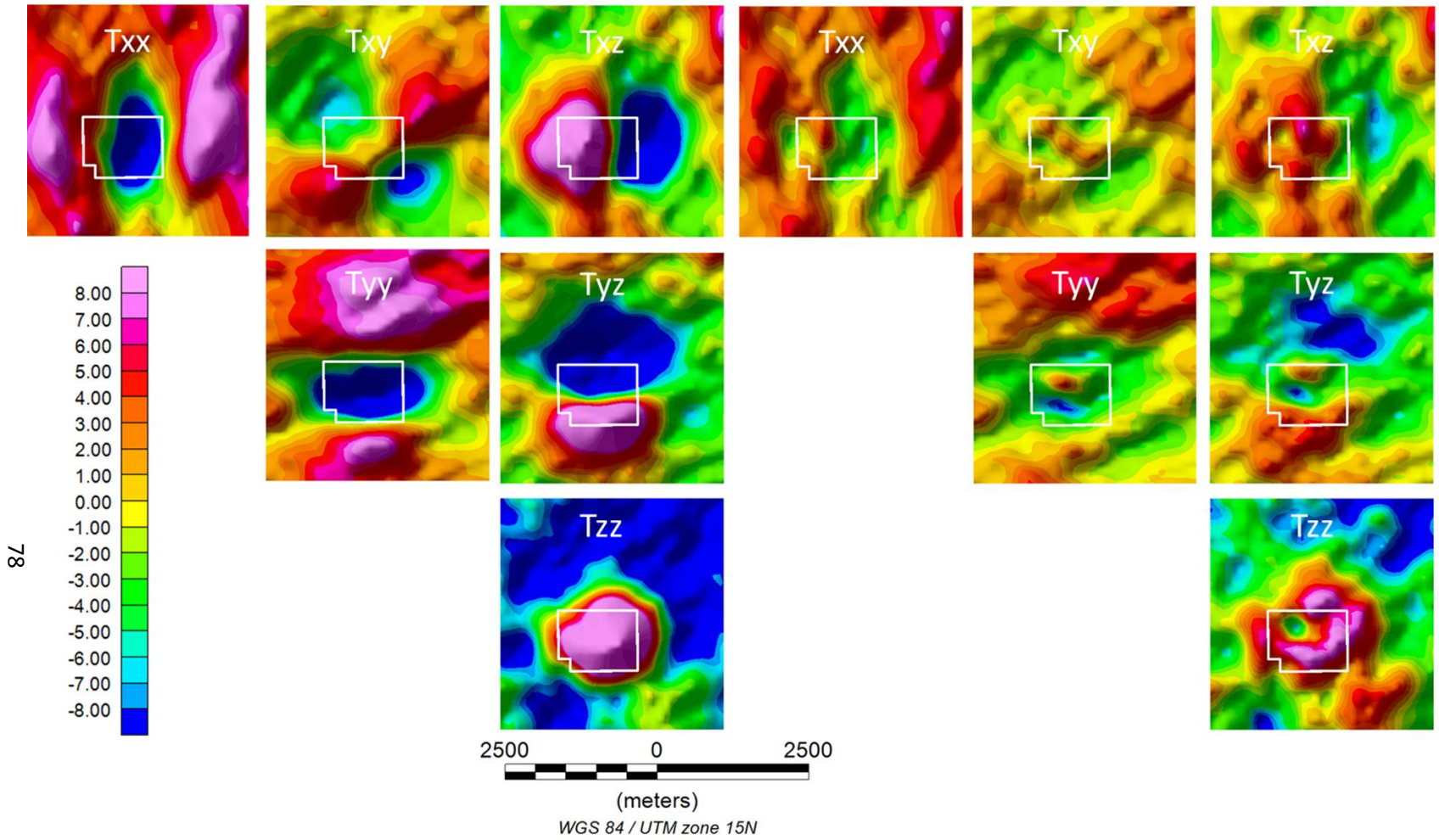

Figure 6.1 Observed gradients (left) and residual gradients (right) with maximum extent of caprock model outlined in white.

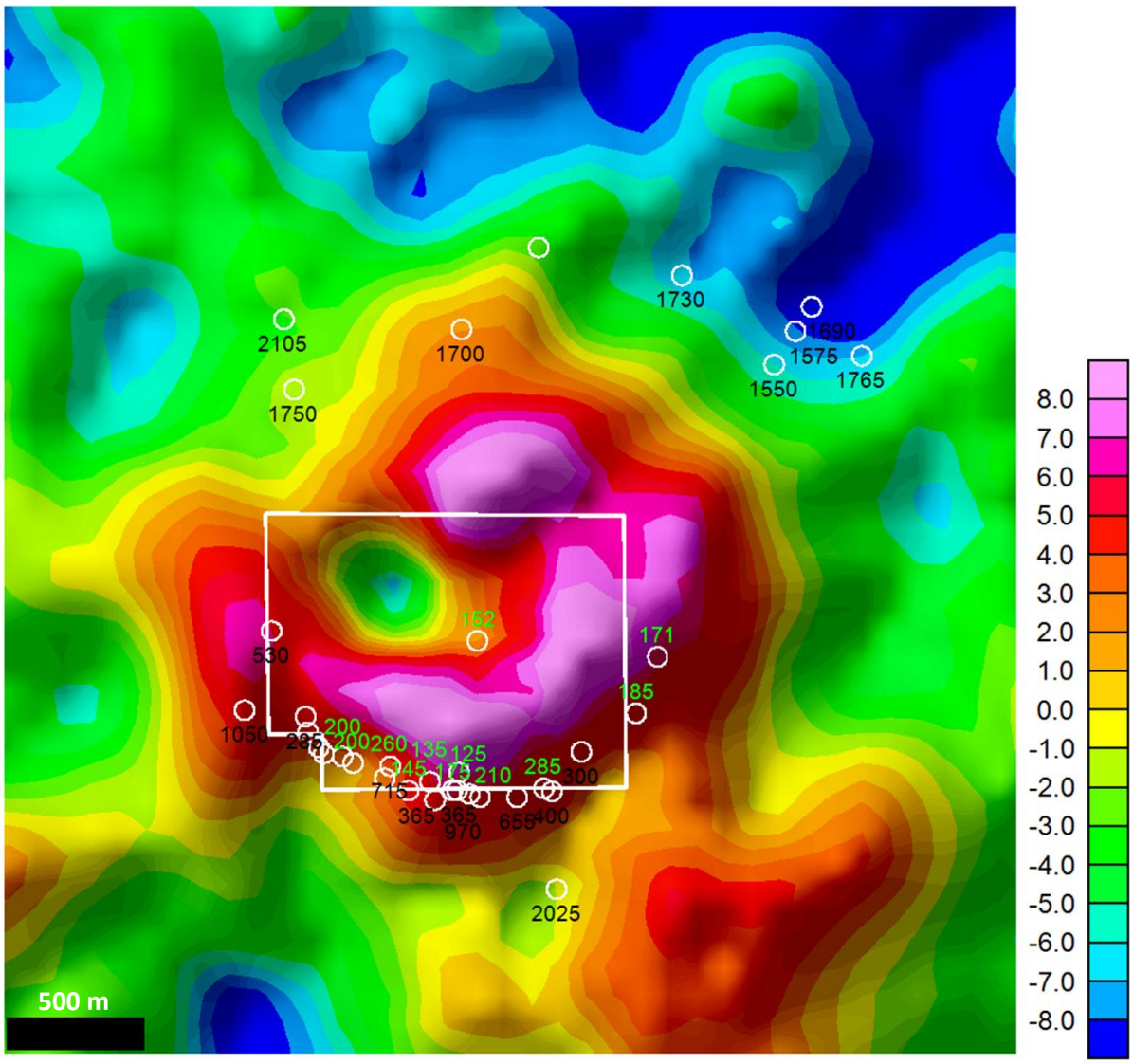

Figure 6.2 Caprock signal for the Tzz gradient with well log picks for top caprock (green) and top of salt (black) (Eti, 2004).

6.2. Salt Dome

The model signal shows the asymmetry of the salt dome as well as the caprock. The signal calculated for the gross dimensions of the salt dome above 2800 m fits the measured signal. The Tzz gradient shows a spatially extensive residual anomaly close to -5 Eötvös (Figure

6.2). The presence of an extensive negative residual anomaly indicates salt below 2800m or shallow salt not included in the model. The residual anomaly is consistent with a 3km upward continuation that shows an anomaly of similar dimension and magnitude. This indicates a good match between the calculated signal for the salt and the measured signal over the dome. The threshold of success for gravity modeling is around 5 Eötvös (Coburn, 2002). The residual anomaly is stronger on the north side than the south. When the top of salt contours from Eti (2004) are overlaid on the 2km upward continued surface and the residual surface, it can be seen that there is a higher residual anomaly on the north side of the dome than on the south side of the dome. Since the top of salt has the same depth on the north and south sides of the dome but different signal magnitudes, it indicates that the salt is thicker on the north side of the dome than the south side. One reason for this thickness may be a buildup of salt on the north side of the salt dome. The fault forms the only available accomodation space for salt migration.

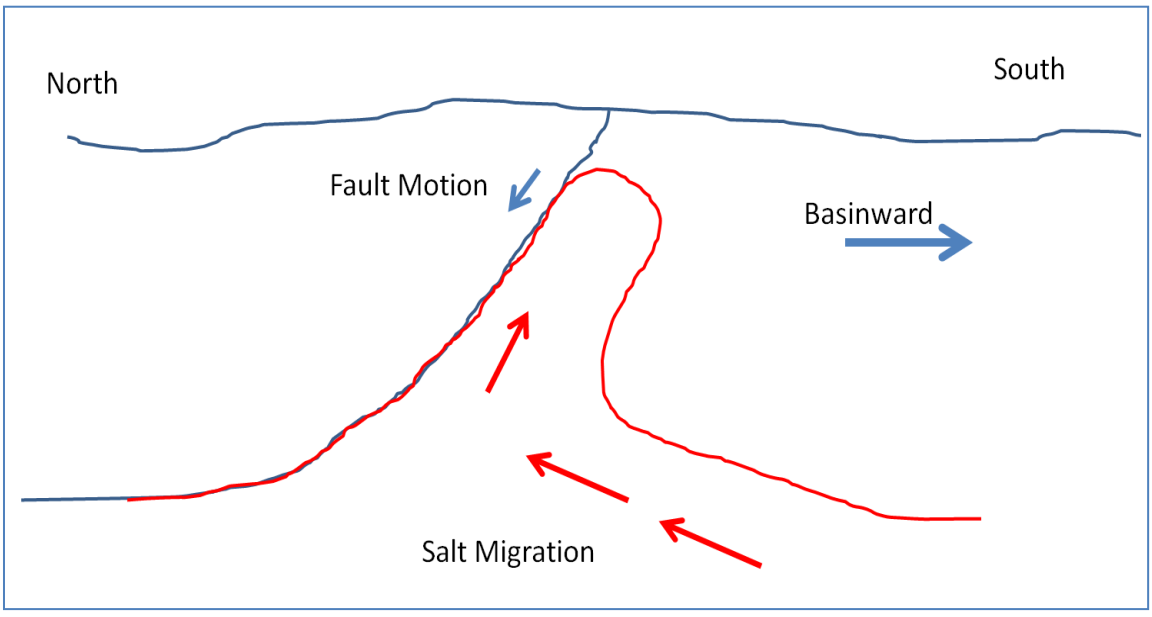

Figure 6.3 Possible salt migration up counter-regional fault as region moves basinward.

The data show three boundary geometries for the salt dome. Between 900 m and 2800 m the well logs and seismic data define a broad ridge of salt extending to the northeast. Below 2800 m the boundary of the salt defines an ellipse with a long axis that measures 10 km north-south and 6 km east-west. At 3800 m depth the outer boundary of the salt has a teardrop shape with the rounded end toward the north and the trail pointed south. The shallow portion of the salt dome between 1000 m and 2800 m is roughly parallel with the direction of the counter-regional fault. The teardrop shape maximum salt boundary is likely the geometry of the salt as it migrated from the Louann salt. The maximum extent of the salt body as mapped by Eti (2004) is widest on the north side of the dome and narrows to the south (Figure 6.4). This suggests a broad salt body moving from south to north. Sediment loading in the Miocene may have terminated northward salt movement. Rowan et al. (1999) defines a salt dome system with adjacent counter-regional faults as a stepped counter-regional salt system (Figure 6.4). In this system, differential loading of sediment initiates the counter-regional fault. The block diagram in Figure 6.4 and the Vinton dome differ in the spatial relationship between the dome and faulting away from the dome. The Rowan et al.'s model shows deformation by faulting along the salt migration pathway. In the case of the Vinton dome en echelon faulting similar to Keystone faults that occur south of the dome in the stepped counter-regional model. Thus the Vinton salt probably migrated from the south during initial emplacement in the Eocene as interpreted by Eti (2004). After the Eocene sediment loading caused the salt to migrate south along the young counter-regional fault.

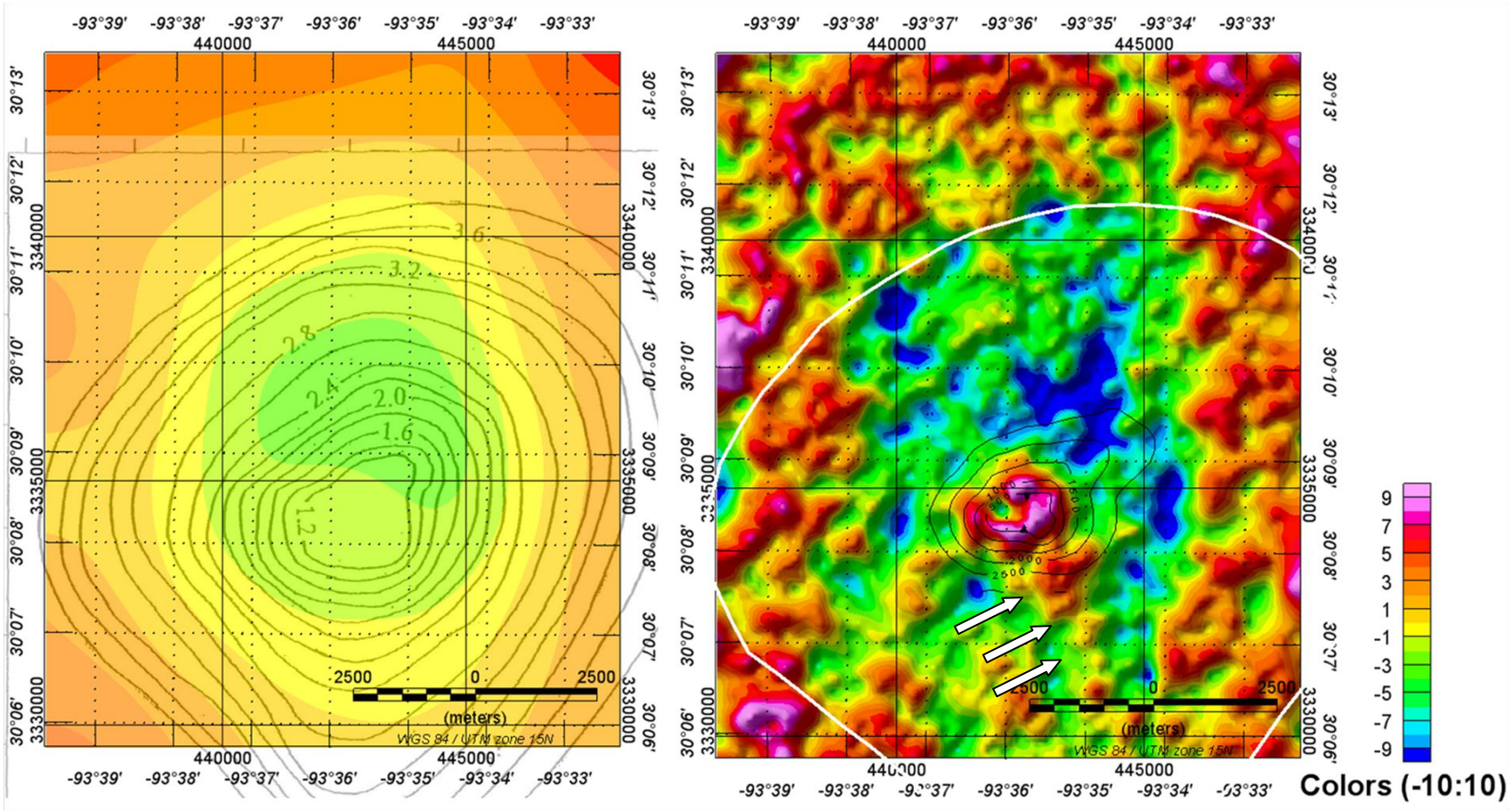

Figure 6.4 (Left) Residual map upward continued to two km. Eti's (2004) top salt surface contours overlaid in black. (Right) Tzz residual map with 3.8 km contour from Eti's (2004) top salt interpretation outlined in white. Arrows on the right residual anomaly map define a positive trend extending south from the caprock.

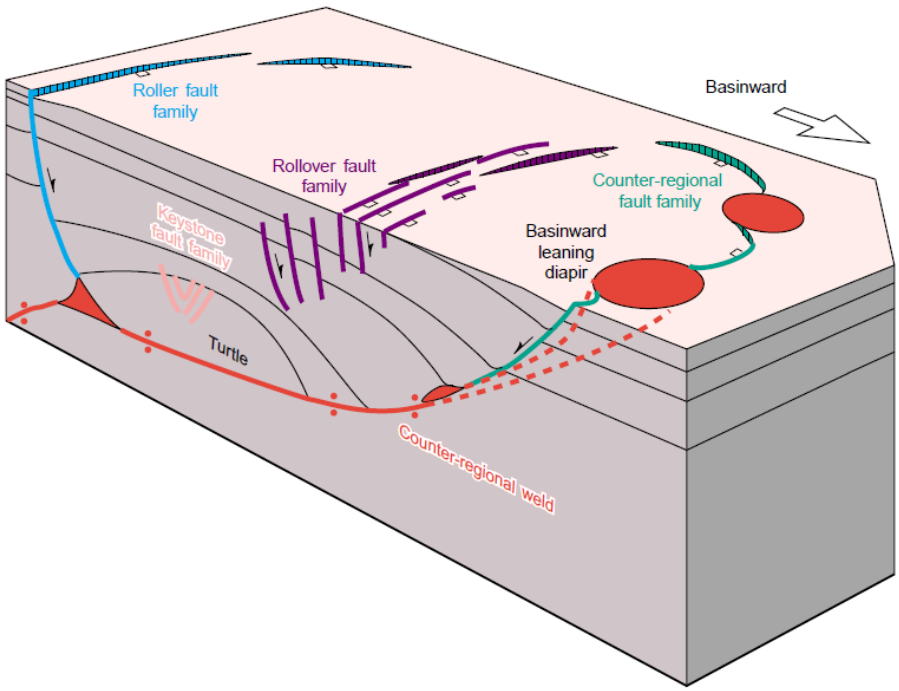

Figure 6.5 Fault types found near salt in a stepped counter-regional salt system (Rowan et al., 1999).

6.3. Faults

The biggest surprise from the FTG data is the lack of clear signal coming from the counter-regional fault centered over the top of the dome. With a throw of 460 meters and a length on the scale of kilometers, it should have appeared on the FTG data. Possible explanations of why the fault does not have a significant expression in the FTG data include the influence on the fault signal by the salt dome, or the lack of a significant density contrast across the fault interface.

There are positive anomalies on the south side of the dome of the Tzz gradient (Figure 6.2). The positive trend can be caused by higher density fault blocks adjacent to lower density fault blocks. This trend is probably caused by a configuration where younger, less dense sediments are downthrown against older, denser sediments. The en echelon faults on the south

side of the dome are similar to keystone faults defined by Rowan et al. (1999) where faulting takes place in response to salt evacuation.

The H-2 invariant has been used to interpret radial structures around an igneous body (Mataragio and Kieley, 2009). I have applied the same methodology to the Vinton dome (Figure 6.4). The H-2 invariant interpretation relies on picking breaks in signal instead of picking along peaks or troughs. I tried to stay consistent to trends radiating from the peak of the dome. There are a number of trends that are tangential to the dome, and could indicate undulations or geometry changes of the dome instead of faulting. There are a number of linear trends around the dome that suggest faulting is more extensive than previously thought, however these features can also be caused by cultural effects such as roads and pipelines. This may be due to faults that are shallower than can be confidently interpreted by seismic. Near the surface seismic can be skewed by terrain effects, refracted wave arrivals, or problems with the survey geometry. The invariant does not relate fault throw. Equation 4.5 shows that both Txz and Tyz terms are squared and any positive/negative relationships eliminated. It is unclear which side of the lineation should be designated as the downthrown side without inspecting another gradient.

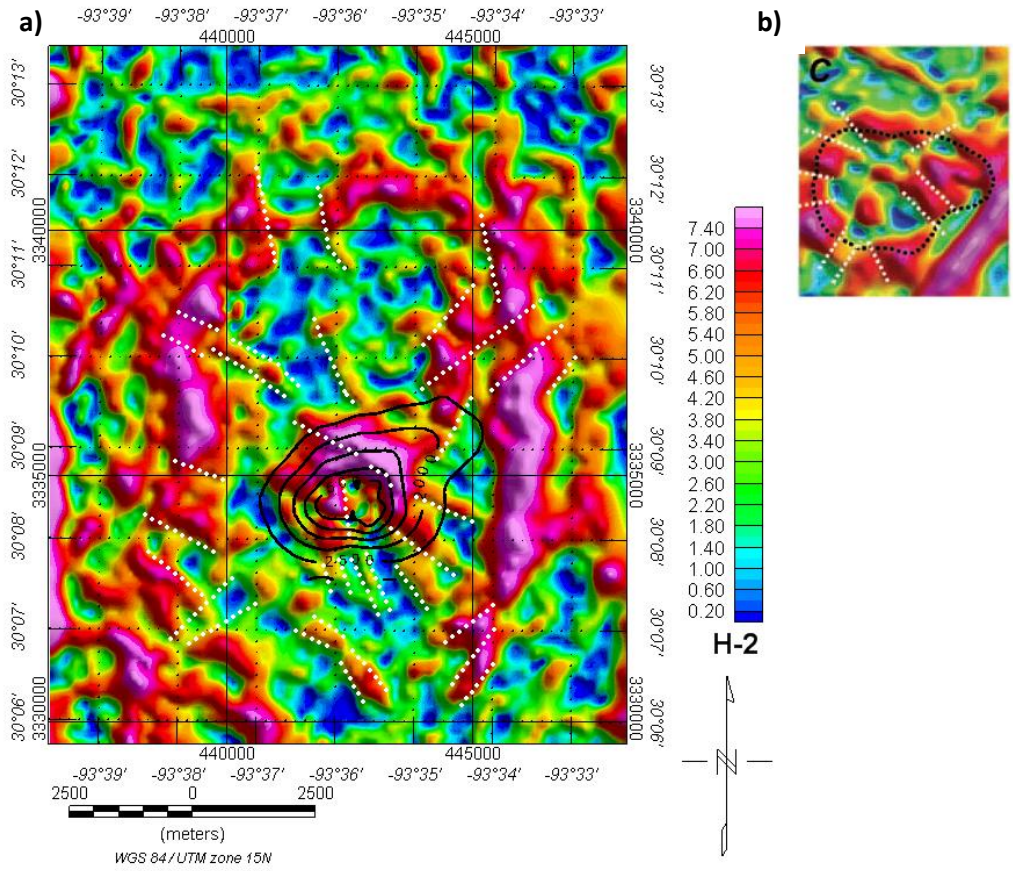

Figure 6.6 a) H-2 Invariant with radial fractures interpreted and (b) an example interpretation from Matargio and Kieley (2009).

6.4. Reservoirs

The expected signal from a gas-charged reservoir is a negative anomaly on the Tzz gradient. The amplitude of the anomaly decreases quickly as the depth of source block increases. The models indicate that most reservoirs imaged by FTG methods will be greater than 500m x 500m and between 500m and 1km depth (Figure 6.7). All of this is assuming a reservoir thickness of 100m. One hundred meters is a thick reservoir to be saturated with gas. This thickness indicated by the model is probably more indicative of a number of thinner reservoirs

in close depth extent. Duncan (2005) points toward this when he talks about sand stringers within the Miocene. Most of the perforation intervals recorded in SONRIS are less than 20 m thick.

Sixteen areas were picked that exhibit the expected reservoir signal (Figure 6.8 and 6.9). These areas have a consistent expression across all six gradients. All but two of the areas are outside the area where production is currently taking place. The two anomalies that are within producing areas have wells that are on the edge of the residual anomaly. There is a high concentration of gas production adjacent to the north side of the dome. After subtraction of the calculated signature for the entire dome model this area appeared as a positive anomaly. As discussed earlier this positive anomaly indicates a caprock overhang that is not included in the model.

When compared with dry holes, five prospective areas have been drilled including the two areas that are producing (Figure 6.10). Dry holes drilled in these five areas reach measured depths greater than 1300m. At this depth any gas reservoirs present will have very low magnitude signal as indicated by Figure 6.7. It's unclear from the SONRIS database why these wells were categorized as dry holes.

Production information from drillinginfo.com was overlaid on the residual Tzz image (Figure 6.11). This database contained production wells in five of sixteen prospective areas. However, there are four additional production on the east side of the survey that do not have corresponding negative anomalies.

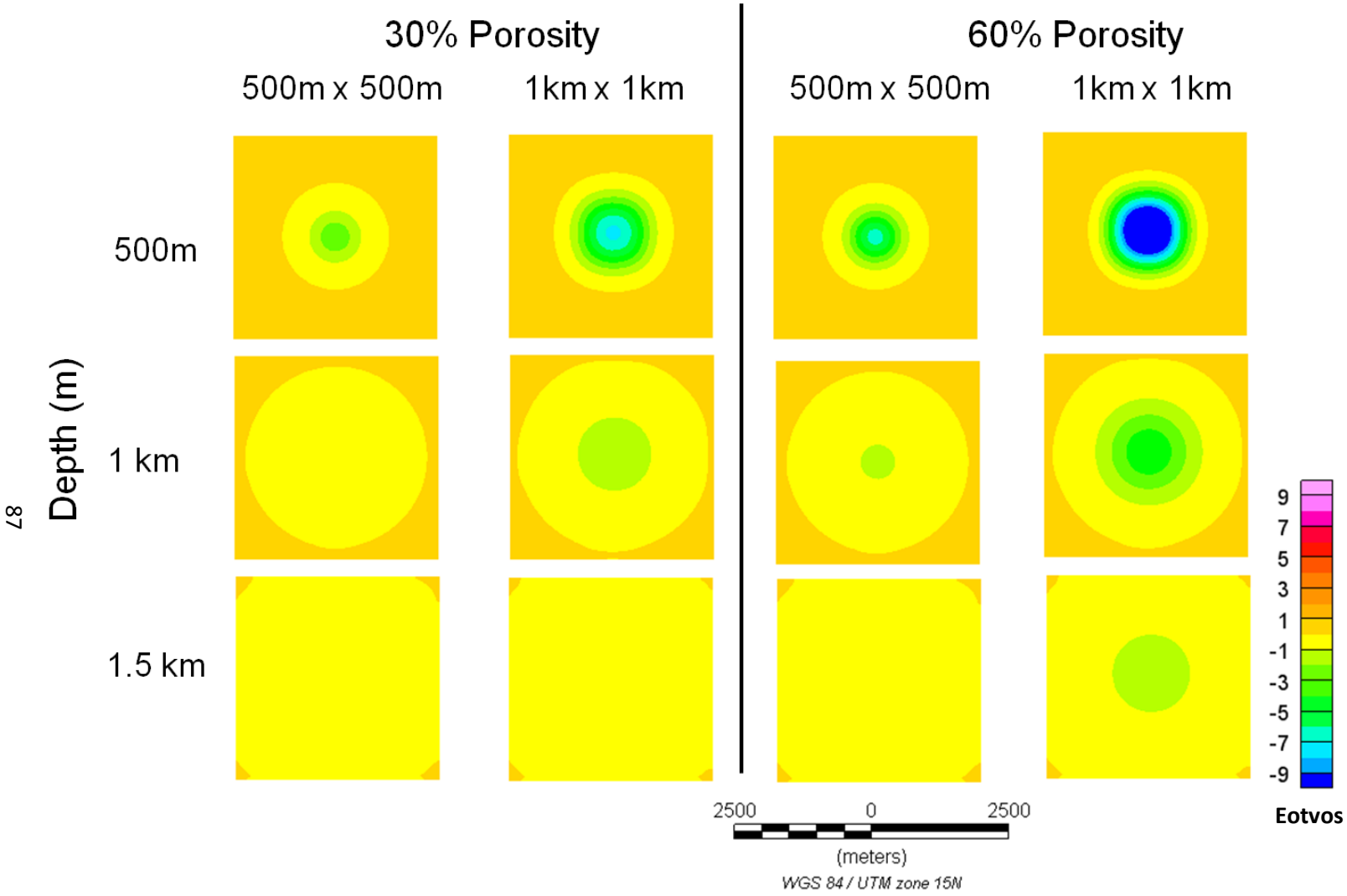

Figure 6.7 Reservoir tests for the Tzz gradient. Two block sizes were used with a constant thickness of 100m at three different depths.

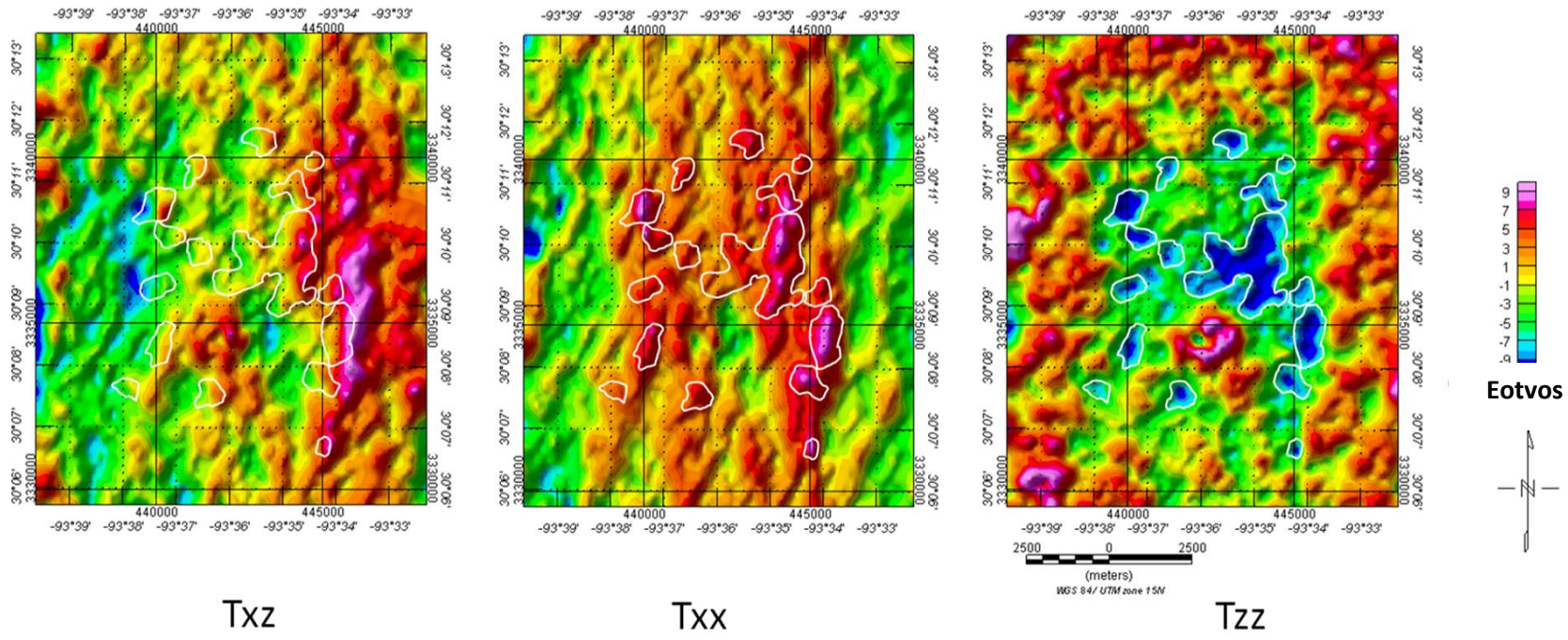

Figure 6.8 Residual maps for Txz, Txx, and Tzz. Anomalies outlined in white exhibit expected reservoir signal.

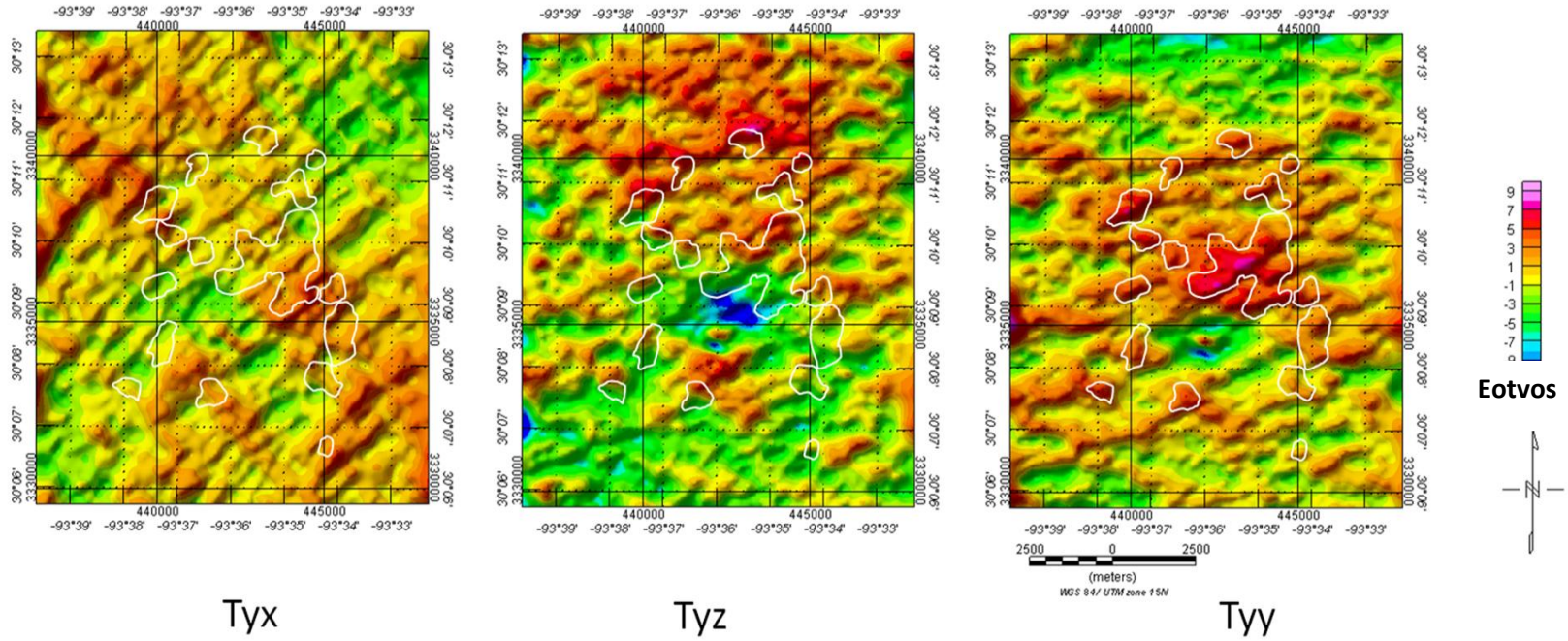

Figure 6.9 Residual maps for Tyx, Tyz, and Tyy. Anomalies outlined in white exhibit expected reservoir signal.

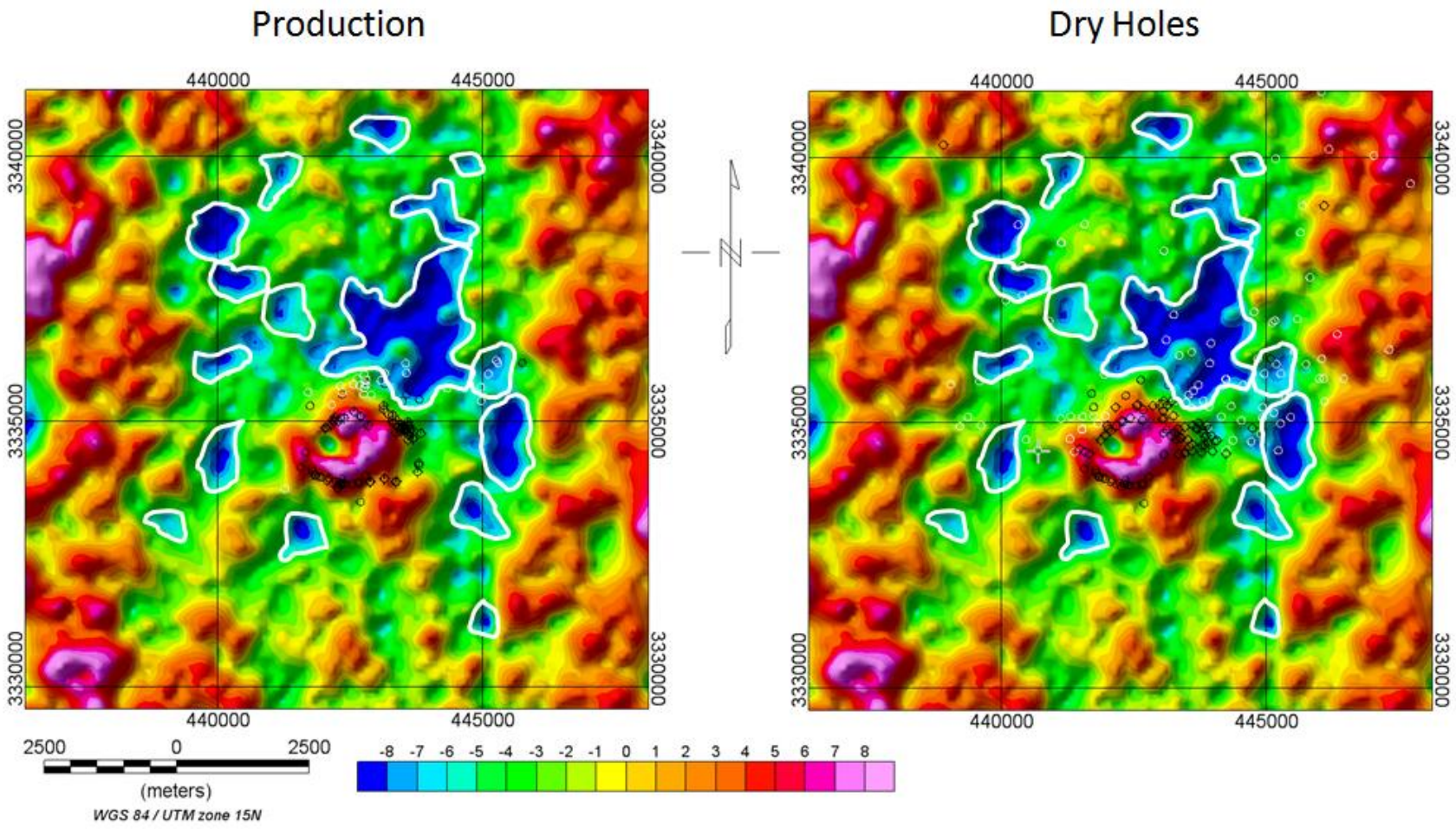

Figure 6.10 Comparison of production wells and dry holes drilled. Black circles are shallower than 1300m and white circles are deeper than 1300m depth. Prospective areas outlined in white.

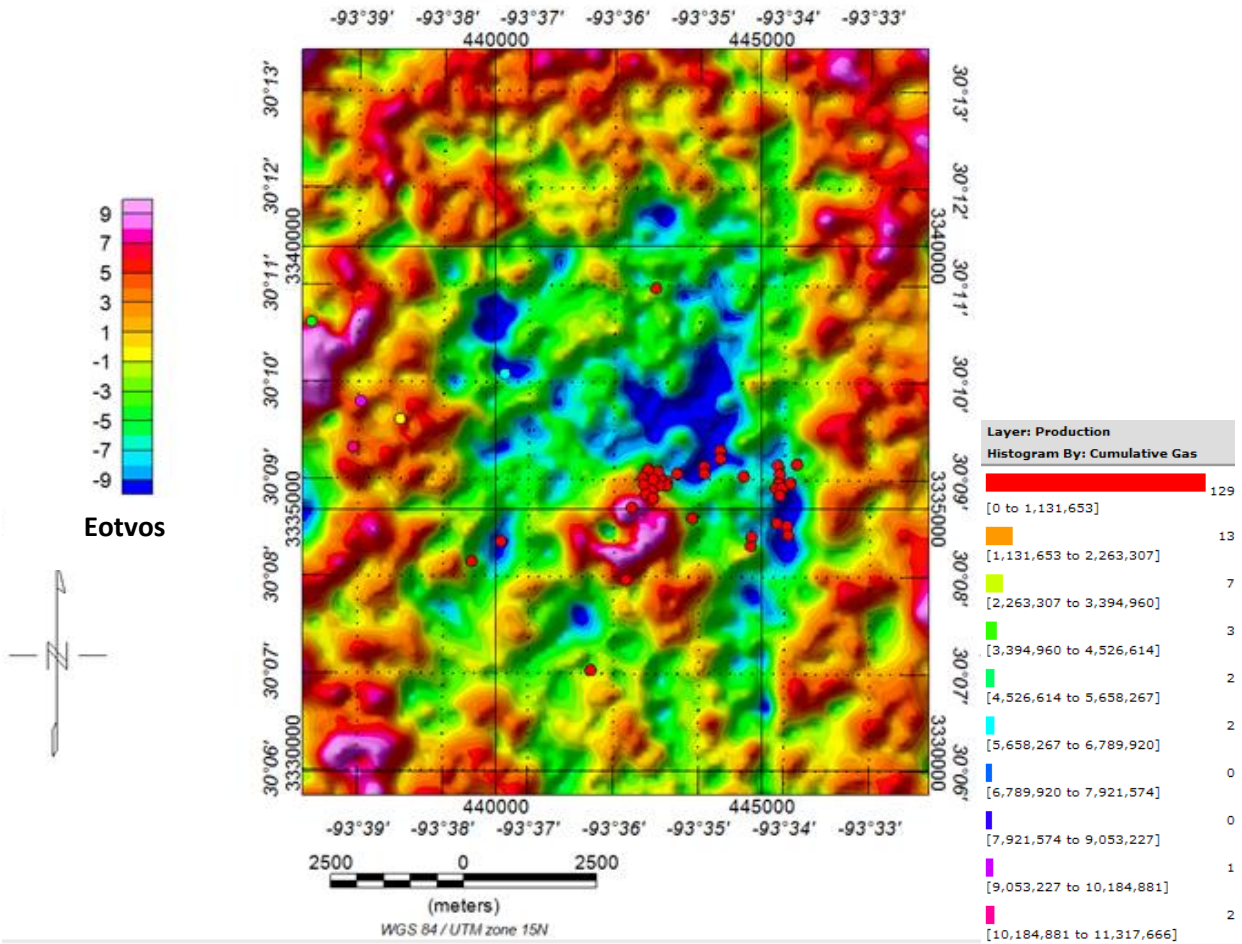

6.11 Residual Tzz plots with production wells from drillinginfo.com with colors corresponding to the amount of gas production at the well.

Chapter 7

Discussion

The results from the forward modeling exercise show differences from previous work done on the Vinton salt dome (Kisin, 2003; Eti, 2004; Duncan, 2005; Gherasim, 2005; Coker, 2006). The FTG data provides insights into the structure of the area that have not been observed through other geophysical methods. Much of the well data do not extend below 2000m. The seismic data have no coverage over the caprock of the dome and loses the salt image below 3500m depth. The conventional gravity reveals deep structure, but the FTG data show a narrower dome that is extended along the north-south axis.

7.1. Near Surface

Thompson and Echelberger (1928) divide the near surface into two units. The Pleistocene age Beaumont clay composes the surface down to 60 meters. Below 60 meters to 300 meters is the Lafayette gravel of late Pliocene age. In calculating the terrain correction for the FTG data a 1.8 g/cc near surface density was assumed. This terrain correction induced topographic features on the FTG data, and even after switching the Shuttle Topography Mission elevation data derived terrain correction for a LIDAR elevation dataset derived terrain correction there were still features that mimicked the topography of the area. Testing 1.00 g/cc to 1.8 g/cc showed that a density of 1.4 g/cc was the most realistic density for correcting the FTG data without topographic expression in the data. A VSP tomography study adjacent to the dome showed a near surface velocity of 1830 m/s (Kisin, 2003). Gardner's equation can be used to convert the velocity into density:

$$\rho = 0.23V^{0.25} \quad (7.1)$$

The near surface density calculated from Kisin is 1.5 g/cc, a very close match. The density also fits within the range of densities measured in soil surveys conducted by the Natural Resources Conservation Service in 2011.

A density contrast of 0.75 g/cc provided the closest match in signal magnitude at the peak of the caprock. Assuming a caprock density of 2.75 g/cc this means the surrounding sediment has an estimated density of 2.0 g/cc. This indicates a thin weathing layer with a density of 1.4 g/cc and a thickness of less than 50 m. At 130 m depth the country rock exhibits a density of 2.0 g/cc.

7.2. Caprock

Salt picks from well logs were relied upon for mapping the top of the caprock. Picks made by other authors focus on locating the salt below the caprock and not on the caprock itself (Wilson and Noel, 1983). There are a number of reasons for the lack of caprock picks in wells. Operators have tried to avoid drilling through caprock since it is not an exploration target. Most drilling is on the side of the dome where oil and gas can accumulate in closures formed by salt flanks. Drilling through caprock occurs to find overhangs where additional traps are located, but this has more risk without an available image. There is little knowledge about how far out the caprock extends over the salt, and thus a well might simply go through the caprock and continue into salt (Judston and Stamey, 1933; Xu, 2012).

An interpretation done by Wilson and Noel (1983) only contains two caprock picks. Eti (2004) used 16 well picks in mapping the top of caprock. His top caprock map provides the best

first approximation of the maximum spatial limits of the caprock. The top salt interpretation provided by White Oak Energy based off well logs and seismic data did not include the caprock. Residual anomalies left after calculation of the caprock FTG signal show that the caprock extends beyond Eti's original outline by between 50m and 100m (Figure 6.2).

7.3. Salt Dome

The flanks of the dome are imaged on seismic by using horizon terminations between 500 ms and 2750 ms two-way time (TWT) (Eti, 2004; Coker, 2006)(Figure 7.3). If 1830 m/s is used at 0.250 s one-way time and 2590 m/s is used at 1.375 s one-way time then the salt flank used by previous other is between 460 m and 3500 m depth (Kisin, 2003; Duncan, 2005). Figure 7.3 shows that the salt might be extended to as deep as 4000 m. The deepest well logs reach 1900 m depth (Eti, 2004). The interpretation provided by White Oak Energy reached a maximum depth of 2800 m. Eti estimated the maximum depth of salt to be 3800 meters depth. The maximum spatial extent of salt is not mapped at that depth on the seismic reflection data. Instead, Eti's salt map derived from conventional gravity data has been used to determine the maximum depth and spatial extent of salt. A model using Eti's top of salt geometry between 1200 m and 3800 m was input to the forward modelling program, but the signal calculated was much higher magnitude than the measured survey and was not used in the final subtraction.

There is an elongate feature observed in the H-1, R-1, and R-2 attributes of the data that is inside the maximum extent of the salt dome established by Eti. The boundary is longer on the north-south axis and narrower east-west when compared to Eti's maximum extent of salt interpretation. The salt dome appears to have three distinct boundary geometries through its total depth. Subcaprock to below 2800m boundary changes from circular to elongate along the

northeast-southwest axis and follows the trend of the counter-regional fault. Below 2800m the elongate boundary rotates to an orientation along north-south. This shape changes into a tear shape at the 3800m maximum depth.

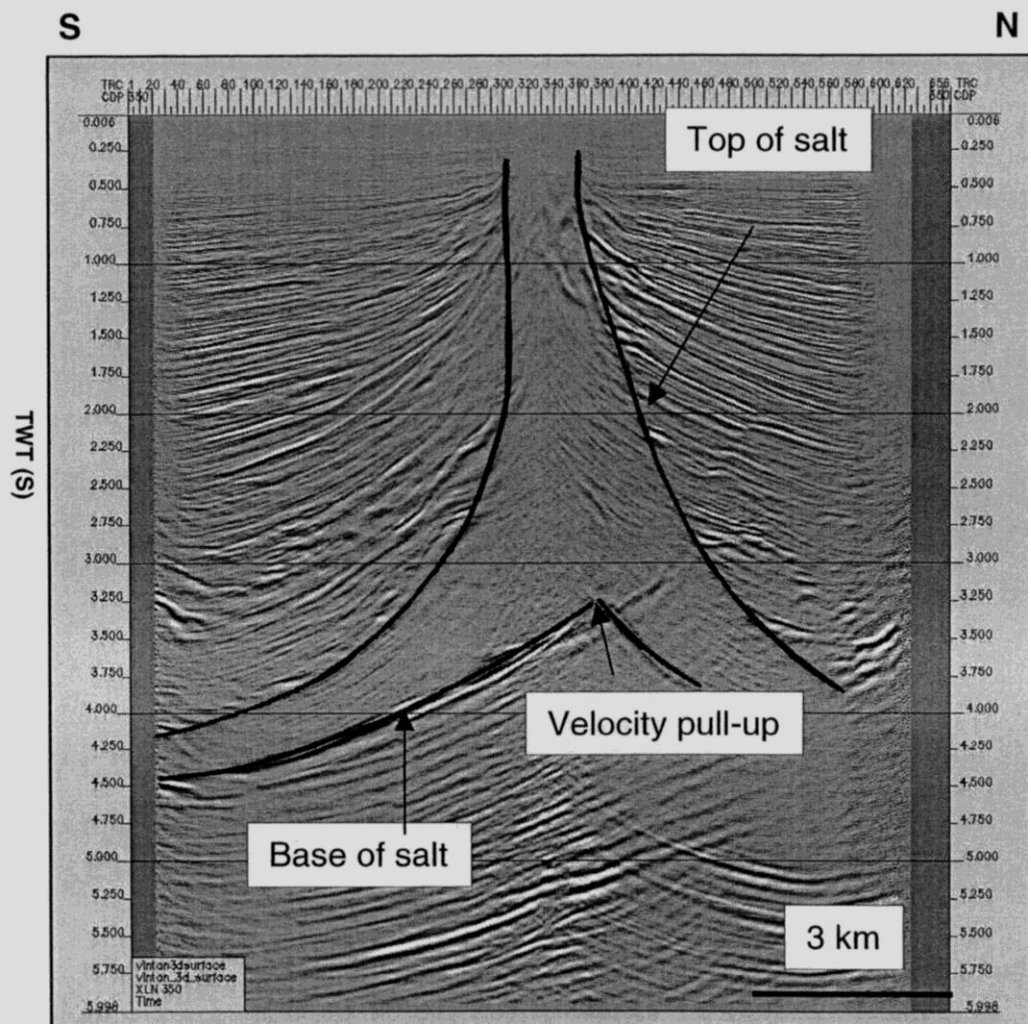

Figure 7.1. Top and base salt interpretation of seismic showing the time interval of used for interpreting the salt (Eti, 2004).

7.4. Faults

There is extensive faulting around the Vinton dome. Faults have a wide range of depths, throws, lengths, and orientations. Many faults were mapped by Coker (2006) on four horizons.

It was intuited that the main count-regional fault would have a noticeable expression on the FTG data due to its length, reported throw, and extensive continuity in depth. After residual maps were generated the expression of the fault was not seen in the data. A velocity model generated by Duncan (2005) based on well logs illustrates that the throw of the counter-regional fault does not have a significant impact on the velocities (and by extension the densities) until 1200 meters depth. The footwall and the hanging wall reach equal velocities again at 2200 meters depth. Directly above that point the footwall has a velocity of 3000m/s (8500 ft/s) while the hanging wall has a velocity of 2280 m/s (7500 ft/s). Using Gardner's equation this gives the footwall a density of 2.21g/cc. The hanging wall density is 2.14 g/cc. This gives a density contrast of 0.07 g/cc at a depth of 2200 m, the lowest point in which the fault affects the velocity model. This configuration generates a signal below 1.5 Eötvös on the Tzz gradient spread over a distance of 5000 m.

The radial fault sets around the dome may be imaged by the FTG data. Figure 7.5 shows Coker's fault interpretation from seismic overlaid on the H-2 invariant of the FTG data. The method illustrated in Mataragio and Kieley (2009) does not use peaks or troughs for delineating radial fractures. Their interpretational approach is by placing faults within discontinuities found within the surface of a broader signal generated by a large scale igneous intrusion. Even using this methodology, not all of Coker's faults are apparent in the attribute, and this can be attributed to throw. This is implied by the depth-density curve derived for Vinton. Faults with

small displacements will have formations in the headwall and footwall that are very similar in density, and so will have a smaller impact on the gravity field.

The divergent faults on the northeast side of the dome may be the best candidate for imaging on FTG data. They are the shallowest of the three fault sets with the steepest dips between 45 and 60 degrees (Coker, 2006). The faults have throws between 2m and 53m, which is less than the faults on the southeast side of the dome.

The southeast en echelon faults have larger throws (between 2m and 53 m) than the northeast divergent faults, but the southern faults dip between 30 and 45 degrees. There is a downthrown graben on the south side of the dome formed by two faults. This should have a negative anomaly expression due to a high density matrix encasing the lower density rock formed at a shallower depth, but does not. There is a positive trend on the Tzz data that extends south from the southern edge of the caprock.

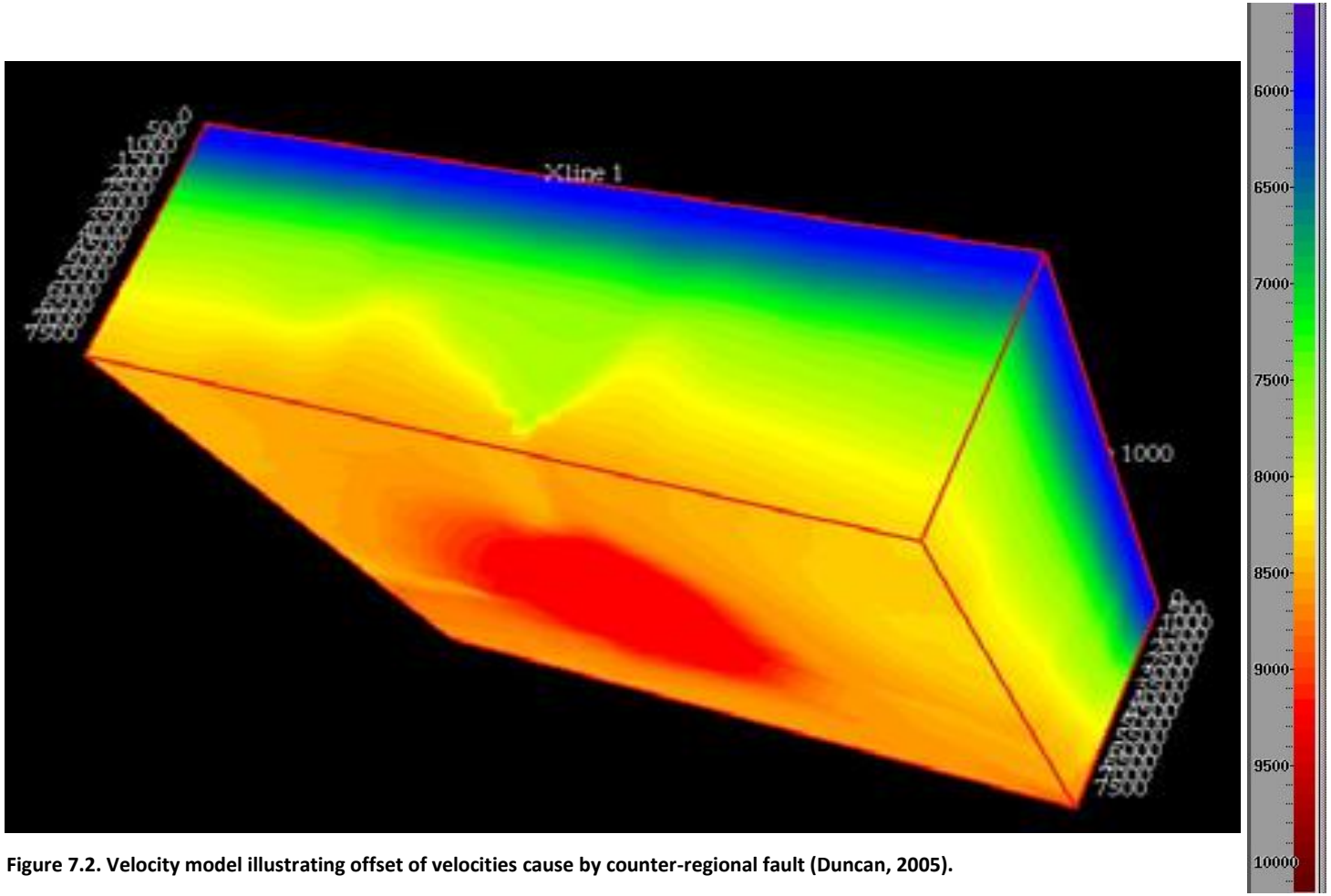

Figure 7.2. Velocity model illustrating offset of velocities cause by counter-regional fault (Duncan, 2005).

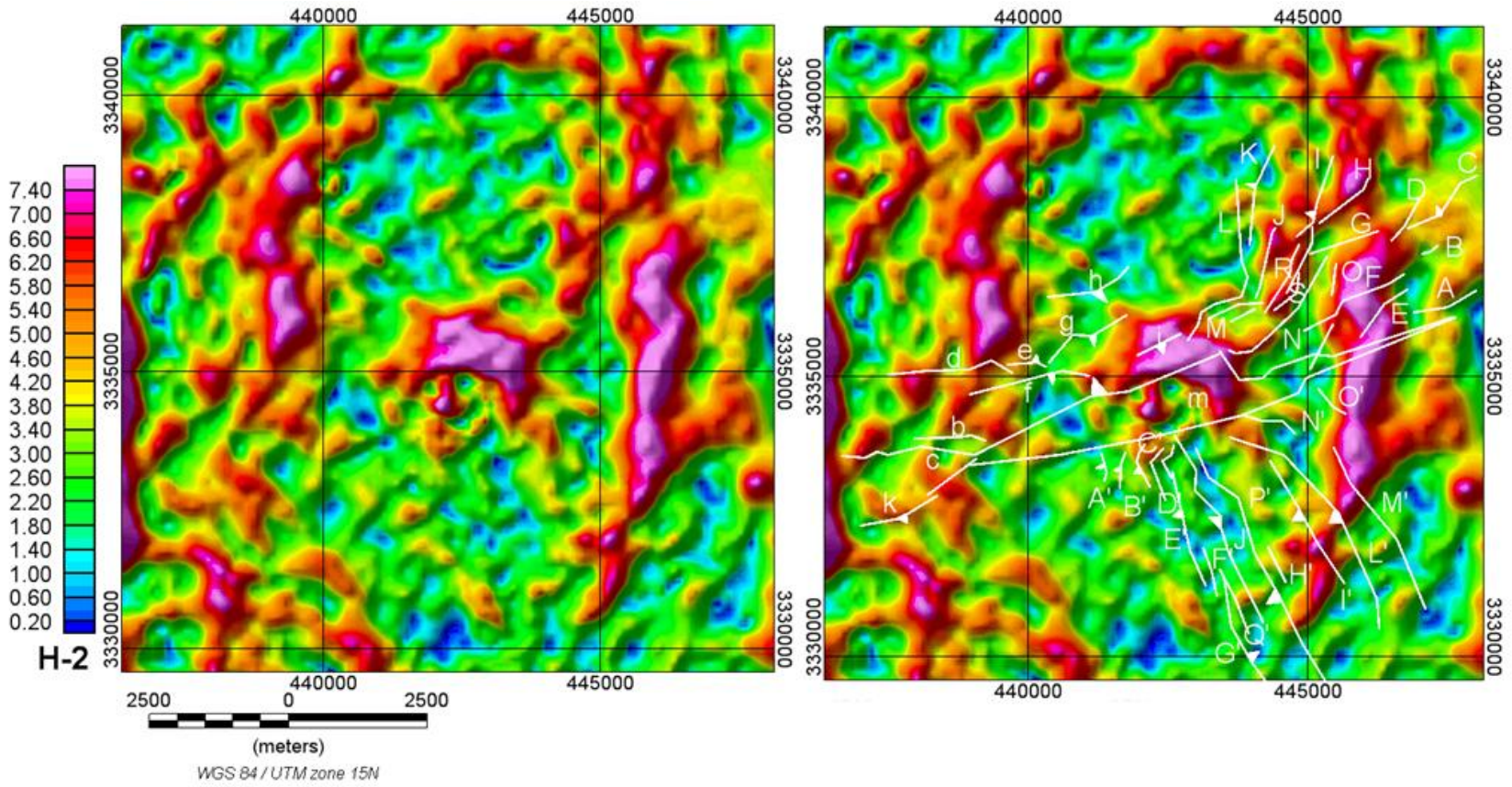

Figure 7.3. H-2 Invariant without and with fault interpretation overlain (Coker, 2006).

7.5. Reservoirs

Most reservoirs are perforated at depths between 500m and 2000m (SONRIS, 2012). Perforation intervals range from 1m to 50m. The perforation intervals can be divided into two groups; above 1300m depth and below 1300m depth coinciding with the Miocene Formation and the Frio Formation respectively (Figure 7.4). Figure 7.5 shows these two groups on the Tzz residual maps that have been upward continued to 500 m and 1000 m. The upward continued surfaces roughly correspond to the signals recorded for those depths in the subsurface. The group of production wells above 1300 m depth is in close proximity to the caprock and upper portion of the dome. Most are on the north side of the dome, and more negative signal is located on the north side of the dome than the south side of the dome. Production intervals below 1300m depth are further north and are more coincident with the residual low on the north side of the dome than wells shallower than 1300 m. Only a single production well has been established on the south side of the dome below 1300 m. It is located on the west side of the dome closer to a residual low.

The production distribution can be attributed to the relationship of the counter-regional fault to the dome. The headwall of the fault is on the north side of the dome. Downward sliding of the block has caused the formations on the north side of the dome to be thicker and more horizontal. Formations on the south side of the dome are thinner and much steeper due to drag as the salt migrated along the fault plane (Xu et al., 2012).

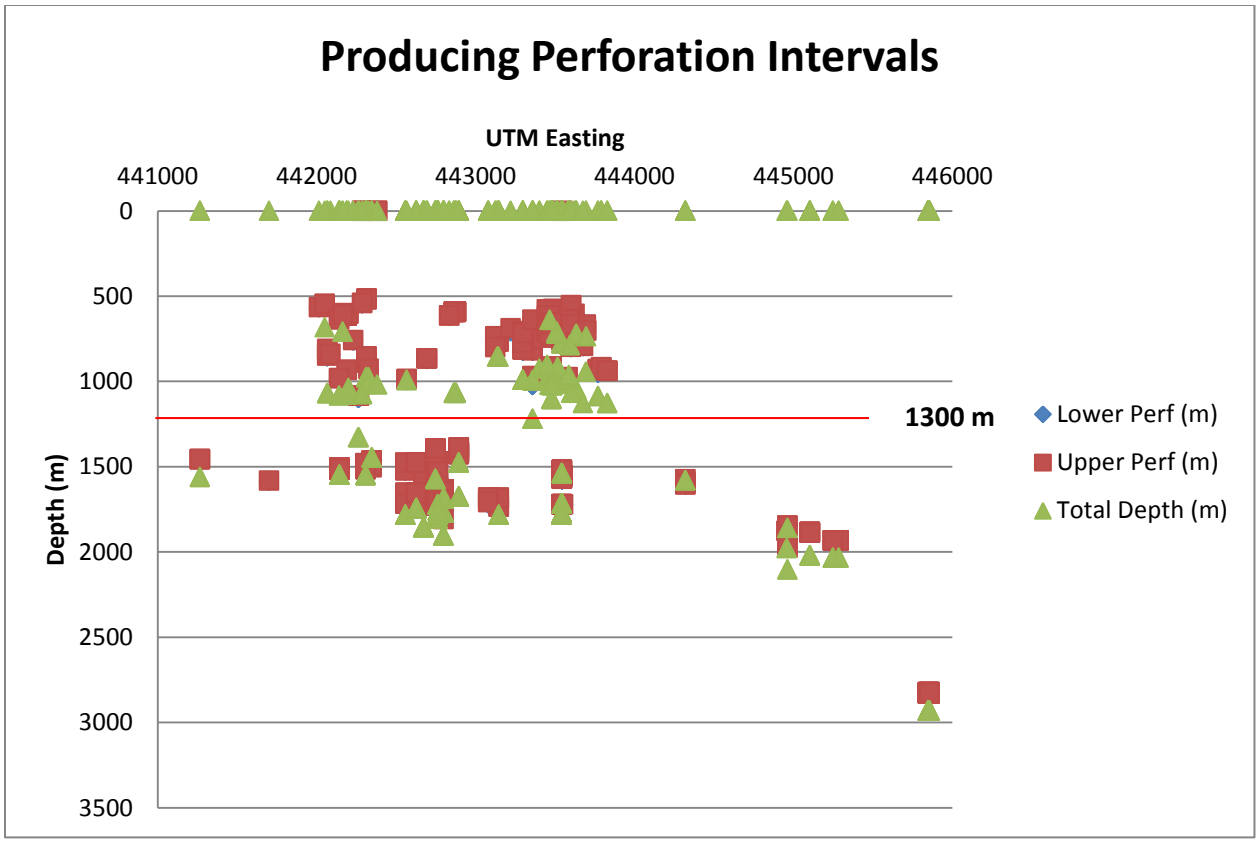

Figure 7.4. Distribution of producing perforation intervals from east to west across survey area (SONRIS, 2012).

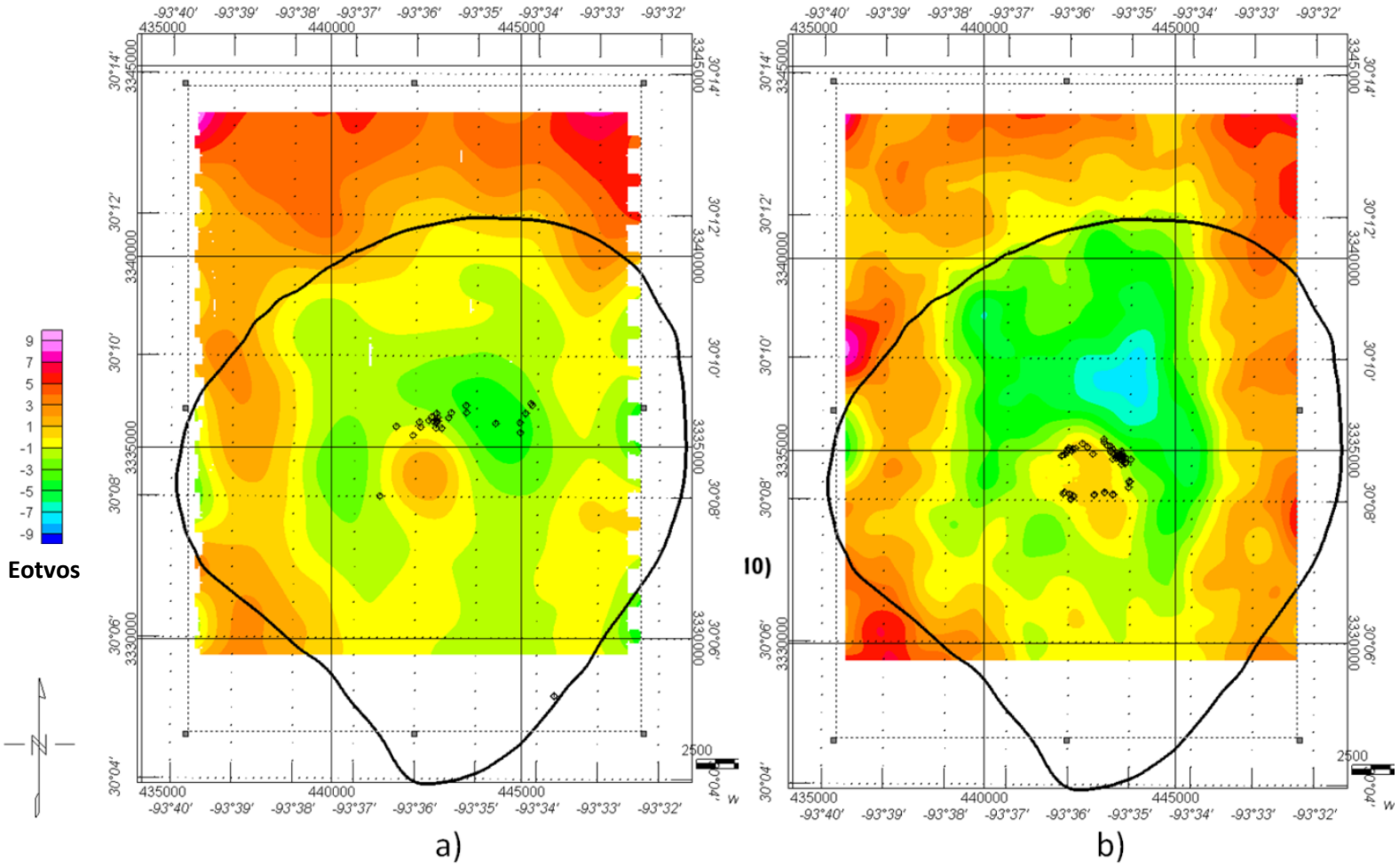

Figure 7.5. a) Residual Tzz surface upward continued to 1000 m with production wells deeper than 1300 m plotted. b) Residual Tzz surface upward continued to 500 m with production wells shallower than 1300 m plotted. Maximum extent of salt outlined in black

Chapter 8

Conclusions

A model for calculating the expected signal from the Vinton salt dome was built and input to a FTG forward calculation algorithm. The calculated signal was subtracted from the measured gradients with the expectation that most, if not all, of the signal from the salt dome would be taken out and the remaining residual map would contain signal from other subsurface bodies such as gas charged reservoirs and faults. After subtraction several anomalies consistent with the caprock and salt dome signal were observed. This suggests that signal from the salt dome and caprock was not predicted by the model. This could be due to a lack of *a priori* information in areas poorly predicted by the model calculation. This leads to the conclusion that Full Tensor Gradiometry can provide information about the subsurface in areas of sparse data coverage such as areas where only 2D reflection seismic data or well logs are the only sources of information about the subsurface.

In the case of the Vinton Salt dome, the Full Tensor Gradiometry method presented a more continuous image of the caprock and deep salt than available from well logs or 3D reflection seismic data. Reflection seismic data coverage over the caprock of the dome was absent while FTG imaging of the caprock was possible. Reservoir modeling illustrated that reservoirs smaller than 2500 m^2 below 500 m depth had signal less than the 7 Eötvös. Linking known production with the expected reservoir signal produced mixed results. Potential reservoirs were correlated across all six gradients based on signal calculated from constructed reservoir models. Fifteen prospective areas were identified from residual gradient maps and

were also imaged on the R-1 invariant attribute. Oil and gas production was observed in five of the sixteen prospective areas. Dry holes were observed in four of the sixteen areas. The H-1 invariant attribute derived from the residual maps suggested a narrower maximum extent of the salt dome at a depth of 3.8 km than previously proposed by Eti (2004). A number of radial features were observed on the H-2 invariant attribute, but most of the picked lineations did not correspond to faults previously mapped on 3D reflection seismic data.

8.1. Future Work

New acquisition systems and technology in recent years have increased the amount of FTG data available for study (Bell et al., 1997). There are additional processing methods and gridding methods that can be applied to this FTG dataset that are outside the scope of this study. There are also additional attributes that can be derived from the FTG dataset.

Additional gridding methods that take advantage of all six tensor components are available, but any method will suffer from the noise content of the measured survey (Fitzgerald, 2011; Pederson, 1990). However, Geosoft Montaj software used for the current study does not have built-in solutions for utilizing the full tensor measurements. Added functionality to Geosoft Montaj, or another software package would be needed to apply this type of gridding.

Use of an inversion algorithm would be useful in deriving a salt body geometry from the FTG data. There are several inversion methods available (Nagihara and Hall, 2001; Hokdstad et al., 2011; Wan and Zhdanov, 2008; Li, 2001).

Additional attributes can also be derived from the FTG data. Dickinson et al. (2009) measured strike from tensor data with the equation:

$$\tan 2\,\theta s = 2\,\frac{Txy(Txx+Tyy)+TxzTyz}{Txx^2-Tyy^2+Txz^2-Tyz^2} \quad (8.1)$$

The strike angle is calculated at each data point, and consistent values are connected to form lineaments. The ability to connect similar values is not included in the Geosoft Montaj package, and was not part of the original scope of the project.

Appendix

MATLAB Programs used for this study

Model creation for input to forward modeling program

```
%Salt model, numbers are in 100 m increments
%model has 66 blocks east-west, 45 blocks north-south, and 28 blocks vertical
%100 meters, each block is 100m x 100m
%Numbers are specified from south to north
%bottom layer is 2740 m rounded to 2700
%density contrast is -170 (-0.17g/cc)
T1=zeros([66 3]);
T2=zeros([18 2]);
T3=repmat(-170,[25 2]);
T4=zeros([23 2]);
T5=[T2; T3; T4];
T6=zeros([14 2]);
T7=repmat(-170,[32 2]);
T8=zeros([20 2]);
T9=[T6; T7; T8];
T10=zeros([12 1]);
T11=repmat(-170,[36 1]);
T12=zeros([18 1]);
T13=[T10; T11; T12];
T14=zeros([12 3]);
T15=repmat(-170,[38 3]);
T16=zeros([16 3]);
T17=[T14; T15; T16];
T18=zeros([10 10]);
T19=repmat(-170,[42 10]);
T20=zeros([14 10]);
T21=[T18; T19; T20];
T22=zeros([10 2]);
T23=repmat(-170,[46 2]);
T24=zeros([10 2]);
T25=[T22; T23; T24];
T26=zeros([12 2]);
T27=repmat(-170,[46 2]);
T28=zeros([8 2]);
T29=[T26; T27; T28];
```

```
T30=zeros([15 3]);
T31=repmat(-170,[46 3]);
T32=zeros([5 3]);
T33=[T30; T31; T32];
T34=zeros([17 3]);
T35=repmat(-170,[46 3]);
T36=zeros([3 3]);
T37=[T34; T35; T36];
T38=zeros([20 2]);
T39=repmat(-170,[43 2]);
T40=zeros([3 2]);
T41=[T38; T39; T40];
T42=zeros([24 2]);
T43=repmat(-170,[39 2]);
T44=zeros([3 2]);
T45=[T42; T43; T44];
T46=zeros([30 2]);
T47=repmat(-170,[30 2]);
T48=zeros([6 2]);
T49=[T46; T47; T48];
T50=zeros([40 2]);
T51=repmat(-170,[15 2]);
T52=zeros([11 2]);
T53=[T50; T51; T52];
T54=zeros([66 6]);
TL27=[T1, T5, T9, T13, T17, T21, T25, T29, T33, T37, T41, T45, T49, T53, T54];
%layer is 2440 m rounded to 2400
%density contrast between salt and sediment is -150 (-0.15g/cc)
T55=zeros([66 5]);
T56=zeros([18 2]);
T57=repmat(-150,[24 2]);
T58=zeros([24 2]);
T59=[T56; T57; T58];
T60=zeros([16 2]);
T61=repmat(-150,[28 2]);
T62=zeros([22 2]);
T63=[T60; T61; T62];
T64=zeros([14 2]);
T65=repmat(-150,[32 2]);
T66=zeros([20 2]);
T67=[T64; T65; T66];
T68=zeros([13 2]);
T69=repmat(-150,[34 2]);
T70=zeros([19 2]);
T71=[T68; T69; T70];
T72=zeros([12 6]);
```

```
T73=repmat(-150,[35 6]);
T74=zeros([19 6]);
T75=[T72; T73; T74];
T76=zeros([13 3]);
T77=repmat(-150,[34 3]);
T78=zeros([19 3]);
T79=[T76; T77; T78];
T80=zeros([14 1]);
T81=repmat(-150,[35 1]);
T82=zeros([17 1]);
T83=[T80; T81; T82];
T84=zeros([15 1]);
T85=repmat(-150,[35 1]);
T86=zeros([16 1]);
T87=[T84; T85; T86];
T88=zeros([17 2]);
T89=repmat(-150,[34 2]);
T90=zeros([15 2]);
T91=[T88; T89; T90];
T92=zeros([18 2]);
T93=repmat(-150,[36 2]);
T94=zeros([12 2]);
T95=[T92; T93; T94];
T96=zeros([20 2]);
T97=repmat(-150,[34 2]);
T98=zeros([12 2]);
T99=[T96; T97; T98];
T100=zeros([23 2]);
T101=repmat(-150,[31 2]);
T102=zeros([12 2]);
T103=[T100; T101; T102];
T104=zeros([30 2]);
T105=repmat(-150,[23 2]);
T106=zeros([13 2]);
T107=[T104; T105; T106];
T108=zeros([39 2]);
T109=repmat(-150,[10 2]);
T110=zeros([17 2]);
T111=[T108; T109; T110];
T112=zeros([66 9]);
TL24=[T55, T59, T63, T67, T71, T75, T79, T83, T87, T91, T95, T99, T103, T107, T111, T112];
%layer is 2130 m rounded to 2100
%density contrast between salt and sediment is -130 (-0.13g/cc)
T113=zeros([66 6]);
T114=zeros([22 1]);
T115=repmat(-130,[5 1]);
```

```
T116=zeros([39 1]);
T117=[T114; T115; T116];
T118=zeros([19 1]);
T119=repmat(-130,[19 1]);
T120=zeros([28 1]);
T121=[T118; T119; T120];
T122=zeros([17 1]);
T123=repmat(-130,[24 1]);
T124=zeros([25 1]);
T125=[T122; T123; T124];
T126=zeros([17 1]);
T127=repmat(-130,[25 1]);
T128=zeros([24 1]);
T129=[T126; T127; T128];
T130=zeros([16 1]);
T131=repmat(-130,[26 1]);
T132=zeros([24 1]);
T133=[T130; T131; T132];
T134=zeros([15 3]);
T135=repmat(-130,[29 3]);
T136=zeros([22 3]);
T137=[T134; T135; T136];
T138=zeros([14 3]);
T139=repmat(-130,[31 3]);
T140=zeros([21 3]);
T141=[T138; T139; T140];
T142=zeros([14 2]);
T143=repmat(-130,[30 2]);
T144=zeros([22 2]);
T145=[T142; T143; T144];
T146=zeros([15 2]);
T147=repmat(-130,[29 2]);
T148=zeros([22 2]);
T149=[T146; T147; T148];
T150=zeros([16 1]);
T151=repmat(-130,[28 1]);
T152=zeros([22 1]);
T153=[T150; T151; T152];
T154=zeros([17 1]);
T155=repmat(-130,[28 1]);
T156=zeros([21 1]);
T157=[T154; T155; T156];
T158=zeros([18 1]);
T159=repmat(-130,[27 1]);
T160=zeros([21 1]);
T161=[T158; T159; T160];
```

```
T162=zeros([19 1]);
T163=repmat(-130,[28 1]);
T165=zeros([19 1]);
T166=[T162; T163; T165];
T167=zeros([20 1]);
T168=repmat(-130,[27 1]);
T169=zeros([19 1]);
T170=[T167; T168; T169];
T171=zeros([20 1]);
T172=repmat(-130,[28 1]);
T173=zeros([18 1]);
T174=[T171; T172; T173];
T175=zeros([21 1]);
T176=repmat(-130,[28 1]);
T177=zeros([17 1]);
T178=[T175; T176; T177];
T179=zeros([22 1]);
T180=repmat(-130,[27 1]);
T181=zeros([17 1]);
T182=[T179; T180; T181];
T183=zeros([24 1]);
T184=repmat(-130,[25 1]);
T185=zeros([17 1]);
T186=[T183; T184; T185];
T187=zeros([27 1]);
T188=repmat(-130,[22 1]);
T189=zeros([17 1]);
T190=[T187; T188; T189];
T191=zeros([30 1]);
T192=repmat(-130,[17 1]);
T193=zeros([19 1]);
T194=[T191; T192; T193];
T195=zeros([37 1]);
T196=repmat(-130,[10 1]);
T197=zeros([19 1]);
T198=[T195; T196; T197];
T199=zeros([66 12]);
TL21=[T113, T117, T121, T125, T129, T133, T137, T141, T145, T149, T153, T157, T161, T166,
T170, T174, T178, T182, T186, T190, T194, T198, T199];
%Layer at 1800m
% density contrast between salt and sediment is -100 (-0.1 g/cc)
T200=zeros([66 8]);
T201=zeros([21 1]);
T202=repmat(-100,[17 1]);
T203=zeros([28 1]);
T204=[T201; T202; T203];
```

```
T205=zeros([19 1]);
T206=repmat(-100,[20 1]);
T207=zeros([27 1]);
T208=[T205; T206; T207];
T209=zeros([18 1]);
T210=repmat(-100,[22 1]);
T211=zeros([26 1]);
T212=[T209; T210; T211];
T213=zeros([17 1]);
T214=repmat(-100,[24 1]);
T215=zeros([25 1]);
T216=[T213; T214; T215];
T217=zeros([17 1]);
T218=repmat(-100,[25 1]);
T219=zeros([24 1]);
T220=[T217; T218; T219];
T221=zeros([16 6]);
T222=repmat(-100,[26 6]);
T223=zeros([24 6]);
T224=[T221; T222; T223];
T225=zeros([17 2]);
T226=repmat(-100,[25 2]);
T227=zeros([24 2]);
T228=[T225; T226; T227];
T229=zeros([19 1]);
T230=repmat(-100,[23 1]);
T231=zeros([24 1]);
T232=[T229; T230; T231];
T233=zeros([20 2]);
T234=repmat(-100,[22 2]);
T235=zeros([24 2]);
T236=[T233; T234; T235];
T237=zeros([21 1]);
T238=repmat(-100,[22 1]);
T239=zeros([23 1]);
T240=[T237; T238; T239];
T241=zeros([22 1]);
T242=repmat(-100,[21 1]);
T243=zeros([23 1]);
T244=[T241; T242; T243];
T245=zeros([23 1]);
T246=repmat(-100,[21 1]);
T247=zeros([22 1]);
T248=[T245; T246; T247];
T249=zeros([26 1]);
T250=repmat(-100,[18 1]);
```

```
T251=zeros([22 1]);
T252=[T249; T250; T251];
T253=zeros([30 1]);
T254=repmat(-100,[14 1]);
T255=zeros([22 1]);
T256=[T253; T254; T255];
T257=zeros([35 1]);
T258=repmat(-100,[8 1]);
T259=zeros([23 1]);
T260=[T257; T258; T259];
T261=zeros([66 15]);
TL18=[T200 T204 T208 T212 T216 T220 T224 T228 T232 T236 T240 T244 T248 T252 T256 T260
T261];
%Layer at 1500m
%density contrast between salt and sediment is -70 (-0.07g/cc)
T262=zeros([66 9]);
T263=zeros([22 1]);
T264=repmat(-70,[14 1]);
T265=zeros([30 1]);
T266=[T263; T264; T265];
T267=zeros([21 1]);
T268=repmat(-70,[17 1]);
T269=zeros([28 1]);
T270=[T267; T268; T269];
T271=zeros([19 1]);
T272=repmat(-70,[20 1]);
T273=zeros([27 1]);
T274=[T271; T272; T273];
T275=zeros([19 1]);
T276=repmat(-70,[21 1]);
T277=zeros([26 1]);
T278=[T275; T276; T277];
T279=zeros([18 1]);
T280=repmat(-70,[22 1]);
T281=zeros([26 1]);
T282=[T279; T280; T281];
T283=zeros([18 2]);
T284=repmat(-70,[23 2]);
T285=zeros([25 2]);
T286=[T283; T284; T285];
T287=zeros([18 3]);
T288=repmat(-70,[22 3]);
T289=zeros([26 3]);
T290=[T287; T288; T289];
T291=zeros([19 1]);
T292=repmat(-70,[21 1]);
```

```
T293=zeros([26 1]);
T294=[T291; T292; T293];
T295=zeros([20 1]);
T296=repmat(-70,[20 1]);
T297=zeros([26 1]);
T298=[T295; T296; T297];
T299=zeros([21 1]);
T300=repmat(-70,[19 1]);
T301=zeros([26 1]);
T302=[T295; T296; T297];
T303=zeros([22 1]);
T304=repmat(-70,[17 1]);
T305=zeros([27 1]);
T306=[T303; T304; T305];
T307=zeros([23 2]);
T308=repmat(-70,[16 2]);
T309=zeros([27 2]);
T310=[T307; T308; T309];
T311=zeros([25 1]);
T312=repmat(-70,[14 1]);
T313=zeros([27 1]);
T314=[T311; T312; T313];
T315=zeros([29 1]);
T316=repmat(-70,[10 1]);
T317=zeros([27 1]);
T318=[T315; T316; T317];
T319=zeros([66 18]);
TL15=[T262 T266 T270 T274 T278 T282 T286 T290 T294 T298 T302 T306 T310 T314 T318 T319];
%Layer at 1200m; -.05 density contrast,
% density contrast between salt and sediment is -50 (-0.05 g/cc)
T320=zeros([66 10]);
T321=zeros([23 1]);
T322=repmat(-50,[13 1]);
T323=zeros([30 1]);
T324=[T321; T322; T323];
T325=zeros([21 1]);
T326=repmat(-50,[16 1]);
T327=zeros([29 1]);
T328=[T325; T326; T327];
T329=zeros([21 1]);
T330=repmat(-50,[17 1]);
T331=zeros([28 1]);
T332=[T329; T330; T331];
T333=zeros([19 5]);
T334=repmat(-50,[20 5]);
T335=zeros([27 5]);
```

```
T336=[T333; T334; T335];
T337=zeros([20 1]);
T338=repmat(-50,[18 1]);
T339=zeros([28 1]);
T340=[T337; T338; T339];
T341=zeros([21 1]);
T342=repmat(-50,[17 1]);
T343=zeros([28 1]);
T344=[T341; T342; T343];
T345=zeros([22 1]);
T346=repmat(-50,[16 1]);
T347=zeros([28 1]);
T348=[T345; T346; T347];
T349=zeros([23 1]);
T350=repmat(-50,[15 1]);
T351=zeros([28 1]);
T352=[T349; T350; T351];
T353=zeros([24 1]);
T354=repmat(-50,[13 1]);
T355=zeros([29 1]);
T356=[T353; T354; T355];
T357=zeros([28 1]);
T358=repmat(-50,[8 1]);
T359=zeros([30 1]);
T360=[T357; T358; T359];
T361=zeros([30 1]);
T362=repmat(-50,[6 1]);
T363=zeros([30 1]);
T364=[T361; T362; T363];
T365=zeros([66 20]);
TL12=[T320 T324 T328 T332 T336 T340 T344 T348 T352 T356 T360 T364 T365];
%Layer at 900m
% density contrast between salt and sediment is -20 (-0.02 g/cc)
T366=zeros([66 10]);
T367=zeros([32 1]);
T368=repmat(-20,[2 1]);
T369=zeros([32 1]);
T370=[T367; T368; T369];
T371=zeros([23 1]);
T372=repmat(-20,[12 1]);
T373=zeros([31 1]);
T374=[T371; T372; T373];
T375=zeros([22 1]);
T376=repmat(-20,[14 1]);
T377=zeros([30 1]);
T378=[T375; T376; T377];
```

```
T379=zeros([21 1]);
T380=repmat(-20,[16 1]);
T381=zeros([29 1]);
T382=[T379; T380; T381];
T383=zeros([21 1]);
T384=repmat(-20,[17 1]);
T385=zeros([28 1]);
T386=[T383; T384; T385];
T387=zeros([20 2]);
T388=repmat(-20,[18 2]);
T389=zeros([28 2]);
T390=[T387; T388; T389];
T391=zeros([21 1]);
T392=repmat(-20,[16 1]);
T393=zeros([29 1]);
T394=[T391; T392; T393];
T395=zeros([22 1]);
T396=repmat(-20,[15 1]);
T397=zeros([29 1]);
T398=[T395; T396; T397];
T399=zeros([23 1]);
T400=repmat(-20,[14 1]);
T401=zeros([29 1]);
T402=[T399; T400; T401];
T403=zeros([24 1]);
T404=repmat(-20,[13 1]);
T405=zeros([29 1]);
T406=[T403; T404; T405];
T407=zeros([25 1]);
T408=repmat(-20,[12 1]);
T409=zeros([29 1]);
T410=[T407; T408; T409];
T411=zeros([30 1]);
T412=repmat(-20,[6 1]);
T413=zeros([30 1]);
T414=[T411; T412; T413];
T415=zeros([66 22]);
TL9=[T366 T370 T374 T378 T382 T386 T390 T394 T398 T402 T406 T410 T414 T415];
%Layer at 600m
% density contrast between salt and sediment is 50 (0.05 g/cc)
T416=zeros([66 12]);
T417=zeros([32 1]);
T418=repmat(50,[2 1]);
T419=zeros([32 1]);
T420=[T417; T418; T419];
T421=zeros([32 1]);
```

```
T422=repmat(50,[3 1]);
T423=zeros([31 1]);
T424=[T421; T422; T423];
T425=zeros([23 1]);
T426=repmat(50,[12 1]);
T427=zeros([31 1]);
T428=[T425; T426; T427];
T429=zeros([23 1]);
T430=repmat(50,[12 1]);
T431=zeros([31 1]);
T432=[T429; T430; T431];
T433=zeros([23 1]);
T434=repmat(50,[11 1]);
T435=zeros([32 1]);
T436=[T433; T434; T435];
T437=zeros([24 1]);
T438=repmat(50,[9 1]);
T439=zeros([33 1]);
T440=[T437; T438; T439];
T441=zeros([25 1]);
T442=repmat(50,[8 1]);
T443=zeros([33 1]);
T444=[T441; T442; T443];
T445=zeros([25 1]);
T446=repmat(50,[8 1]);
T447=zeros([33 1]);
T448=[T445; T446; T447];
T449=zeros([26 1]);
T450=repmat(50,[9 1]);
T451=zeros([31 1]);
T452=[T449; T450; T451];
T453=zeros([32 1]);
T454=repmat(50,[3 1]);
T455=zeros([31 1]);
T456=[T453; T454; T455];
T457=zeros([66 23]);
TL6=[T416 T420 T424 T428 T432 T436 T440 T444 T448 T452 T456 T457];
%Layer at 300m
% density contrast between salt and sediment is 400 (0.4 g/cc)
T458=zeros([66 12]);
T459=zeros([32 1]);
T460=repmat(400,[2 1]);
T461=zeros([32 1]);
T462=[T459; T460; T461];
T463=zeros([32 1]);
T464=repmat(400,[3 1]);
```

```
T465=zeros([31 1]);
T466=[T463; T464; T465];
T467=zeros([23 1]);
T468=repmat(400,[12 1]);
T469=zeros([31 1]);
T470=[T467; T468; T469];
T471=zeros([23 1]);
T472=repmat(400,[12 1]);
T473=zeros([31 1]);
T474=[T471; T472; T473];
T475=zeros([23 1]);
T476=repmat(400,[11 1]);
T477=zeros([32 1]);
T478=[T475; T476; T477];
T479=zeros([24 1]);
T480=repmat(400,[9 1]);
T481=zeros([33 1]);
T482=[T479; T480; T481];
T483=zeros([25 1]);
T484=repmat(400,[8 1]);
T485=zeros([33 1]);
T486=[T483; T484; T485];
T487=zeros([26 1]);
T488=repmat(400,[9 1]);
T489=zeros([31 1]);
T490=[T487; T488; T489];
T491=zeros([66 25]);
TL3=[T458 T462 T466 T470 T474 T478 T482 T486 T490 T491];
%Layer at 360m
% density contrast between salt and sediment is 400 (0.4 g/cc)
T492=zeros([66 11]);
T493=zeros([25 2]);
T494=repmat(400,[11 2]);
T495=zeros([30 2]);
T496=[T493; T494; T495];
T497=zeros([23 8]);
T498=repmat(400,[13 8]);
T499=zeros([30 8]);
T500=[T497; T498; T499];
T501=zeros([66 24]);
TL36=[T492 T496 T500 T501];
%Layer at 260m
% density contrast between salt and sediment is 575 (0.575 g/cc)
T501=zeros([66 12]);
T502=zeros([28 1]);
T503=repmat(575,[5 1]);
```

```
T504=zeros([33 1]);
T505=[T502; T503; T504];
T506=zeros([26 2]);
T507=repmat(575,[9 2]);
T508=zeros([31 2]);
T509=[T506; T507; T508];
T510=zeros([25 3]);
T511=repmat(575,[10 3]);
T512=zeros([31 3]);
T513=[T510; T511; T512];
T514=zeros([27 1]);
T515=repmat(575,[8 1]);
T516=zeros([31 1]);
T517=[T514; T515; T516];
T518=zeros([31 1]);
T519=repmat(575,[3 1]);
T520=zeros([32 1]);
T521=[T518; T519; T520];
T522=zeros([66 25]);
TL2=[T501 T505 T509 T513 T517 T521 T522 ];
%Layer at 160m
% density contrast between salt and sediment is 575 (0.575 g/cc)
%Change T numbers
T523=zeros([66 13]);
T524=zeros([31 1]);
T525=repmat(575,[1 1]);
T526=zeros([34 1]);
T527=[T524; T525; T526];
T528=zeros([31 1]);
T529=repmat(575,[2 1]);
T530=zeros([33 1]);
T531=[T528; T529; T530];
T532=zeros([66 30]);
TL1=[T523 T527 T531 T532];
TS=cat(3, TL1, TL2, TL36, TL3, TL6, TL6, TL6, TL9, TL9, TL9, TL12, TL12, TL12, TL15, TL15, TL15,
TL18, TL18, TL18, TL21, TL21, TL21, TL24, TL24, TL24, TL27, TL27, TL27);
% save('TS3.mat','TS')
```

Forward modeling program

```
% ********************************
% Density -> T Algorithm
% ********************************
load TS3.mat
den = TS;
tqwz=0;
```

```
k(1)=0;
k(2)=0;
k(3)=1;
L(1)=0;
L(2)=0;
L(3)=1;

num_experiments = 1;
e = 16; %north-south
v = 16; %east-west

lp=0;
z0=0.0;
CX=0;
tic
for n = 1:num_experiments

   T = zeros(e,v);

   for v=1:16 %east-west
   CX=CX+1
   x0=1400.1+200*(v-1); %v*200 meters

      for e=1:16 %north-south
      y0=300.1+(e-1)*200; %e*200 meters
      tqwz=tqwz+1;
      GG(tqwz,1)=x0;
      GG(tqwz,2)=y0;

         for yh=1:28 %yh is the number of blocks in the z- (vertical) direction
         lp=0;
         z1=160+(yh-1)*100; %100 m vertical steps
         z2=z1+100;
         z(1)=(z2-z0);
         z(2)=z(1);
         z(3)=z(1);
         z(4)=z(1);
         z(5)=(z1-z0);
         z(6)=z(5);
         z(7)=z(5);
         z(8)=z(5);

            for wh=1:45 %w is the number of blocks in y (S-N) directon
            y1=0+(wh-1)*100;
            y2=y1+100;
```

```
y(1)=(y2-y0); %y0=-200.1+(e-1)*2000
y(2)=y(1);
y(3)=(y1-y0);
y(4)=y(3);
y(5)=y(3);
y(6)=y(3);
y(7)=y(1);
y(8)=y(1);

   for q=1:66
   %lp=lp+1;
   %q is the number of blocks in x (W-E) direction
   x1=0+(q-1)*100;
   x2=x1+100;

   x(1)=(x1-x0);
   x(2)=(x2-x0);
   x(3)=x(2);
   x(4)=x(1);
   x(5)=x(1);
   x(6)=x(2);
   x(7)=x(2);
   x(8)=x(1);

   SS=0.0;
   w(1)=1;
   w(3)=1;
   w(5)=1;
   w(7)=1;
   w(2)=-1;
   w(4)=-1;
   w(6)=-1;
   w(8)=-1;

      for j=1:8
      c=((x(j)^2+y(j)^2+z(j)^2)^0.5);
      A(1,1)=atan(y(j)*z(j)/(x(j)*c));
      A(2,2)=atan(x(j)*z(j)/(y(j)*c));
      A(3,3)=atan(x(j)*y(j)/(z(j)*c));
      A(3,2)=-1*log(x(j)+c);
      A(2,3)=A(3,2);
      A(3,1)=-1*log(y(j)+c);
      A(1,3)=A(3,1);
      A(2,1)=-1*log(z(j)+c);
      A(1,2)=A(2,1);
      SS=SS+w(j)*L*A*k';
```

```
            end

          T(e,v)=T(e,v)+SS*6.67e-11*den(q,wh,yh)*1.0e9;
          end
        end
      end

    GG(tqwz,3)=T(e,v);
    end
  end
toc
figure (n)
contourf(T)
colorbar

end
```

Program for calculating coherence

```
%Normalized Coherence Program
%for 100m grid spacing
%input is tab delimited text file with column 1=x-coord, column 2=y-coord,
%and column 3=FTG gradient value
%all columns must have the same number of values, all rows must have the
%same number of values
%I typically take a text file, put it in my MATLAB directory, rename it by
%replacing the .txt with a .m, and then it can be input here
clear all
close all
load Tyz-fa-lev-TC140-up100-sub-Salt.m
B=Tyz_fa_lev_TC140_up100_sub_Salt;

cc=0
for i=1:142 %number of samples in x-direction
  for j=1:118 %number of samples in y-direction
    cc=cc+1;
    A(i,j)=B(cc,3);
  end
end

tqwz=0;
tic
for i=1:138; %number of samples in x-direction minus 4 (edge buffer)
  y0=3329800+100*(i-1);
  for j=1:114; %(number of samples in y-direction minus 4(edge buffer)
    x0=436600+(j-1)*100;
```

```
      C1=0;
      C2=0;
      C3=0;
      C4=0;

      cc=0;
      tqwz=tqwz+1;
      GG(tqwz,1)=x0; %writes x-coordinates to a file
      GG(tqwz,2)=y0;

      for k=1:3;
         p2=k+j-1;
         for q=1:3;
            p1=q+i-1;
            cc=cc+1;

            NW(cc)=A(p1,p2);
            NE(cc)=A(p1+2,p2);
            SW(cc)=A(p1,p2+2);
            SE(cc)=A(p1+1,p2+1);
            Q(cc)=A(p1+1,p2+1);

         end
      end
      NWM=mean(NW);
      NWV=std(NW);
      NEM=mean(NE);
      NEV=std(NE);
      SEM=mean(SE);
      SEV=std(SE);
      SWM=mean(SW);
      SWV=std(SW);
      QM=mean(Q);
      QV=std(Q);
      for h=1:9;
         C1=C1+0.125*((NW(h)-NWM)*(Q(h)-QM)/NWV*QV);
         C2=C2+0.125*((NE(h)-NEM)*(Q(h)-QM)/NEV*QV);
         C3=C3+0.125*((SE(h)-SEM)*(Q(h)-QM)/SEV*QV);
         C4=C4+0.125*((SW(h)-SWM)*(Q(h)-QM)/SWV*QV);
      end
      CH(i,j)=(abs(C1*C2*C3*C4))^0.25;
      GG(tqwz,3)=CH(i,j);
   end
end
toc
figure (3)
```

```
contourf(CH)
%caxis([0 20])
colorbar
```

References

Bahorich, M., and S. Farmer, 1995, 3-D seismic discontinuity for faults and stratigraphic features: the coherence cube, The Leading Edge, v. 14, p. 1053-1058

Barton, D.C., 1936, Mechanic of formation fo salt domes with special reference to Gulf Coast salt domes of Texas and Louisiana, in: Barton, D.C., and Sawtelle G., eds., SP29: Gulf Coast Oil Fields, American Association of Petroleum Geologists, p. 20-78.

Bell, R. E., Anderson, R., and Pratson, L., 1997, Gravity gradiometry resurfaces: Leading Edge. v 16. p. 55-59.

Borowski, W.S., 1990, Oil and gas developments in Louisiana Gulf Coast onshore in 1989, The American Association of Petroleum Geologists Bulletin, v. 74, p. 75-83.

Branson, R.B., 1991, Productive trends and production history, south Louisiana and adjacent offshore, in: Goldthwaite, D., ed., An introduction to Central Gulf Coast Geology, New Orleans Geological Society, p 61-70.

Coburn, G.W., 2002, A methodology for defining the base and geometry of salt bodies in the deepwater Gulf of Mexico, Gulf Coast Association of Geological Societies Transactions, v. 52, p. 123-133.

Coker, M. O., 2006, Aquitanian (Lower Miocene) depositional system: Vinton dome, onshore Gulf of Mexico, southwest Louisiana: M.Sc. thesis, University of Houston.

Constance, P.E., Holland, M.B., Roche, S.L., Bicquart, P., Bryans, B., Gelinsky, S., Ralph, J.G., and R.I., Bloor, 1999, Simultaneous acquisition of 3-D surface seismic data and 3-C, 3-D VSP data, 69th Annual International Meeting, Society of Exploration Geophysicists, Expanded Abstracts.

Cossey, S.P.J., and R.E. Jacobs, 1992, Oligocene Hackberry Formation of southwest Louisiana: Sequence stratigraphy, sedimontology, and hydrocarbon potential. The American Association of Petroleum Geologists Bulletin, v. 76, p. 589-606.

Deussen, A., 1934, Oil-producing horizons of Gulf Coast in Texas and Louisiana, American Association of Petroleum Geologists Bulletin, v. 18, P. 500-518.

Dickenson, J.L., Brester, J.R., Robinson, J.W., and C.A. Murphy, 2009, Imaging techniques for full tensor gravity gradiometry data, 11th SAGA Biennial Technical Meeting and Exhibition Abstracts, p. 84-88.

Duncan, W. S., 2005, A deterministic evaluation of seismic fidelity using velocity modeling and attribute analysis to improve surface seismic imaging around Vinton Dome Louisiana: M. Sc. Thesis, The University of Houston.

Eti, R.P., 2004, An integrated geophysical study of the Vinton salt dome, Calcasieu Parish, Louisiana: M.Sc Thesis, University of Houston.

Fails, T. G., 1990, Variation in Salt Dome Faulting, Coastal Salt Basin: Gulf Coast Association of Geological Societies Transactions, v. 40, p. 181-193.

Fails, T.G., 1995, Exploration and exploitation of coastal salt basin diapiric structures in the lower Pliocene through Eocene trends: Geology and techniques, New Orleans Geological Society.

Gardner, G. H. F., Gardner L. W., and A. R. Gregory, 1974, Formation velocity and density-the diagnostic basics for stratigraphic traps: Geophysics, v. 39, p. 770-780

Gersztenkorn, A., and Marfurt, K.J., 1999, Eigenstructure-based coherence computations as an aid to 3-D structural and stratigraphic mapping: Geophysics, v. 64, p. 1468-1479.

Gherasim, M., 2005, 3-D VSP Elastic Kirchhoff Pre-stack Depth Migration – Vinton Dome, Louisiana: Ph.D. Dissertation, University of Houston.

Harrison, F.W. Jr., Jones, R.K., and L.C. Searles, eds. 1970, Typical oil and gas fields of southwestern Louisiana, v. 2. Lafayette Geological Society.

Heinrich, P. V., 2005, Distribution and origin of fault-line scarps of southwest Louisiana, USA: Gulf Coast Association of Geological Societies Transactions, v. 55, p. 284-293.

Hoeve, J.A.V., and W.S. Borowski, 1988, Oil and gas developments in Louisiana Gulf Coast onshore in 1987, The American Association of Petroleum Geologists Bulletin, v. 72, p. 75-81.

Hokstad, K., Fotland, B., Mackenzie, G., Antonsdottir, V., Foss, S., Stadtler, C., Fichler, C., Haverl, M., Waagan, B.M.T., Myrlund, E.A., Masnaghetti, L., Ceci, F., and P. Raya, 2011, Joint imaging of geophysical data: Case history from the Nordkapp Basin, Berents Sea, SEG Expanded Abstracts.

Ingram, R.J., 1991, Salt Tectonics, in: Goldthwaite, D., ed., An introduction to Central Gulf Coast Geology, New Orleans Geological Society, p. 31-60.

Jackson, M. P. A., and Talbot, C. J., 1986, External shapes, strain rates, and dynamics of salt structures, Geol. Soc. of Am. Bull., v. 97, p. 305-323

Jacobsen, B.H., 1987, A case for upward continuation as a standard separation filter for potential-field maps, Geophysics, v. 52, p. 1138-1148.

Judson, S.A., and R.A. Stamey, 1933, Overhanging salt on domes of Texas and Louisiana, Bulletin of the American Association of Petroleum Geologists, v. 17, p. 1492-1520.

Kimbro, J.J., 2003, A case study of 3D pre-stack depth imaging for the Vinton Dome: M.Sc. Thesis, University of Houston.

Kisin, S., 2003, Tomographic velocity model building: application to Vinton dome VSP data: M.Sc. Thesis, University of Houston.

Levin, H.L., 2006, The Earth Through Time, Wiley.

Li, Y., 2001, 3-D inversion of gravity gradiometer data, SEG Annual Meeting abstracts.

Li. X., 2009, Spatial-domain transformations: something old and something new, SEG Annual Meeting abstracts, p. 928-932.

Martin, R.G., and A.H. Bouma, 1978, Physiography of Gulf of Mexico: 1. The Setting, SG 7: Framework, Facies, and Oil-Trapping Characteristics of the Upper Continental Margin, American Association of Petroleum Geologists, p. 3-19

Mataragio, J., and J. Kieley, 2009, Application of full tensor gradient invariants in detection of intrusion-hosted sulphide mineralization: implications for deposition mechanisms, First Breaks, v. 27, p. 95-98.

Murphy, C. A., and J. Brewster, 2007, Target delineation using Full Tensor Gravity Gradiometry data, ASEG Abstracts, p. 1-3.

Nagihara, S., and S.A. Hall, 2001, Three-dimensional gravity inversion using simulated annealing: Constraints on the diapiric roots of allochthonous salt structures, Geophysics, v. 66, p. 1438-1449.

Natural Resources Conservation Service (NRCS) database access, 2012, http://websoilsurvey.nrcs.usda.gov/app/HomePage.htm

Nettleton, L.L., 1934, Fluid mechanics of salt domes, Bulletin of the American Association of Petroleum Geologists, v. 18, p. 1175-1204.

O'Brien, J., Rodriguez, A., Sixta, D., Davies, M.A., and P. Houghton, 2005, Resolving the K-2 salt structure in the Gulf of Mexico: An integrated approach using prestack depth imaging and full tensor gravity Gradiometry: The Leading Edge, v. 24, p. 404-409.

Okabe, M., 1979, Analytical expressions for gravity anomalies due to homogeneous polyhedral bodies and translations into magnetic anomalies: Geophysics, v. 44, p. 730-741.

Owen, E.W., 1975. Trek of the oil finders: A History of Exploration for Petroleum, American Association of Petroleum Geologists Memoir 6: p. 191-215

Paine, W.R., 1971, Petrology and sedimentation of the Hackberry sequence of southwest Louisiana, Gulf Coast Association of Geological Societies Transactions, v. 21, p. 37-55.

Paine, W.R., Spillers, J.P., Waters, K.M., Andrews, D.I., Baysinger, E.M., Borland, A.M., Cotton, J., Christina Jr. S.T., Hall Jr., J.P., Kimmey, B.W., McDougall, J.E., Meyerhoff, A.A., Munchrath, M.A., Paffett, D.L., Paspberry, F.L., Rockwood, D.N., Roederer Jr., E.P., Stipe, J.C., and H.O. Woodbury, 1968, Geology of Natural Gas in South Louisiana Lafayette and New Orleans Geological Socities: Part 1, Natural Gases of North America, in: Beebe, B.W., and B.F. Curtis, eds., Natural Gases of North America, American Association of Petroleum Geologists Memoir 9, p. 376-434.

Pearce, M.A., Jones, R.R., Smith, S.A.F., McCaffrey, K.J.W., and Phill Clegg, 2006, Numerical analysis of fold curvature using data acquired by high-precision GPS: Journal of Structural Geology, v. 28, p. 1640-1646.

Pederson, L.B., and T.M. Rasmussen, 1990, The gradient tensor of potential field anomalies: Some implications on data collection and data processing of maps: Geophysics, v. 55, p. 1558-1566.

Peel, F.J., C.J. Travis, and J.R. Hossack, 1995. Genetic structural provinces and salt tectonics of the Cenozoic offshore U.S. Gulf of mexico: a Preliminary analysis, in: M.P.A. Jackson, D.G. Roberts, and S. Snelson, eds., Salt tectonics: a global perspective: AAPG Memoir 65, p. 153-175

Prutzman, J.M., 1998, Subsalt imaging using full tensor gradient and 3D seismic data, Mississippi Canyon, Gulf of Mexico, Society of Petroleum Engineers, SPE 49145.

Rowan, M.G., Jackson, M.P.A., and B.D. Trudgill, 1999, Salt-related fualt families and fault welds in the northern Gulf of Mexico, AAPG Bulletin, v. 83, p. 1454-1484.

Salvador, A., 1985, Chronostratigraphic and geochronometric scales in COSUNS stratigraphic correlation chart of the United States, APPG Bulletin, v. 69, p. 181-189.

Sawtelle, G., 1936, Salt dome statistics, in: Barton, D.C. and G. Sawtelle, eds., Gulf Coast Oil Fields, American Association of Petroleum Geologists SP 29.

Selman, D., 2008, Final Report: Processing and Acquisition of Air-FTG®, Bell Geospace Inc, Houston, Texas.

Swanson, S.M., and A.W. Karlsen, 2009, USGS assessment of undiscovered oil and gas resources for the Oligocene Frio and Anahuac formations, onshore Gulf of Mexico basin, USA, Search and Discovery #101078.

Thompson, S.A., and Eichelberger, O.H., 1928, Vinton salt dome, Calcasieu Parish, Louisiana: American Association of Petroleum Geologists Bulletin., v. 12, p. 385-394.

Wan, L., and M.S. Zhdanov, 2008, Focusing inversion of marine full-tensor gradiometry data in offshore geophysical exploration, SEG abstracts, p. 750-755.

Wilson, F., and J.A. Noel, 1983, A gravity analysis of west-central Calcasieu Parish, Louisiana. Gulf Coast Association of Geological Societies Transactions, v. 33, p. 243-250.

Xu, W., Lewczynski, N., and M.R. Etheredge, 2012. Structural modeling of overturned beds using dip from wells near salt structures, northern Gulf of Mexico. AAPG Annual Convention Abstracts.